Segmentation of Branching Structures from Medical Images

Li Wang B.Eng.

A thesis submitted to
The University of Warwick
in fulfillment of the requirement
for the degree of
Doctor of Philosophy

December 2004

To my parents,
for their encouragement and love.

Segmentation of Branching Structures from Medical Images

Li Wang B. Eng

A thesis submitted to
The University of Warwick
for the degree of
Doctor of Philosophy

December 2004

Summary

Segmentation is a preliminary but important stage in most applications that use medical image data. The work in this thesis mainly focuses on branching structure segmentation on 2D retinal images, by applying image processing and statistical pattern recognition techniques.

This thesis presents a vascular modelling algorithm based on a multi-resolution image representation. A 2D Hermite polynomial is introduced to model the blood vessel profile in a quad-tree structure over a range of spatial/spatial-frequency resolutions. The use of a multi-resolution representation allows robust analysis by combining information across scales and to help improve computational efficiency.

A Fourier based modelling and estimation process is developed, followed by an EM type of optimisation scheme to estimate model parameters. An information based process is then presented to select the most appropriate scale/model for modelling each region of the image. In the final stage, a deterministic graph theoretic approach and a stochastic approach within a Bayesian framework are employed for linking the local features and inferring the global vascular structure.

Experimental results on a number of retinal images have been shown to demonstrate the effective application of the proposed algorithms. Some preliminary results on 3D data are also presented showing the possible extension of the algorithms.

Keywords

Retinal Images, Hermite-Gaussian Modelling, EM, AIC, Kruskal M-Spanning Tree, Stochastic linking algorithm

Contents

Acknowledgments

As I stand at the threshold of earning my doctorate, I am overwhelmed when I recall all the people who have helped me get this far.

First and foremost, I would like to take this opportunity to express my indebted gratitude to my supervisor, Dr. Abhir Bhalerao. He introduced me to the image processing world and has always been extremely generous with his time, knowledge and ideas and given me great freedom in this research. His enthusiastic approach to research, vast knowledge in image processing and his truly remarkable personality have made this experience all the more enjoyable and I am greatly appreciative. I would also like to thank Prof. Roland Wilson for his valuable advice and inspiration throughout my PhD study.

My university colleagues and friends have made my stay at Warwick a truly enjoyable experience. Their collective intellectual energy has been a great motivator for me. I would like to thank Guo-Huei Chen, Peter Meulemans, Denis Fan, XiaoRan Mo, Vincent Ng, Nasir Rajapoot and Constantino-Carlos Reyes-Aldasoro.

Special thanks to Dr. Adam Hoover at University of South Carolina for making his retinal image database publicly available which has been a valuable resource for this research.

Last, but not least I would like to thank my parents for being an unstinting source of love, support and encouragement. Where would I be without them!

Declaration

I declare that, except where acknowledged, the material contained in this thesis is my own work and has not been submitted elsewhere for the purpose of obtaining an academic degree.

Li Wang

Dec. 2004

List of Figures

List of Tables

List of Notations

List of key notations used in the thesis:

B	=	Size of image block in each dimension.
$G(x)$	=	2-dimensional Gaussian function in spatial domain.
$G(\omega)$	=	2-dimensional Gaussian function in frequency domain.
C	=	Covariance matrix.
$\phi(\omega)$	=	Phase spectrum of the 2D Gaussian model.
ρ	=	Centroid Vector of the 2D Gaussian model.
T	=	Inertia tensor
θ	=	Orientation Vector of the 2D Gaussian model.
$\mathbb{H}_{20}(\Theta, a)$	=	Second order of Hermite Polynomial.
$K(f, g)$	=	Kullback-Leibler Information.
MST	=	Maximum Spanning Tree
$\mathcal{L}(., f)$	=	Likelihood function.

Chapter 1

Introduction

1.1 Medical Image Analysis and its Challenges

Medical image processing and analysis covers a broad number of areas, including image acquisition, image reconstruction, image enhancement, image compression and image-based visualization. The area of medical image analysis, broadly speaking, can be defined as including the development of the following methodologies: image segmentation, image registration, motion tracking from image sequences and the measurement of anatomical and physiological parameters from images [1].

With the advances in imaging technology, diagnostic imaging has not only become an indispensable tool in medicine today, but by generating large data

sizes and volumes, it has become more and more difficult for human observers to visually evaluate the image contents, and therefore, computer aided automated assessment is becoming essential in clinical planning, diagnosis and treatment.

Over the past decade or so, a variety of image acquisition devices have been developed for clinical or biological tasks. The first imaging modality used in clinical radiology was X-rays, discovered by Röntgen, which is an electromagnetic radiation of very high frequency. A film is taken during the exposure time to record the shadow of the structures along the path of the rays [2]. Since the discovery of X-rays, many new imaging modalities have been developed. These can be broadly categorized into two groups; anatomical and functional.

Anatomical modalities mainly include X-ray, CT (computed tomography), MRI (magnetic resonance imaging) and US (ultrasound). Other popular techniques derived from the original modalities, include MRA (magnetic resonance angiography), CTA (computed tomography angiography), fluorescein angiography and digital fundus angiography.

Functional modalities mainly comprise fMRI (functional MRI) and nuclear medicine imaging modalities which include SPECT (single photon emission computed), PET (positron emission tomography), doppler-ultrasound imaging, perfusion and contrast agent studies in MRI CT and Ultrasound

(US) images [3].

The requirements of medical image analysis vary widely and depend upon the tomographic nature of the image data. Consequently, many medical image analysis algorithms are specialized to particular image modalities. For example, in the CT image (figure 1.1(a)), x-rays are used at different angles to produce a cross-sectional image so that underlying soft tissues can be displayed with enhanced contrast as well as the bony structures. The contrast between different features is determined by the differential absorption amounts of X-rays by neighbouring structures [4]. Depending upon the type of detector used, CT reconstruction images are directly or indirectly dependent on the photon counting statistics that are inherently Poisson in nature. Normally it can be assumed that the noise contained in CT images is stationary and white, but the presence of a structure, such as a bone can significantly alter the counting statistics through which the rays travel, compared with the projection in areas of soft tissue. In addition to these effects, shot noise in the detectors and quantisation noise while sampling the detector output also need to be considered [5].

Figure 1.1(b), is a picture of the left kidney taken by ultrasound imaging. Ultrasound uses high frequency sound waves to construct an image rather than the traditional electromagnetic radiation x-ray. This means that it is a safe, non-invasive way of creating cross sectional images of the human body [6]. An acoustic wave is launched into the body using a hand held

transducer, the wave interacts with tissue and blood, some of the transmitted energy then returns to the transducer to be interpreted by the ultrasound machine. If the velocity of propagation in the tissue being interrogated is known, the distance from the transducer at which the interaction occurred can be determined. The characteristics of the return signal (amplitude, phase, etc) provide information on the interaction and hence they give some indication on the type of medium in which it occurred [7]. The technology enables the observation of the movement of organs, their 3D structure and microvasculature, however, ultrasound images have very low signal-to-noise ratio (SNR) compared to most other medial imaging modalities. Furthermore, since it is usually applied to soft deformable tissue which is not homogeneous, there are variations in the speed of sound as an acoustic wave travels through the tissue causing image distortion. In addition, waves from individual transducer array elements propagate via slightly different paths to a target, and thus have different delay characteristics introduced by the non-homogeneity, which cause imprecision in the focusing process. All these characteristics make the development of signal processing techniques that have to deal with low signal-to-noise ratios (SNR) and are able to correct aberration caused by non-homogeneous tissue a very challenging task.

A magnetic resonance image (MRI) of a human knee is shown in figure 1.1(c). MRI provides high-resolution images of internal structure through non-invasive means and has been used extensively in medial diagnosis and

treatment planning. It uses a series of magnetic field gradients and radio frequency pulses to encode the position and composition of molecules within a tissue volume. These excitation sequences are used to scan a volume in a sequence of slices by sampling the 2D spatial Fourier domain of the slice. An inverse Fourier transform is then used to reconstruct images of the tissue composition within each slice [8]. There is an intrinsic tradeoff between field strength, resolution, acquisition time and SNR. Achieving a desired SNR at high spatial resolution requires longer acquisition time. The acquisition time, unfortunately, is limited in practice due to constraints such as patient comfort and by physical limitations arising in dynamic applications. Therefore, there is a practical limit on the SNR of the acquired MRI data in most applications and a noise reduction algorithm is often used. MR images also contain distortions and spurious features that are collectively described as artifacts. Therefore, some efforts to characterise and reduce these artifacts form a part of most of the image processing algorithms for MRI data [9].

The last type of imaging modality in this set of images (figure 1.1 (d)) is a digital fundus angiography of the human retinal eye. Fundus angiography is a non-invasive technique widely used in ophthalmic practice to examine the pathological changes of the retinal blood vessel tree. This technique aids diagnosis and monitors a variety of eye diseases, such as, diabetes, hypertension and glaucoma. To obtain the angiography image, the eye is dilated with eye drops and a special fundus camera is used to focus on the fundus

through the pupil to produce high resolution digital images. Despite the high resolution of such photographs, it is difficult to detect the blood vessels and quantify geometric changes automatically due to the low contrast between the blood vessels and the retina background. Other pathological patterns known as exudate may also interfere with the automatic blood vessel detection algorithms [10].

The diversity of the above imaging methods and the range of diagnostic applications make medical image analysis become a multitudinous algorithms and methodologies ranging from 2D image alignment [11] to volumetric feature analysis [12]. Despite this, it is instructive to classify the underlying requirements for medical image analysis in general.

A major task of medical image analysis is the extraction of an appropriate feature description to describe the meaningful content or structure of the image data including organs, anatomical features (e.g. blood vessels, tissues) and pathological features (e.g. exudate, tumour) which are often regarded as *segmentation* tasks from an image processing point of view. A successful medical image analysis application needs to be able to produce reliable results on not only normal structure and function, but also on abnormal, pathological or diseased states.

During the past decade or so, a variety of algorithms have been developed to solve both general and object-specific segmentation problems. The tech-

Figure 1.1: (a) A CT image of child's head after craniofacial surgery (b) Ultrasound image for left kidney (c) MRI for human knee (d) Digital fundus angiography for human retina

niques can be, broadly speaking, classified into histogram thresholding [13], edge based segmentation [14], intensity-based region growing [15], basic decision tree (minimum spanning tree) [16] statistical clustering approaches, Bayesian approaches [17], and neural network approaches [18]. In addition,

some multi-resolution algorithms that use Pyramids, Wavelets, the Multi-resolution Fourier Transform (MFT) [19] and Scale Space theory [20] have been developed to improve the immunity against noise and address the fundamental idea that relevant medical image features appear at a variety of *scales* within the same image data set.

The work presented in this thesis focuses on the branching structure analysis for medical image data. An important application of branching structure segmentation has been in the area of detecting vasculature in retinal images [21]. The complex branching structure of the human vasculature can be examined using angiography imaging and quantitative analysis can be performed on the 2-D blood vessel tree to evaluate tree structure and help physicians assess pathological conditions. The clinical background and challenges of this application are discussed in greater detail in the remainder of this chapter. Another application of branching structure analysis is on 3D CT data for measuring the human airway tree [22]. This application is also discussed in the concluding chapter of the thesis as an extension of the presented work.

1.2 Clinical Background to Retinal Imaging

1.2.1 Anatomy of the Eye

The adult eyeball is almost spherical, with an average diameter of 2.0 cm. It includes three membranes, the cornea and sclera, the choroid and the retina. (figure1.2)[1].

The cornea is a tough, transparent tissue which covers the anterior surface of the eye that admits and refracts the light. Continuous with the cornea, the sclera is an opaque membrane that provides shape and protects the inner parts. The retina (nervous tissue) is the inner coat of the eye. It is the beginning of the visual pathway and lines the inside of the wall's entire posterior portion. It is a thin film of nervous tissue attached to the optic nerve which is a bundle of nerves tissue connecting the eye with the brain.

The inner part of the eye's posterior portion (including the optic disc, fovea, the retina tissue and the vasculature) is called the ocular fundus. The visualization and documentation of the ocular fundus has been of great interest to doctors and scientists for many years since it is an important diagnostic indicator for many eye disease, such as, diabetes, hyper-tension and glaucoma.

[1] From Schepens Retina Associates Foundation

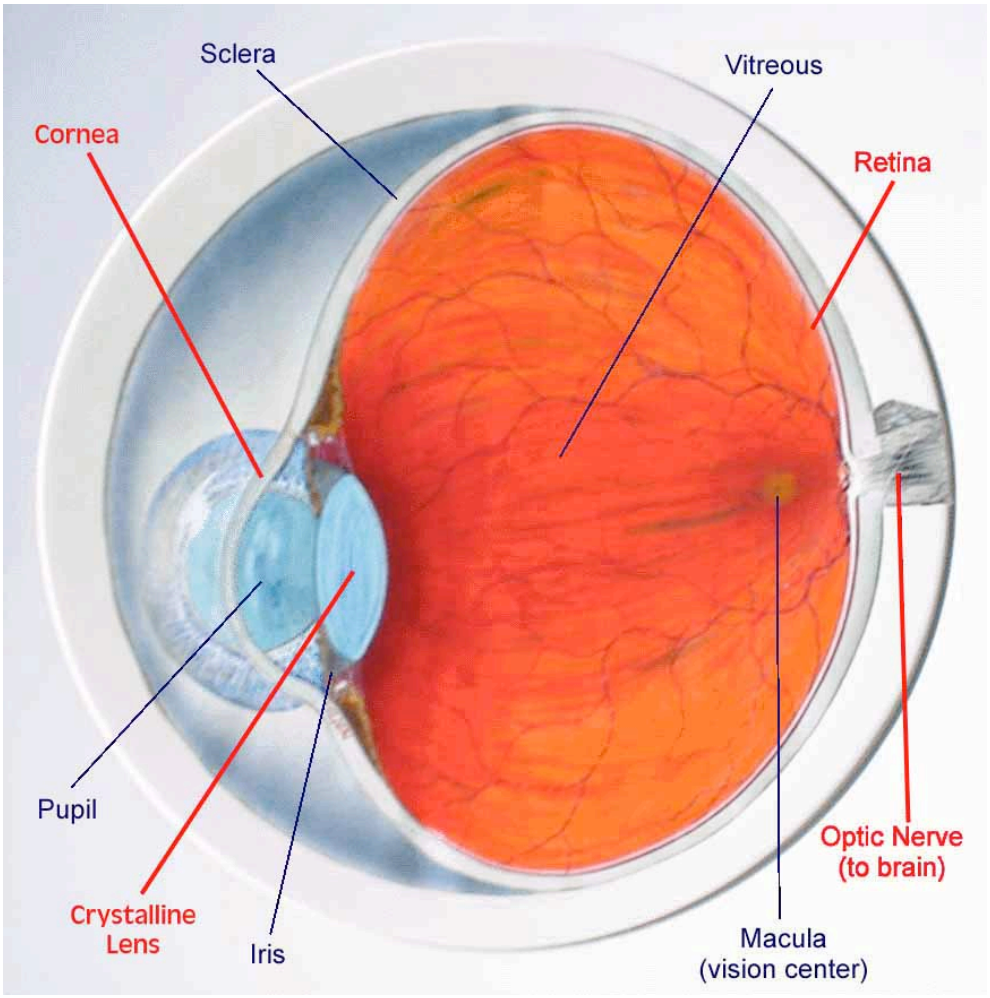

Figure 1.2: Diagram of the human eye viewed from the side

1.2.2 Image Acquisition

Different imaging techniques are presently being employed by the ophthalmologist to observe the ocular fundus and facilitate the quantification of structural changes in retinal blood vessels.

Angiography is one of the common procedures in ophthalmic practice. There are several different image acquisition techniques, such as X-ray, MR, fluorescein and indocyanine green angiography, for different types of eye disorders. Fluorescein angiography is a widely used diagnostic test since there are no harmful forms of radiation involved. The technique consists of a coloured dye injection into a vein in the arm of the patient. The dye travels through the circulatory system and reaches the vessels in the retina after 8-10 seconds. The vasculature and its distribution can then be captured by a special digital fundus camera [23]. Fluorescein angiography may detect and quantify changes in the blood vessels geometry more accurately than direct ophthalmoscopy due to the high contrast between the blood vessel and background retina layer (figure 1.3 (a)). However, it is not suitable for certain people because of allergic reactions.

A non-invasive technique, widely used in clinics, is retinal fundus photography. The pupil is dilated with eye drops and a special fundus camera is used to focus on the fundus and acquire high resolution digital images. Because of the wide field of view, the image is not perfectly in focus in certain areas. Furthermore, despite the high resolution of these photographs, contrast between the blood vessels and retinal background tends to be very poor (figure 1.3 (b)). Therefore, it is reasonable to draw the conclusion that accurate vessel segmentation on a digital fundus image is more difficult compared to the same task in a fluorescein angiograms where the higher contrast

and narrow field of views make for far better images [24].

(a)

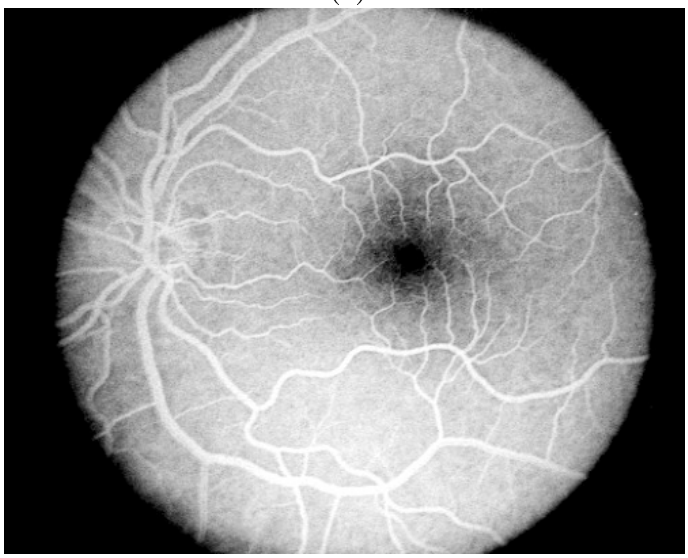

(b)

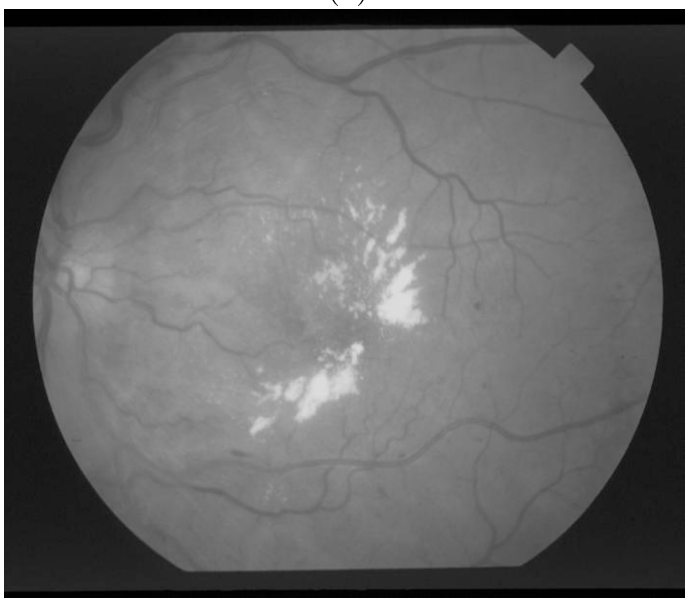

Figure 1.3: (a) Fluorescein Angiogram (b) Digital Fundus Retina Image

1.2.3 Motivation for Automatic Analysis of Retinal Images

Pathological changes of the retinal vessel tree can be observed in a variety of diseases such as diabetes, hyper-tension and glaucoma. An ophthalmologist examines the vascular modifications by direct inspection (ophthalmoscopy) or by manually analysing from the ocular fundus photographs. The routine inspection of fundus images can be a laborious and tedious process and may be prone to human error.

For example, in studies of the disease retrolental fibroplasia, the width of the vessels are examined over time. Human measurement of vessel width is subjective and can produce imprecise results. In contrast, automatic computer examination would provide far more objective, precise and repeatable measurements. Another example of problems with ophthalmic analysis is the measurement of tortuosity, which can be used to judge the severity of a disease, is subjective and imprecise. Again, computer calculations can provide the ophthalmologist with a numerical measure of vessel tortuosity.

Although the underlying mechanisms for some eye diseases are not fully understood, its progress can be inhibited by early diagnosis and treatment. However, since symptoms often occur only in the later stages of the disease, it is extremely difficult to identify the disease in its early stage. Automated vasculature measurement could reduce both the expenditure of resources in

terms of specialists and examination time and provide an objective, precise measurement of retina blood vessel structure and other pathologies. Given the above clinical needs, any automated system should be able to satisfy the following goals:

1. Isolate principal retinal features such as the optic disc and fovea.
2. Automatically detect certain pathologies such as hard exudate and lesions.
3. Detect blood vessels (arteries and veins) with good accuracy (localisation) and efficiency (high recognition percentage, low false negatives, low false positives).
4. Locate bifurcations and measure the width of the blood vessels.
5. Other geometrical and topological parameters related with the branching patterns of the entire blood vessel tree should be measured in order to quantify the changes in structure from a global point of view.

1.2.4 Objectives

The first step in computer analysis of ophthalmic images is segmentation of the vasculature. Accurate blood vessel segmentation is fundamental in the analysis of fundus images as further analysis usually depends on the accuracy of this segmentation. It allows a quantitative measurement of the

geometrical changes of arteries, in diameter, tortuosity or length and can provide the localisation of landmark points, such as bifurcations, needed for image registration [25]. Furthermore, it can be used to measure the size of the optic disc and fovea and estimate the leakage of blood into the retina (exudate) that can indicate retinal disease and diabetes [26].

The vasculature has several distinct characteristics that can be used by image processing techniques to separate blood vessels of interest from unwanted interference.

- The vessel cross-section intensity profile along their width approximates a Gaussian shape for fundus images.
- The orientation and grey level of a vessel do not change abruptly, they are continuous.
- Vessels connect to form a binary tree-like structure.
- The vasculature is approximately piecewise linear, it can be represented by connected lines.

However there are a number of factors that may obstruct the vessel segments.

- The shape, size and grey level of blood vessels vary hugely.
- Some background features have similar attributes to vessels.

- `Vessels crossing and bifurcations can confuse some techniques.`

The main goal of this work has been to develop a branching structure segmentation and detection which can be used for detecting blood vessel structures in retinal images. To achieve this goal, we developed a vessel modelling technique that operates directly on the image intensities for detection of the blood vessels. Bifurcations are identified explicitly by the model. To account for changes in scale of the features of interest, a block-based multi-resolution approach is employed followed by an EM type of optimisation scheme to estimate model parameters and a penalised likelihood measurement to perform model/scale selection. A deterministic graph theoretic approach and a stochastic Bayesian approach, are then employed for linking the features, i.e. vessel segments, bifurcations and inferring the global vascular structure.

1.3 Thesis Outline

In Chapter 2, the problem of segmentation of blood vessels in retinal images is addressed and a review of current vessel segmentation techniques is presented.

The local feature estimation and modelling process of the segmentation is detailed in Chapter 3. A multi-resolution, Gaussian based model and a iterative maximum likelihood type of algorithm is described to achieve an accurate local feature representation. A penalised distance measure Akakie

Information Criteria (AIC) is used to select the most appropriate model and scale for a given region. Experimental results are presented that illustrate the feature model and its performance.

Chapter 4 describes a *deterministic* neighbourhood linking strategy to explore a global inference of the entire blood vessel tree structure. The evaluation of these types of approach is also given along with experimental results. The second part of the chapter presents a *stochastic* Bayesian approach to draw inference of the global structure of vasculature tree to improve the deterministic algorithm discussed previously which is prone to becoming trapped in local maximum and being unable to explore less certain alternative explanations of the data.

The geometry parameters of the vasculature tree (e.g. tortuosity, width, branch angle etc.) are measured in Chapter 5. Segmentation results are also presented along with their evaluation in a form of receiver-operating characteristic (ROC) curve. Different approaches such as a Scale-space based region growing method and a probing algorithm using Matched filtering responses are also discussed for means of comparison.

Finally, Chapter 6 summaries the principal contributions of this work, and describes its merits and limitations. Some preliminary experiments and results on extending the algorithm into 3D are also discussed in the future work section.

Chapter 2

Review of Branching Structure Segmentation

Segmentation is a preliminary but important stage in most applications that use medical image data. It is a prerequisite step for quantification of morphological disease manifestations, for radiation treatment planning [27] [28], for construction of anatomical models [22], for content-based retrieval by structure [29] and for volume visualization of individual objects [28]. Blood vessel delineation on medical images forms an essential step in solving several practical applications such as diagnosis of the vessel stenosis blockage or malformations. It can also be used for registration of patient images obtained at different times. Segmentation methods often depend heavily on the imaging modality, application domain and other specific factors. There is no single

segmentation method that can extract vasculature from every medical image modality. With the rapid growth of digital angiography, many computer used algorithms have been presented to provide either automated or semi-automated detection of vascular structure. From an image processing point of view, vessel segmentation algorithms can be broadly grouped into [30];

- Pattern recognition techniques
- Artificial neural network-based approaches
- Artificial intelligence-based approaches
- Morphology based enhancement and detection

Some of these categories can be further divided into sub categories. Methods of each category will be discussed in length in the following sections.

2.1 Pattern Recognition Techniques

Edge and Ridge Based Detection Methods

Edge detection methods use the knowledge that a vessel is bounded by two parallel edges. Commonly used methods include, first or second order gradient operators, convolution kernels and morphological edge detectors [31] [32].

After applying the detectors, two anti-parallel edges can then be used to detect a vessel. The major problem with parallel edge tracking approaches is that false paths may be traced due to spurious gradients. Bifurcations, crossing points and the appearance of some other pathology features may also confuse the algorithm.

Ridge-based methods convert 2D gray scale images to a 3D surface with image intensity forming the third dimension. The algorithm starts from an arbitrary pixel in the intensity map and traces along the steepest ascent direction and locates ridge points at local maxima. Some applications using a graph description to extract the centreline of objects [33], in which the vessel tree is represented with a graph where each vessel keeps information about its relationship to other vessels.

In Guo's work [34], the image is pre-processed by a median filter followed by a non-linear anisotropic diffusion smoothing, as a noise removal step. A height map and a ridge detection process is then used along with an adaptive thresholding method to select the region of interest. Finally, the candidate vessel centerlines are connected together from the extracted ridges using a curve relaxation process. This process cuts the cost of the ridge extraction process as well as reduces the false ridges introduced by the image noise. However, the smoothing algorithm used in the pre-processing step may alter the actual shape/width of the blood vessels and is prone to produce errors in the vessel/non-vessel classification.

Liu and Sun [35], proposed a method of tracking the ridges by estimating the local vessel directions. First, an intensity height surface is created and from a user given initial ridge point, the associated ridge is found using a conjugate directions search with respect to the Hessian matrix. Second, the ridge is traversed once a ridge point is found and the widths of segmented objects are estimated using points on the ridges. Some accurate results of vascular trees are shown on MR angiograms, however, it requires a fair amount of user intervention and is not suitable for fully automatic vasculature detection.

Overall, due to the large regional variations in intensity inherent in retinal images and very low contrast between vessels and the background, particularly in the digital fundus images, techniques based on edge detectors and boundary tracing lack robustness in defining blood vessels without fragmentation [10].

Region Growing Approaches

Region growing, in its simplest sense, is the process of joining neighbouring pixels into larger regions subject to some predefined criteria. Two important segmentation criteria are *value similarity* and *spatial proximity* [36]. Two pixels can be grouped together if they have similar intensity characteristics or if they are close to each other. This section will briefly describe some of the general approaches grouped by their characteristic techniques.

In Single-linkage algorithms, each pixel is regarded as a node in a graph. Neighbouring pixels whose properties are similar enough are joined by an arc. The image segments are maximal sets of pixels all belonging to the same connected component. Using this method, the boundary of the vessel can be spatially detected accurately, however, the gap between edges can lead to excessive merging.

Instead of comparing the characteristics between neighbouring pixels, the Hybrid-linkage scheme seeks to assign a vector of properties to each pixel where the property vector depends on the $K \times K$ neighbourhood of the pixel. Similarity is established as a function of neighbouring pixel values and thus behaves better on noisy data.

Another technique, centroid-linkage, compares pixel values with the mean of an already existing but not necessarily completed neighbouring segment [37]. If its value and the segment's mean are close enough, then the pixel is added to the segment and the mean is also updated. If the means of the two regions are close enough, the two regions are merged and the pixel is added to the merged region. One drawback of this scheme is the dependence on the order in which pixels and regions are examined, i.e. a left-right, top-bottom sequence yields different initial regions as a right-left, bottom-up scan.

Some researchers proposed a method that combines the Hybrid-linkage with centroid linkage to take advantage of their relative strengths [15] [10].

By using centroid linkage, regions containing weak gradient areas can be accurately detected since the algorithm does not depend on a large difference between the pixel and its neighbour to declare a boundary. Centroid linkage is done only for non-edge pixels, that is, region growing is not permitted across edge pixels. A second pass, defined by the curvature scale-space representation, is made to locate borders between regions. Based on scale-space analysis from which the width size and orientation of blood vessels is obtained by using two main geometrical features based upon the first and second derivative of the intensity, i.e. edges and maximum principal curvature along the scale-space representation. A multiple pass region growing procedure progressively segments the blood vessels using the feature information together with spatial information about the 8-neighbouring pixels. The details of this algorithm along with its implementation results will be presented in chapter 5.

The main disadvantage of a region growing approach is that it often requires a seed point as the starting point of the segmentation process. This requires user interaction. Region growing can also be sensitive to noise, causing extracted regions to have holes or even become disconnected. Conversely, partial volume effects can cause separate regions to become connected. To help alleviate these problems, a homotopic region growing algorithm has been proposed that preserves the topology between an initial region and an extracted region [38]. Fuzzy methods have also been used with region growing

approaches [39].

Matched Filtering Approaches

Matched filtering approaches convolve the image with multiple matched filters for the extraction of objects of interest. It consists of a set of 2D kernels that are swept across the gray scale image, where each kernel models a piece of vessel at a certain orientation with a fixed Gaussian cross-section and a given length. The size of the convolution kernel effects the computational load of the filtering process. The output is an image with pixel values proportional to the best filter response. The filtering acts as a 'smart detector' of parallel lines with Gaussian intensity profile in between. Matched filtering has been used to emphasise vessels in a fundus image at [40] [41] [42] [43] and is usually followed by some other image processing operations like thresholding and then connected component analysis to get the final vessel segmentations.

In Hart's method [44], the filter designed by Chaudhuri [42] is applied to the green plane of an RGB image since it typically exhibits the greatest contrast between vessel and background. In this method, the filter is applied at 12 orientations over 180 degrees and the maximum response of these filters at each location is selected as the vessel segment edge. A thresholding and thinning process is then followed to achieve the binary image containing vessel segments. A linear classifier is used as the final stage to obtain the

classification.

Chen et al [45], proposed an orientation space filtering technique that represents the *space* by adding an orientation axis to the original image space. The orientation space representation is then treated as a continuous variable to which a tunable Gabor filter is used to represent lines at multiple orientations. After representing in orientation space, multiple orientation line detection is achieved by thresholding 3D images of the orientation space and then detecting the connected components in the resulting image. The algorithm is sensitive to the selection of the bandwidth for Gabor filters. It requires a trade off between sensitivity and selectivity for optimum multiple orientation line segmentation.

The matched-filter techniques possess many interesting features such as, robustness, no initialisation and user intervention is required, however, it is relatively time consuming as the convolution kernel used may be quite large and needs to be applied repeatedly. In addition, the kernels respond optimally to vessels that have a fixed σ, the standard deviation of the underlying Gaussian function, as the kernel. Therefore, they may output weak responses to thin vessels as well as very thick vessels. In addition, the vessels with high tortuosity may also be left out from the kernel response.

Template Matching

Template matching tries to recognise a structure model in an image. The template is used as a *prior* model and normally a top-down approach is used. In vasculature extraction applications, the vasculature tree template is usually represented in the form of a series of nodes connected in segments. The template is then deformed to fit the structures.

In Thackray and Nelson's work [46], the system uses an adaptive thresholding scheme to extract the vascular object from the intensity image and then eight templates with different angles to detect the orientation of vessel segments are applied. Like matched filtering approaches, it appears that the range of vessels width and orientation are limited by the pre-set templates.

In Klein's [47] work, a deformable spline algorithm was used to determine vessels and enhance their centerline features. Using a manually supplied initial location of the vascular entity, the system then applies a set of Gabor filters to determine the feature energy/orientation and deform the spline snake by minimising an energy function. The estimation of this approach can be very accurate but the amount of user intervention and the computational expense makes it impractical for detecting entire structures.

Other researchers have proposed a stochastic deformation process described by a Hidden Markov Model to achieve template deformation [48]. It combines a *priori* knowledge of the arterial tree in the form of mathemati-

cal templates and a stochastic deformation process is described by a hidden Markow model. The structure template is a set of connected nodes and their structural designations. The arterial tree from an image is extracted by deforming the structure model and calculating the likelihood estimation of the deformation. The recognition process is implemented using a dynamic programming technique.

Model-based Approach

Model based algorithms have similarities to the human cognitive process. They normally directly extract the required primitives from the unprocessed raw range images. Model based approaches can be broadly divided into two categories: deformable models (snake) and parametric models.

Deformable models are model-based techniques employed for finding object contours using parametric curves that deform under the influence of internal and external forces. In theory, a snake is a set of control points, (sometimes called a *snaxel*), that are connected to each other. There is an energy associated with each pixel by a geometric function that defines such constraints as the smoothness or coherence of the contour, the closeness of the contour to image edge pixels and the compactness of the boundary [47]. These forces are known as the snake's internal and external forces, respectively. The snake's total energy can be represented by the following equation

using the internal and external energy:

$$E_{snake} = \lambda E_{internal} + (1 - \lambda) E_{external} \tag{2.1}$$

The internal energy is defined by the *snaxels'* relationships with their neighbouring pixels. It normally contains two components; elasticity and bending, where as, the external energy attracts a snake to image contours with large intensity gradients. An external energy is essential to halt snake minimisation. Without sufficient external force, eventually the internal energy will make the snake shrink down to a single pixel. Deformable models can generate smooth curves or surfaces that accurately fit the vessel edge, however, the amount of user interaction and computation required makes it impractical for extracting entire vascular structures.

In another type of model based approach, primitive geometric features are matched to the data. Normally, the estimations are checked and improved by some optimisation criteria. Local consistency is usually examined by employing some geometric constraints, e.g. distances, orientation of normals. Because of the introduction of robust statistics into some model-based methods, e.g. by EM algorithms, those methods are very robust to noisy or occluded data.

Due to the nature of retinal fundus images, models derived from Gaussian based functions are commonly used by a number of researchers to model the

vessel [49] [43] [50], including:

- A single Gaussian function.
- Two individual Gaussian functions displaced from each other.
- Two equal (twin) Gaussian functions displaced from each other.
- The difference of two Gaussian functions.

Depending on the image modality, one model may have better fitting performance over the other. As pointed out by Martinez [10], cross sections of blood vessels are more Gaussian shaped in fluorescein images than red-free images due to the difference of light reflex in the different acquisition method. Therefore, a single Gaussian function can produce a reasonable fitting in a fluorescein image but the result in a fundus image is relatively poor.

Gao [49], concluded that the difference of two Gaussian models is theoretically justified, it gives good performance in tests on red-free images and provides useful parametric information. Vessel width is calculated as the standard deviation of the outer Gaussian multiplied by a factor fixed across a group of images. However, modelling each vessel segment with two Gaussian functions doubles the computational cost. Furthermore, the variety of shapes and widths of blood vessels make the choice of the fixed factor problematic.

During the last decade or so, more and more researchers have adopted their methodologies into multi-scale approaches. [10] [51] [20]. Multi-scale approaches perform segmentation tasks at different image resolutions. Major structures, such as the large vessels are extracted in low resolution images while fine structures are extracted at high resolutions. It increases the processing speed and robustness. The curvature scale-space method is a commonly used multi-resolution algorithm in computer vision. As a means of comparison, a curvature scale-space method was implemented, which has been widely used on edge or corner detection problems in computer vision. The basic idea behind scale-space representations is to separate out information at different scales [52] for an image to be embedded in a one-parameter family representation which is derived by convolving the original image $f(\mathbf{x})$ with Gaussian kernels of increasing variance t. Under this representation, for a 2D image $f(\mathbf{x})$, multi-scale spatial derivatives can be defined as

$$S_{\mathbf{x}^p}(\mathbf{x}|t) = f(\mathbf{x}) * \mathcal{G}_{\mathbf{x}^p}(\mathbf{x}|t) \tag{2.2}$$

where $\mathcal{G}_{\mathbf{x}^p}$ denotes a derivative of some order p of a Gaussian kernel [52]. After the images at different scales p are obtained, features can be extracted at corresponding level depending on the size.

Another type of approach is based on the Multi-resolution Fourier Transform (MFT) algorithm, which was first introduced by Wilson [19]. Using the MFT representation, Davies proposed a modelling algorithm for linear,

feature, branching and corner detection [53]. The algorithm was aimed at detecting edges and corners of the objects. Based on this idea, a superposition of Hermite-Gaussian modelling in a multi-resolution framework is developed to model blood vessels. The model has the ability to handle blood vessels with a variety of shapes as well as branching points and bifurcations. It is cheap to compute and robust to noise. The detail of the modelling algorithm will be introduced in chapter 3.

Vessel Tracking Algorithms

Tracking-based methods utilize a profile model to incrementally track and segment a vessel. Tracking operations normally begin at a known position in the image and extracts the image features to recognise the vessel structure simultaneously by exploiting the continuity properties of the vessel [21] [43] [54].

A Hough Transform is used in [55], to locate the papilla in a retinal image. Starting from the papilla, an iterative tracing procedure is implemented which halts when the response to a one-dimensional filter falls below a given threshold. As pointed out by Hoover [56], a drawback of this approach is the proclivity for termination at branch points, which are not detected well by one-dimensional filters. Also, the success of the algorithm is reliant upon the starting points which must always be either at the optic nerve or at

subsequently detected branch points.

Hoover et al. [56], addressed this issue by proposing a method based on a two-dimensional matched filter response. A conservative high level thresholding is set followed by an interactive probing process. The probe examines the image in pieces, testing a number of region-based properties. If the segment is defined as a vessel, the constituent pixels are simultaneously segmented and classified. The approach of combining filtering and exploitation of connectivity constraints is very effective. The detail of this approach and implementation results are presented in chapter 5 for a comparison.

Liu and Sun [35], presented an adaptive tracking algorithm using a three stage recursive procedure. First, a segment in the vascular network is identified given a starting position and direction. Secondly, by filling it with the surrounding background pixel values, the detected segment can be deleted from the image. The detection-deletion scheme is issued to prevent the problem of tracking path re-entry in those areas where vessels overlap. At the final stage, all branch points are detected by the use of matched filtering along both edges of the vessel. The detected branch points are used as the starting points in the next recursion. The recursive procedure terminates when no new branch point is found. The algorithm results were compared with ground truth images and some false-negative errors were generated, but very few false-positive errors.

The tracking methods are inherently efficient in computation and can always provide a meaningful description of the vessel network. The disadvantage is that, it is insufficient to provide a complete segmentation and has difficulties when the vessel reaches bifurcations and crossing points. In Zhou's work [43], the algorithm tracks well along the main blood vessels but ignores the minor ones at the branching point. Some researchers have improved the algorithm by using an extended Kalman Filter type of prediction-correction to optimize the estimation of the next possible location of blood vessel segment [57]. As pointed out by [58], by adopting smoothness constraints, this technique achieves robustness at the cost of yielding artificially smoothed (distorted) vessel edges and can lead to substantial errors. Furthermore, these algorithms normally require user intervention and do not appear to be extensible to 3D extraction.

2.2 Neural Network Based Approaches

Another set of approaches use artificial neural networks (ANNs) for classification. ANNs represent a paradigm for machine learning and can be used in a variety of ways for image segmentation. The most commonly applied use in medical imaging is as a classifier. In this kind of method, the network can be treated as a collection of elementary processors. Each node takes a number of inputs, performs elementary computations and generates a single

output. Each node is given a weight and the output is a function of the weighted sum of the inputs. Pre-labelled angiograms are used as the training set to determine the network weights [59]. ANNs can also be used in an unsupervised fashion as a clustering method [60], as well as for deformable models [61].

Some researchers have applied Neural network approaches to ophthalmic image analysis [62]. Systems can be trained by a certain pattern, such as a collection of vessels, and can thus extract the vasculature. It can also be used to extract other features that appear in the image such as micro-aneurysms.

One problem associated with this type of approach is that learning heavily relies on the choice of training data. The size of the training data set also effects the learning process and ideally the training procedure should be rerun each time new training data is added to the set. These factors limit the effectiveness and utility of the algorithms.

2.3 Artificial-Intelligence Based Approaches

Another type of approach can be described as artificial-intelligence-based. These utilize knowledge to guide the segmentation process and to delineate vessel structures.

In Meaney's work [63], a rule-based expert system is used to segment

coronary vessels from a digital fundus image. The system extracts vessel segments as trapezoidal units using an OPS-5 production system. The rule set is used to determine which edge segments may participate in the formation of these trapezoidal strips and which segments arise from image noise. The system does not attempt to combine these units to form a complete vascular structure.

Bombardier et al [64] proposed two fuzzy segmentation operators for the automatic and reproducible identification of artery boundaries from angiogram images in a knowledge-based approach. Different segmentation operators are used to extract different anatomical structures. The two step segmentation process comprises the identification of the region of interest (ROI) and detection of the boundaries of the identified structures automatically. Fuzzy set theory is used to represent the knowledge.

2.4 Morphology based Enhancement and Detection

Mathematical morphology is a tool for extracting image components that are useful in the representation and description of region shape. Based upon the mathematical concept of set theory, this procedure is a powerful approach to many image processing tasks since *sets* in mathematical morphology repre-

sent the shapes of objects in an image.

Zana and Klein [65] proposed vessel identification using mathematical morphology methods. It assumes that the vessels are piecewise linear and that their cross-section is Gaussian-shaped. The image is first 'opened' with a set of linear structuring elements (15 pixels long, every 15 degrees) and then the small vessels (capillaries) are recovered after geodesic reconstruction. Additional operators are used to eliminate noise. The overall objective of this method is for image registration.

Figueiredo and Leitao [31] proposed a non-smoothing approach in estimating vessel contours in angiograms. The algorithm has two key features. First, it does not smooth the image so that the distortion introduced by smoothing or filtering can be avoided. Second, it does not assume a constant background which makes the technique well suited for a retina fundus image. Edge detection is performed by adapting a morphological gray scale edge operator. All local maxima of the morphological edge detector are considered as candidates for edge points. Dynamic programming is then used to find the minimum cost path around the candidates by selecting a pair for each cross section. Continuity and intensity terms are also used in the process of selecting candidate edge points.

Thackray and Nelson's work [46] discussed earlier can be also classified as a morphology based approach since the algorithm uses a combination of

mathematical morphology operations, 'opening' with a linear rotating structuring element and dual feature thresholding. As the first step, a rotating structure element is designed to be able to capture vessels with random orientation and certain size (mainly shorter capillaries). Some residual capillaries are visible along with dominating large vessels in the example images. Dual features of gray scale and intensity gradient magnitude threshold are then used to filter out the unwanted capillaries and other features. The algorithm can accurately measure segment categories of vessels in a vascular network, however it heavily relies on the selection of the structuring element, rotation angles and dual feature thresholding. Furthermore, the algorithm is used for the purposes of classifying the network into different categories, such as capillaries, larger vessels and non-vessels, and is not aimed at a complete segmentation of the vascular structure.

2.5 Summary

Vessel segmentation methods have been a heavily researched area in recent years. In this chapter, from an image processing point of view, some of the algorithms in the literature have been classified into four different categories, however, many algorithms use multiple techniques together to solve different segmentation problems.

Since there are large regional variations in intensity inherent in retinal

images, and very low contrast between vessels and the background, particularly in the red-free fundus images, techniques based on edge detectors and boundary tracing lack robustness in defining blood vessels without fragmentation. Techniques based on matched filters and template matching are difficult to adapt to the variations of width and orientation characteristic of blood vessels. Furthermore the smoothing/filtering process unavoidably alters the vessel profile. For the tracking based algorithms, as mentioned by Lalonde [66], the most common problem undermining the effectiveness of many algorithms concerns the handling of bifurcations. For example, Lecornu et al [67] describe vessel tracking as an optimization problem, where the two best paths between two vessel end points need to be recovered. The cost function to be minimized includes parameters related to edge contrast and parallelism, however no provision is made to detect and correct handling of bifurcations. Those algorithms rely on the 1D Gaussian intensity profile of the vessel, again tracking may ignore side branches or fail upon reaching a bifurcation [43].

It is for the above reasons that a parametric model-based approach has been proposed, which is less dependent on image intensity variation. Vessels with a large range of width and scale are also taken into account by using multi-resolution analysis. Bifurcation and branch detection are included within the algorithm by using a superposition of Gaussian models with the refinement of a Hermite polynomial to effect a difference of Gaussian profile.

An iterative EM type of optimisation step is used to reduce the estimation error and increase the robustness of the local feature modelling against uncertainty. In the final stage of the algorithm, two types of linking strategy, using a Kruskal minimum spanning tree and a Markov Chain Bayesian approach, are employed to explore the global vascular topology implied by the local structure.

In the next chapter, multi-resolution parametric modelling and the EM type of optimisation scheme will be described, followed by the model/scale selection strategy using an information criteria algorithm. Experimental results and a brief evaluation will also be presented.

Chapter 3

Multi-resolution Hermite Gaussian Modelling

3.1 Introduction

As mentioned by numerous researchers [10] [20] [68] [69], since real-world objects exist as meaningful entities over certain ranges of scales, any vision system handling objects of different sizes and at different distances requires a way to control the scales at which the object is observed [70]. Therefore, adopting a multi-resolution approach is a key aspect in global image analysis. This means that local region analysis has to be applied to regions of varying sizes to find the optimal scale to model particular features.

In this chapter, a multi-resolution model based estimation algorithm that operates directly on the image intensities at different scales is proposed to model local vasculature features. Regions are modelled locally as a superposition of Gaussian functions and an iterative ML estimation is used to derive their parameters. A penalized likelihood information measure, the Akakie Information Criteria, is then employed to choose the best *model* and *scale* for vessel segments.

Having compared the different channels of the original RGB image, we observed that the blood vessels appear in highest contrast against the background in the green channel. This is also the case for any exudate present. This observation is in agreement with other researchers (e.g. Chaudhuri [42], Lalonde [66]). We therefore, carried out our detection and modelling algorithm on the green channel of the RGB colour images (figure 3.1).

As noted in [71], the optic disc and exudate appear as bright patterns in colour fundus retinal images. Most of them contrast well against the background because the grey level variation caused by these patterns are often similar to that caused by the vessels, and the appearance of optic disc and lesions becomes one of the main reasons for the failure of vascular structure detection [24] [72]. A preprocessing step has to be carried out. Prior to the vessel detection, to remove the optic disc and exudate in order to reduce its interference on vessel segmentation.

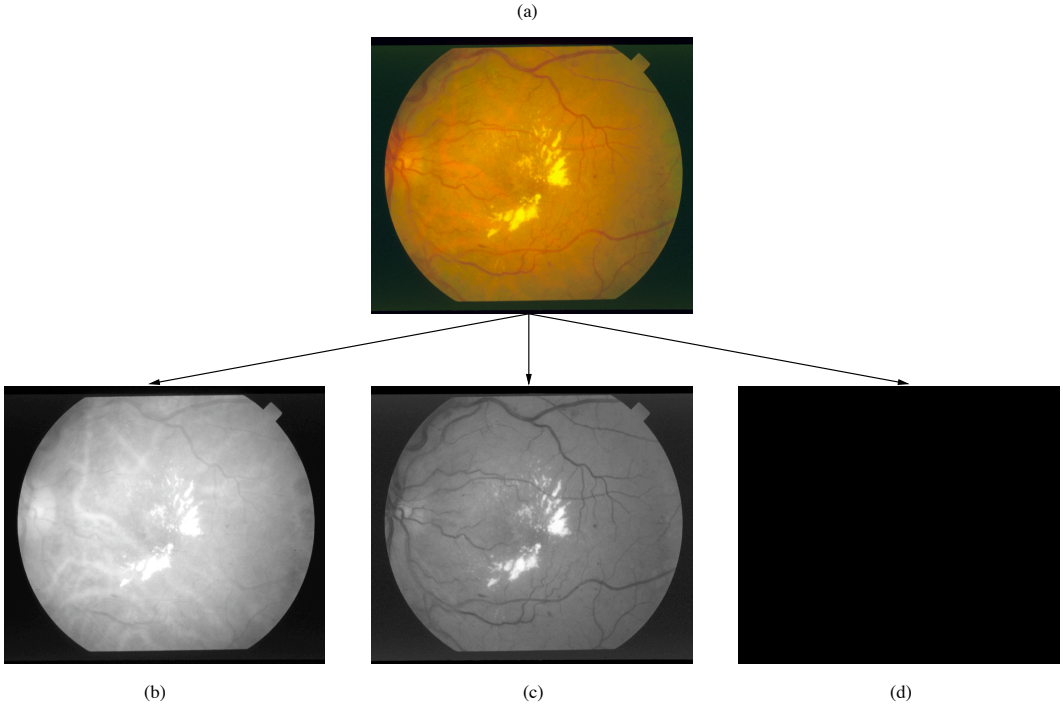

Figure 3.1: (a) A original RGB retinal image from the database. (605×700) (b) Red channel of the RGB image. (c) Green channel of the RGB image. (d) Blue channel of the RGB image.

3.2 Preprocessing

The optic nerve is one of the most important anatomical features in the human retina. It is the entrance of the retinal artery and central retinal vein. As shown in figure 3.2(a), it appears as a bright region in a circular area, roughly one-sixth the width of the image in diameter. Exudate will normally share the same intensity level as the optic disc, but with varied size and irregular borders (figure 3.2(b)).

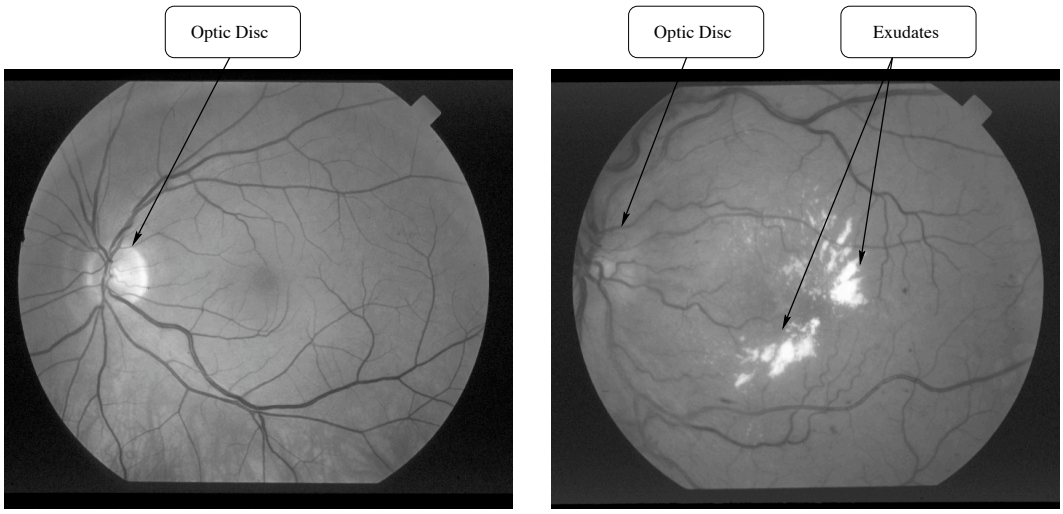

Figure 3.2: (a) A sample of healthy retinal fundus image (#IM0162). (b) A sample of fundus image with diabetic retinopathy (#IM0001). Image Size 605×700.

The work described in this section is concerned with the localization of both the optic disc and exudates. Since the aim is to remove these features from the retinal images, it is necessary to detect their exact contour as well as their position.

3.2.1 State of the Art

Researchers have taken different approaches to this problem. In Osareh's work [73], a colour normalization and contrast enhancement technique followed by fuzzy C-means clustering are employed, and neural networks are used for the vessel/nonvessel classification step. The results are shown to

work well, but the local contrast enhancement step may amplify noise in the image.

In [56], the optic disc is localized by using a fuzzy convergence algorithm to determine the origin of the blood vessel network. This approach needs a binary vessel segmentation result as input data, which can accumulate segmentation errors. No method is proposed for the detection of the contours and exudates.

In another type of approach [74], the circle Hough transform is used to detect the contours of the optic disc. The main weakness of this approach is that the performance of contour detection relies on certain specifications regarding the shape of the optic disc that are not always met. It is therefore not suitable for detecting exudates with irregular shape.

In this section, a morphological filtering technique is used to localize the candidate region of both the optic disc and exudates. The contours of the optic disc and exudate are determined by means of a morphological reconstruction technique [71]. This method was chosen over others [73] [56] [74], because of its effectiveness and simplicity, since the main purpose of this work is focused on the vascular structure.

3.2.2 Morphological Filtering

The basic morphological operators used in [71] are defined as:

- Dilation: $(f \oplus b)(x) = max_{b \in sB} f(x+b)$
- Erosion: $(f \ominus b)(x) = min_{b \in sB} f(x+b)$
- Opening: $f \circ b = (f \ominus b) \oplus b$
- Closing: $f \bullet b = (f \oplus b) \ominus b$

where f is the grey level image, b is a structuring element, B is a subset of the domain of f and s is a scaling factor. A geodesic transformation of an image f (marker) and a mask image m is also used in the reconstruction routine.

- Geodesic Dilation: $\delta_m^1 = (f \oplus b) \cap m, \delta_m^n = \delta_m^1 \delta_m^{n-1}$
- Geodesic Erosion: $\varepsilon_m^1 = (f \ominus b) \cup m, \varepsilon_m^n = \varepsilon_m^1 \varepsilon_m^{n-1}$

Note that regions containing exudates are characterized by a high local contrast. Firstly, the vessels are eliminated by using a closing operator $\mathcal{I}_1 = (f \circ b)$ with a circle structuring element b bigger than the maximum width of vessels (figure 3.3(a), 3.5(a)). The candidate region can then be found by thresholding and reconstructing the derivative of $\mathcal{I}_1$ (figure 3.3(b), 3.5(b)).

In order to find the contours of the exudates, all candidate regions are set to 0 in the original image and the morphological reconstruction is then calculated (figure 3.4(a), 3.6(a)). This operation propagates the values of pixels x next to the candidate regions into the candidate regions by successive geodesic dilation, with the original image f acting as the mask.

The contours of exudates and the main part of the optic disc are also obtained by applying a simple threshold operation to the difference between the original image and the reconstructed image (figure3.4(a), 3.6(b)).

3.3 Local Feature Analysis

The global shape of the retinal vessel structure (figure 3.7(a)), in general, cannot be modelled by a single primitive form, therefore any model can only represent the local shape of a vessel in a small region (figure 3.7(b), (e)). Here, we exploit the symmetry and translational invariance properties of the Fourier domain to model linear and branching structures.

The local feature models derived in this section are based upon the characteristics of local spectra. Any given image regions of varying sizes are modelled using their local spectra, and the model parameters are then estimated from the representation. This approach is based on the methods developed by Calway [75] and Davies [68], but have been extended in three

(a)

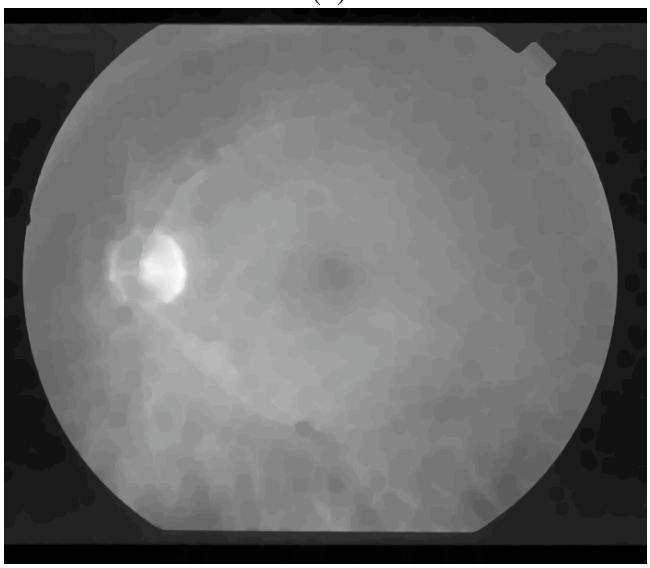

(b)

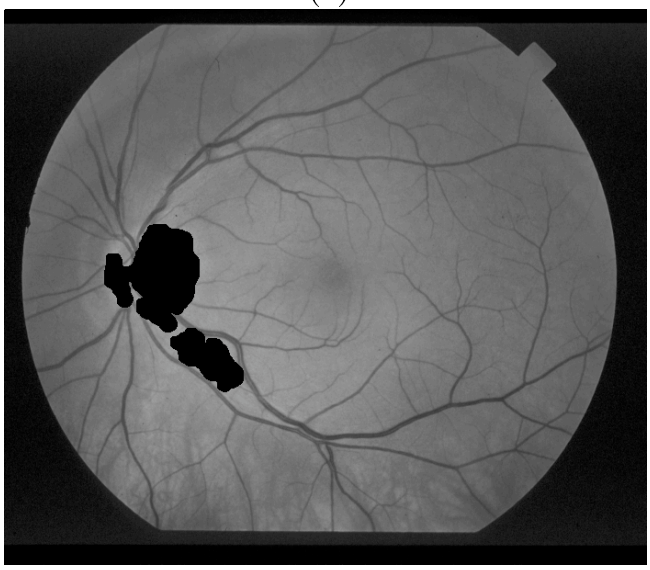

Figure 3.3: (a) Closing of the original image. (#IM0162) (b) Candidate region of the optic disc and exudates.

(a)

(b)

Figure 3.4: (a) Morphological reconstruction (#IM0162) (b) labelled contour of the optic disc and exudates.

(a)

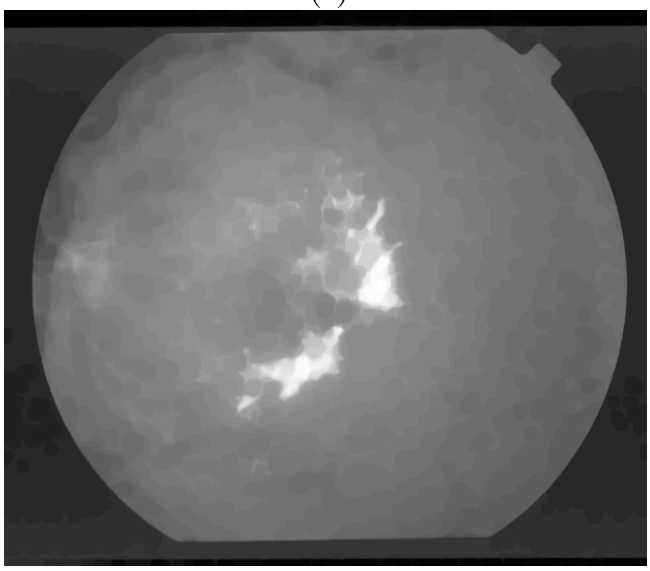

(b)

Figure 3.5: (a) Closing of the original image. (#IM0001) (b) Candidate region of the optic disc and exudates.

(a)

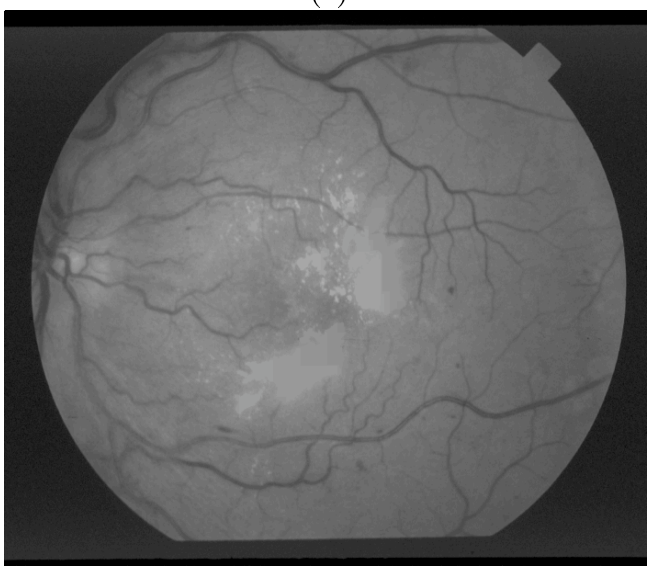

(b)

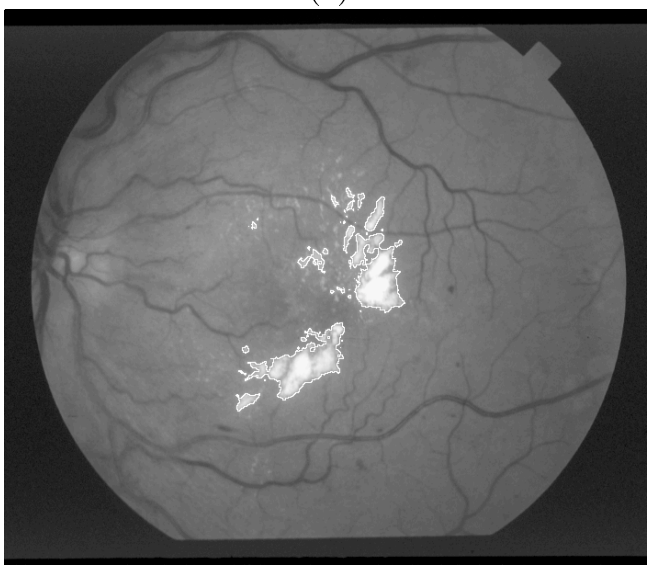

Figure 3.6: (a) Morphological reconstruction (#IM0001) (b) labelled contour of the optic disc and exudates.

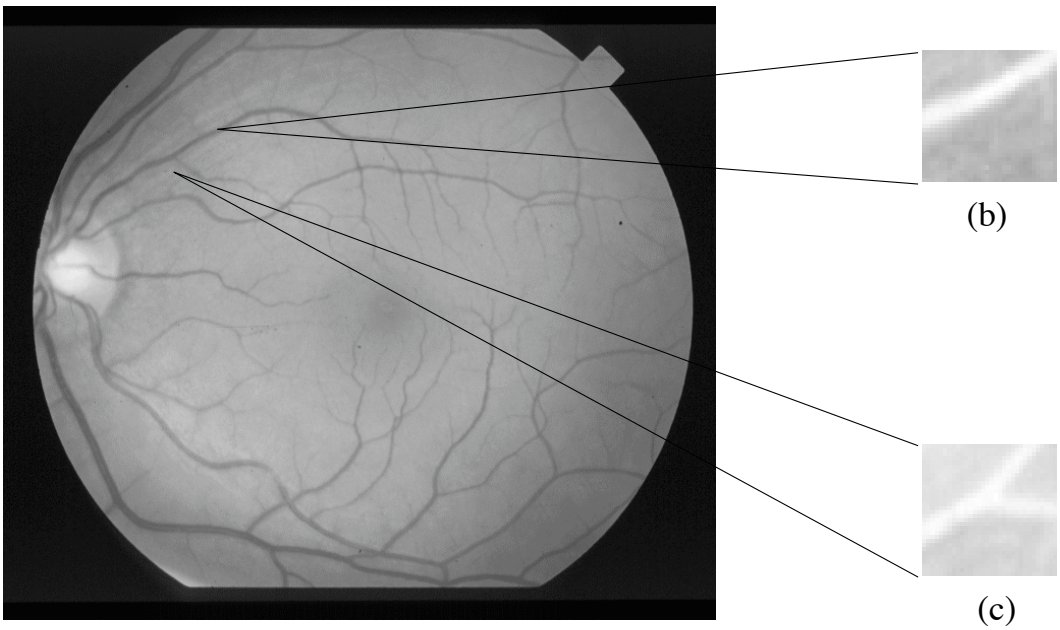

(a) Digital fundus retinal image (IM077)

Figure 3.7: (a) Sample of digital fundus retinal image (605×700). (b)-(c): Part of inverted grey level image.

main ways;

1. A Gaussian intensity model is used instead of a line model. The parameter set is extended from {centroid, orientation} to {amplitude, centroid, orientation, width and length}, therefore, the geometry of vessel segments can be modelled more explicitly.

2. Multiple features such as branches are modelled as a superposition of Hermite-Gaussian functions which describe the amplitude, position, and orientations of *intersecting* linear features. The centroids of component features are separated by applying K-means clustering to the

local Fourier phase and the covariances and amplitudes subsequently estimated by a likelihood maximization.

3. The algorithm has been extended to work on three dimensional data.

After the estimation of the parameter set, a penalised likelihood method is used to combine estimates from a range of scales in the framework of a multi-resolution image model. Details of the model estimation and model/scale selection algorithm are presented in the remains of this chapter.

3.3.1 Feature Modelling and Estimation

Prior to the modelling step, the background is subtracted using a simple piece-wise linear approximation since the background intensity variation is insignificant in local image regions.

$$F_{bg}(i,j) = b + a_x i + a_y j \tag{3.1}$$

where $\{b, a_x, a_y\}$ are coefficients of the piecewise linear polynomial (3.1) and obtained using a least-squares curve fitting. The result of background subtraction is shown in figure 3.9.

3.3.1.1 Gaussian Intensity Model

The main reason for choosing a Gaussian intensity model is if an ideal linear feature is windowed by a smooth function $w()$, and it can be regarded as a 2-dimensional Gaussian function [50]. Examples are shown in figure 3.9.

The 2-dimensional Gaussian function can be written in the form;

$$G(\mathbf{x}|\Theta) = Aexp(-(\mathbf{x}-\mu)^T C^{-1}(\mathbf{x}-\mu)/2) \tag{3.2}$$

where $\mathbf{x}$ is the spatial co-ordinate, ie.

$$\mathbf{x} = (x, y)^T \tag{3.3}$$

and $\Theta = \{A, \mu, C\}$ is the parameter set, μ is the mean vector and the covariance matrix $C = R^T V R$, where V is the diagonal matrix of variances and R is the rotation matrix.

$$V = \begin{pmatrix} \sigma_{x_1}^2 & 0 \\ 0 & \sigma_{y_1}^2 \end{pmatrix} \tag{3.4}$$

$$R = \begin{bmatrix} \cos(\theta) & \sin(\theta) \\ -\sin(\theta) & \cos(\theta) \end{bmatrix} \tag{3.5}$$

where θ is the angle to the x-axis. Figure 3.8 illustrates the meaning of the parameters used in the model.

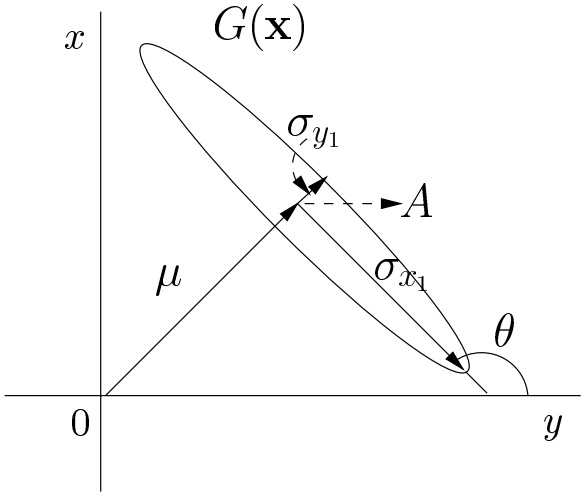

Figure 3.8: Parameters of Gaussian Model $G(\mathbf{x})$.

Another reason for using a Gaussian intensity function to model the data is because of its simple analytical properties. For instance, under any non-singular linear transformation, such as the Fourier Transformation, $-(\mathbf{x}-\mu)^T C^{-1}(\mathbf{x}-\mu)/2$, known as the *Mahalanobis distance*, keeps its quadratic form and remains positive definite. The Mahalanobis distance,

$$\mathbb{D}_x = (\mathbf{x}-\mu)^T C^{-1}(\mathbf{x}-\mu)/2 \tag{3.6}$$

in domain x, under a linear transformation $y = Ax$, becomes

$$\begin{aligned}
\mathbb{D}_y &= (A\mathbf{x}-\mu)^T C^{-1}(A\mathbf{x}-\mu) \\
&= (AA^{-1}(A\mathbf{x}-\mu))^T C^{-1}(AA^{-1}(A\mathbf{x}-\mu)) \\
&= (\mathbf{x}-A^{-1}\mu)^T A^T C^{-1} A(\mathbf{x}-A^{-1}\mu) \\
&= (A\mathbf{x}-\mu_A)^T C_A^{-1}(A\mathbf{x}-\mu_A)
\end{aligned} \tag{3.7}$$

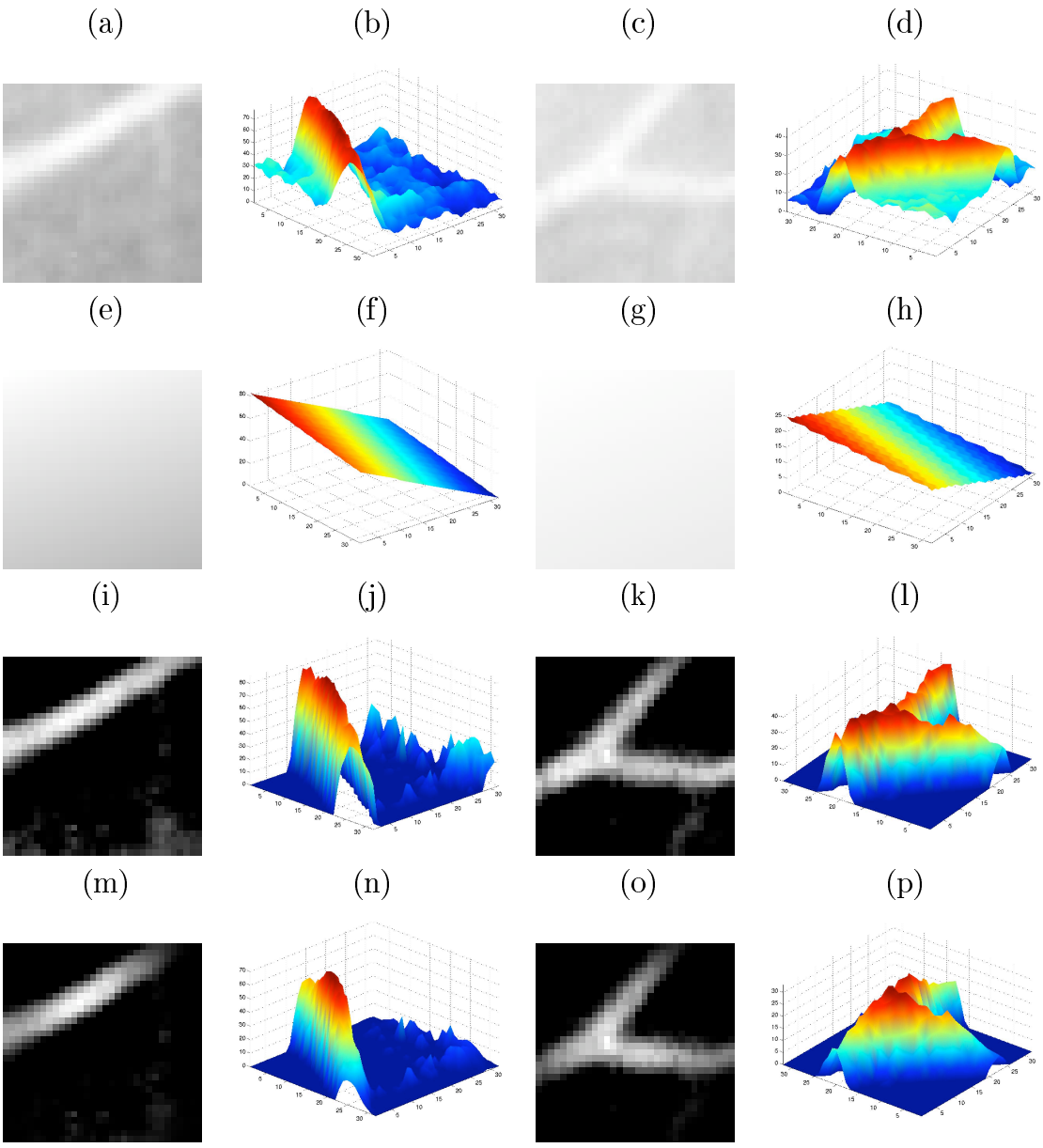

Figure 3.9: (a)-(d) Linear and branching feature with their intensity (e)-(h) Background modelled by piecewise linear (i)-(l) Subtraction of original and background data. (foreground) (m)-(p) Windowed foreground data.

Thus, the distribution remains Gaussian.

The Gaussian product theorem is another property which will be used when calculating the similarity between neighbouring feature blocks. The detail appears in length in chapter 4.

To estimate the parameters of our Gaussian model, a multi-resolution (windowed) Fourier Transform (MFT) is applied in each block before the feature extraction process;

$$Y(\omega) = \sum w(\mathbf{x}' - \mathbf{x}) y(\mathbf{x}) e^{(-j\mathbf{x}'\omega)} \tag{3.8}$$

where ω is the frequency co-ordinate,

$$\omega = (u, v)^T \tag{3.9}$$

and $w(\mathbf{x}' - \mathbf{x})$ is a window function used to localise the signal and avoid edge effects. The windowing function is based on a Hanning equation with parameters adaptive to the transformation scale, i.e. the block size (3.10). For any two neighbouring regions on the same or different levels, the windows in the overlapping area will sum to one.

$$w(\mathbf{x}' - \mathbf{x}) = cos^2(\frac{\mathbf{x}' - \mathbf{x}}{N}\pi) \tag{3.10}$$

Figures 3.10 & 3.11 show the magnitude spectra of the windowed Fourier transform at different block sizes (levels). For regions containing a single feature, the corresponding spectral energy lies orthogonal to the spatial orientation. For more complicated regions like branch points, there is a superposition of energies that have a less clear spectral structure.

3.3.1.2 Feature Centroid estimation

If it is assumed that there is only a single feature in one block, the position of the feature, i.e. the distance of its centre from the origin with respect to the origin of the image plane, is linearly related to the phase spectrum [76]. Denoting the phase by $\phi(\omega)$, the Discrete Fourier Transform can be represented as;

$$G(\omega) = |G(\omega)| exp[-j\phi(\omega)] \tag{3.11}$$

where $G(\omega)$ is the Fourier transform of the spatial image. For a single linear feature, the phase spectrum, $\phi(\omega)$, can be modelled as;

$$\phi(\omega) = -\rho \cdot \omega \tag{3.12}$$

where ρ is the centroid vector and can be calculated by taking the partial derivatives of the phase in each of the directions. In the discrete case, by taking the difference in phase between neighbouring coefficients, the centroid

(a) Original Image

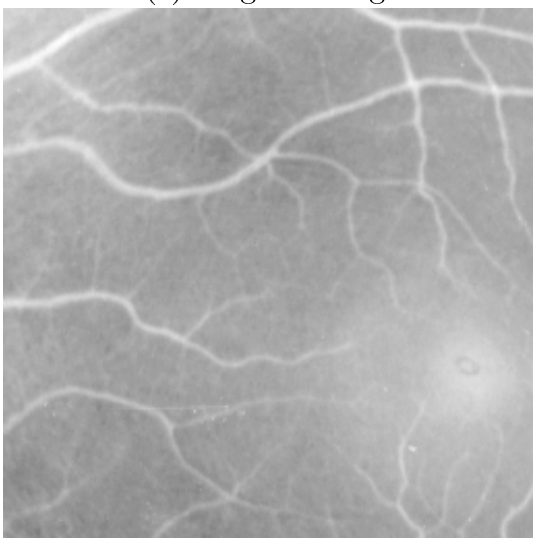

(b)Foreground $N = 64$

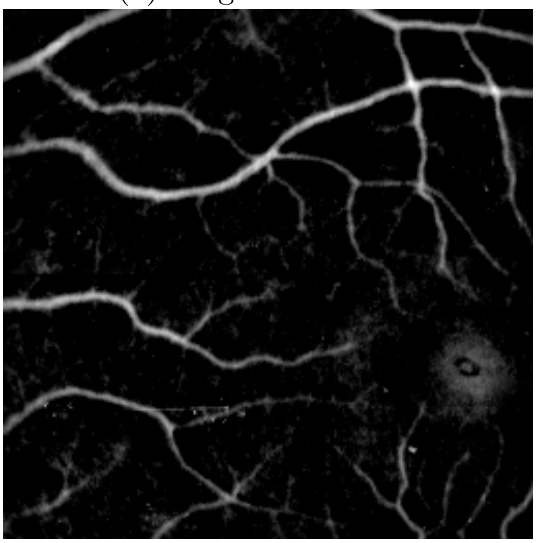

(e) Windowed Fourier Transform $N = 64$

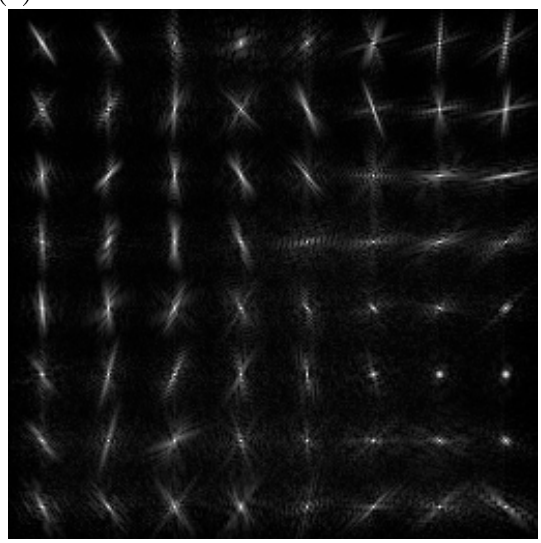

Figure 3.10: Windowed Fourier transform of an example foreground image and it's DFT Magnitude Spectra at level 64.

vector of spatial position can be estimated as;

$$\rho_i = \frac{N}{2\pi} \sum_{\omega} \hat{\phi}(\omega_i) \hat{\phi}(\omega_{i+1})^* \tag{3.13}$$

(c)Foreground $N = 32$ (f)Windowed Fourier Transform $N = 32$

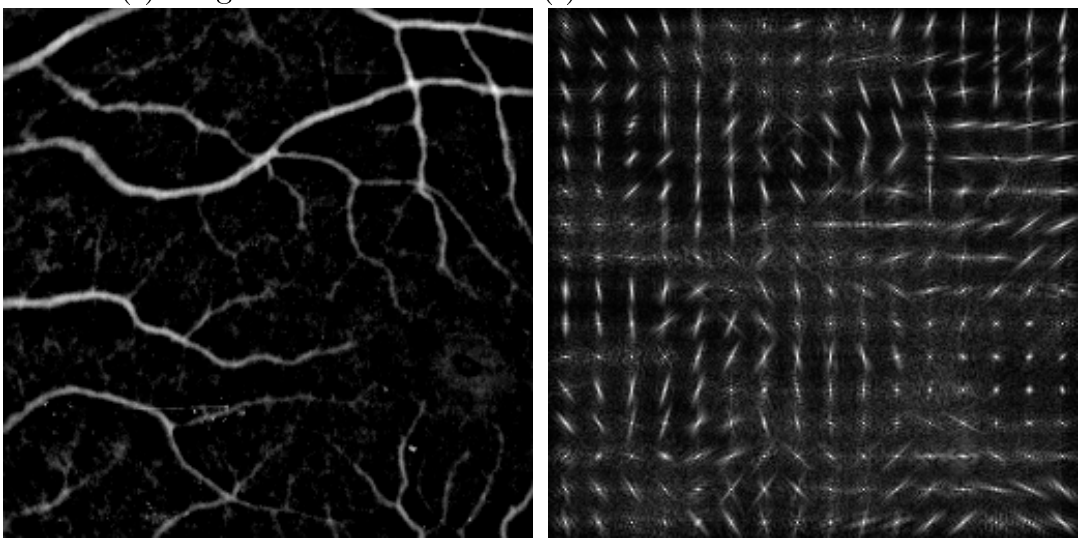

(d)Foreground $N = 16$ (g)Windowed Fourier Transform $N = 16$

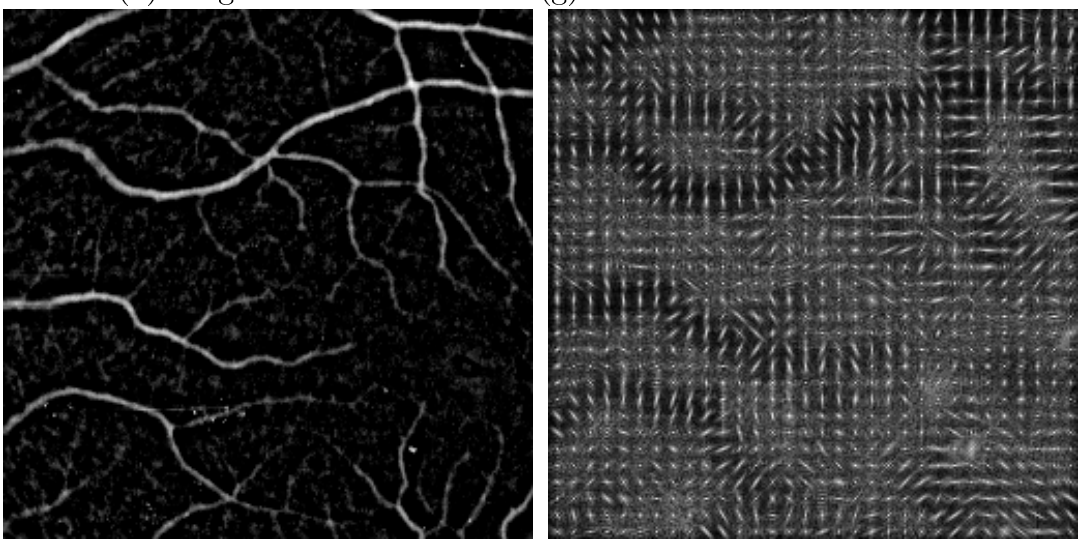

Figure 3.11: Windowed Fourier transform of an example foreground image and it's DFT Magnitude Spectra at level 32 & 16.

$$\rho_j = \frac{N}{2\pi} \sum_{\omega} \hat{\phi}(\omega_j)\hat{\phi}(\omega_{j+1})^* \tag{3.14}$$

where $\frac{N}{2\pi}$ is the sampling interval.

3.3.1.3 Orientation

The MFT block which was modelled with Gaussian intensity profiles may be considered as having energy in an ellipse, centred on the origin. From Borisenko and Tarapovs' work [77], a moment of inertia tensor T can be calculated using the energy spectrum in place of mass,

$$T = \begin{pmatrix} T_{00} & T_{01} \\ T_{10} & T_{11} \end{pmatrix} \tag{3.15}$$

$$T = \sum \frac{\omega\omega^T \hat{E}(\omega)}{||\omega||} \tag{3.16}$$

where N is the size of the block, the factor $||\omega||$ is used to reduce the greater emphasis to energy further away from the origin. $\hat{E}(\omega)$ is the normalised energy at a given point (u, v) in the block, ie.

$$\hat{E}(\omega) = \frac{|E(u,v)|}{E_{sum}} \tag{3.17}$$

where E_{sum} is the sum of the energy value in the block.

The major and minor axes of the ellipse are represented by the eigenvectors of the matrix. Since the orientation of maximum energy concentration, θ, is defined as the orientation of the major axis of the ellipse, it is indicated by the direction of the eigenvector, $\mathbf{e}_1$, which is associated with the largest

eigenvalue, λ_1, i.e.

$$T\mathbf{e}_1 = \lambda_1 \mathbf{e}_1 \tag{3.18}$$

where $\mathbf{e}_1$ is defined as

$$\mathbf{e}_1 = (e_{10}, e_{11})^T \tag{3.19}$$

The orientation can then be obtained from

$$\hat{\theta} = arctan(\frac{e_{11}}{e_{10}}) \tag{3.20}$$

3.3.2 Multiple Linear Feature Estimation

The ability to estimate blocks with multiple features is important since it provides the utility to identify bifurcations and crossing points which can be used for exploring the global vascular structure, or as landmark points in image registration algorithms [78].

If more than one linear feature is present in a block, in order to perform the estimation, it is necessary to segment the spectrum into components corresponding to each feature. The complete spectrum of the region is modelled as the sum of the spectrum of each cluster;

$$G(\omega) = |G(\omega)|exp[-j\phi(\omega)] = \sum_{l=1}^{K} |G_l(\omega)|exp[-j\phi_l(\omega)] \tag{3.21}$$

The use of the multiple linear feature modelling allows regions to contain junction points or corners.

A partitioning method, K-means clustering, is applied to separate the regions which are contributions from different features. K-means is an unsupervised, non-hierarchical clustering method, which is widely used in a number of image processing applications [79] [80]. It is an iterative scheme which attempts to both improve the estimation of the mean of each cluster and re-classify each sample to the closest cluster. Firstly, it randomly selects initial seeds which are equal to the required number of clusters. Next, each component is examined and assigned to one of the clusters, depending on the minimum distance. The centroid's position of each cluster is recalculated at each iteration until no more components are changing class.

1. *Initialise $k = 2$ classes, choosing k pixels' coordinates as initial centroid at random from the image. Make sure that the pairwise distance between the k distance is large enough.*

2. *Using the phase gradient $\phi_{i,j}$, convert each phase spectrum coefficient into a spatial vector $\mathbf{P}_{i,j}$. The sampling interval is $\frac{2\pi}{N}$ where N represents the block size. The spatial position is calculated by*

$$\mathbf{P}_{i,j} = \frac{N}{2\pi}\phi_{i,j} \tag{3.22}$$

Then, compare the distance between each pixel and each class centre

and assign coefficient to the class to which it is closest.

3. *Recalculate the centroid for each class.*

4. *Repeat from step 2 until the movement of the class centre is lower than a certain threshold t_m (we used $t_m = 2$ for a 128×128 image).*

From a statistical point of view, the K-means cost function can be written as

$$J = \sum_{n=1}^{N^2} \sum_{k=1}^{K} \gamma_{nk} \parallel x_n - \mu_k \parallel^2 \tag{3.23}$$

where $\gamma_{nk} \in \{0, 1\}$ such that $\sum_k \gamma_{nk} = 1$. Different colours are used in Figure 3.12 to show the clustering approach of the K-means algorithm in a given region that contains multiple features. After classifying the components belonging to each feature, the parameters of each feature can be individually estimated using equations(3.11)–(3.20).

3.3.3 Optimization Algorithm

The above Fourier based estimation is computationally efficient and accurate in noise free data. However, because of uncertainties in most real images, an optimization step is needed to improve the initial estimation Θ_0. An iterative Minimum Mean Square Error (MMSE) type of approach is employed

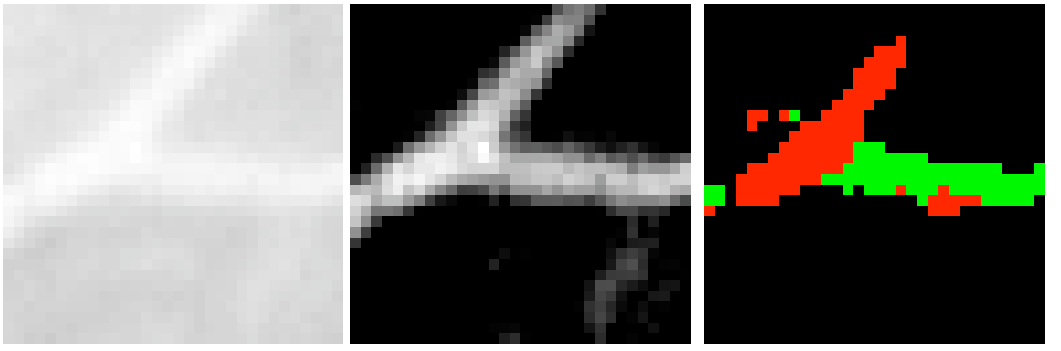

(a) Original Image (b)Foreground (c) K-means Classification

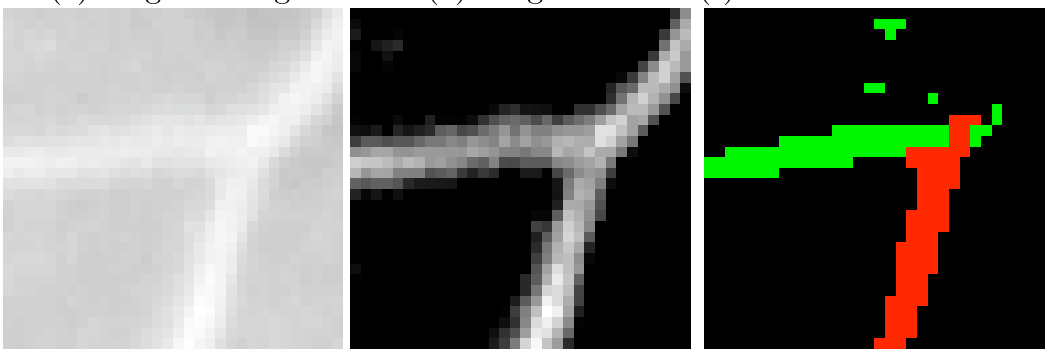

(d) Original Image (e)Foreground (f) K-means Classification

Figure 3.12: K-means classification for regions contain multiple features.

to minimise the error between model $G_m()$ and windowed data $f_B()$.

$$arg_{\Theta} min \sum_{\mathbf{x}} (f_B(\mathbf{x}) - G_m(\mathbf{x}|\Theta))^2 \tag{3.24}$$

which can be regarded as an error function.

This is equivalent to maximising the sample statistics Θ weighted by the inner product between the windowed data, $f_B(\mathbf{x})$, and the model $G_m(\mathbf{x}|\Theta)$.

The regression leads to a similar set of equations as the Expectation

Maxmisation (EM) algorithm. However, the conceptual basis between this approach and the EM algorithm is rather different.

The EM algorithm is an elaborate technique for finding the maximum-likelihood estimate of the parameters of an underlying *distribution* from a given data set when the data is incomplete or has missing values. It is often used when optimising the likelihood function is analytically intractable, but the likelihood function can be simplified by assuming the existence values of additional but *hidden* parameters [81].

Unlike the EM however, this estimation implicitly takes into account the spatial arrangement of the data $f_B(\mathbf{x})$ relative to the intensity model $G_m(\mathbf{x}|\Theta)$ whereas EM estimates the underlying distribution from which $f_B(\mathbf{x})$ are drawn.

The algorithm first calculates the expected value of equation $Q()$, defined as;

$$Q(\Theta, \Theta^{(t)}) = E[\sum_{\mathbf{x}} G(\mathbf{x}|\Theta) W(\mathbf{x}|\Theta^{(t)})] \tag{3.25}$$

and

$$G(\mathbf{x}|\Theta) = Aexp(-(\mathbf{x}-\mu)^T \Sigma^{-1} (\mathbf{x}-\mu)/2) \tag{3.26}$$

$$\sum_{\mathbf{x}} W(\mathbf{x}) = f_B(\mathbf{x}) G_m(\mathbf{x}|\Theta^{(t)}); \tag{3.27}$$

where $\Theta^{(t)}$ are the current parameter estimates that we used to evaluate the expectation and Θ are the new parameters that we optimise to increase Q.

A modified form of the maximisation step is used, instead of maximising $Q(\Theta, \Theta^t)$, to find some $\Theta^{(t+1)}$ such that, $Q(\Theta^{(t+1)}, \Theta^{(t)}) > Q(\Theta, \Theta^{(t)})$.

The second step of the algorithm is to maximise the expectation we computed from equation 3.25. i.e.

$$\Theta^{(t+1)} = arg_{\Theta} max Q(\Theta, \Theta^{(t+1)}) \tag{3.28}$$

Taking the log of Equation 3.25, we get;

$$log(Q(\Theta^{(t+1)}, \Theta^{(t)})) = \sum_{\mathbf{x}} (-ln\frac{1}{\sqrt{2\pi}} - \frac{1}{2}ln(|\Sigma|) - \frac{1}{2}(\mathbf{x}-\mu)^T\Sigma^{-1}(\mathbf{x}-\mu))W(\mathbf{x}|\Theta^{(t)}) \tag{3.29}$$

By taking the derivative of the function 3.25 with respect to each parameter in set Θ and setting it equal to zero, we can derive a set of iterative equations;

$$A^{(t+1)} = \frac{\sum_{\mathbf{x}} W(\mathbf{x}|\Theta^{(t)})}{\sum_{\mathbf{x}} G^2(\mathbf{x}|\Theta_{(t)})} \tag{3.30}$$

$$\mu^{(t+1)} = \frac{\sum_{\mathbf{x}} W(\mathbf{x}|\Theta^{(t)})\mathbf{x}}{\sum_{\mathbf{x}} W(\mathbf{x}|\Theta^{(t)})} \tag{3.31}$$

$$\Sigma^{(t+1)} = \frac{\sum_{\mathbf{x}} W(\mathbf{x}|\Theta^{(t)})(\mathbf{x}-\mu_t)(\mathbf{x}-\mu_t)^T}{\sum_{\mathbf{x}} W(\mathbf{x}|\Theta^{(t)}))} \tag{3.32}$$

The proofs are presented in Appendix A.

Convergence is achieved rapidly in 7-10 iterations. Figure 3.13 illustrates

estimates of two type of linear features in part of a 2D retinal fundus image for single and multiple Gaussian models. In figures 3.14 and 3.15, the estimation is tested in a larger region. Note that the parametric description of the model Θ has information about feature amplitude and width together with position and orientation.

3.3.4 Hermite Approximation

As mentioned above, one of the main reasons of choosing a Gaussian intensity function as the model is that the intensity profile of blood vessel segments are approximately Gaussian in shape after the subtraction of the piecewise linear approximation of the background and applying a Hanning window to the region 3.9 (b) & (l). However, as reported by other researchers [49], [10], in some special cases, the intensity profile of some large vessel segments is not exactly Gaussian due to the so called 'central light reflex' caused by specular reflection (see figure 3.16). Note that this happens more frequently in digital fundus images since the light reflex is comparatively larger than in fluorescein images [10].

For the above special cases, Gaussian intensity modelling tends to over-segment the features. Gao *et al.* [49] proposed an algorithm which uses the difference of two separate Gaussian functions to model each blood vessel segment. The model is able to fit the data well, however, doubles computational

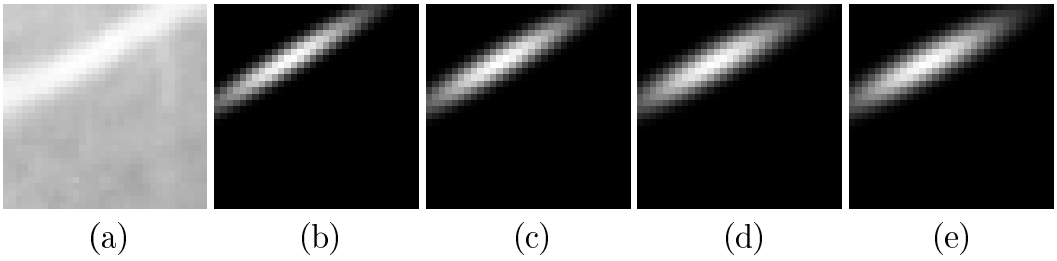

(a) (b) (c) (d) (e)

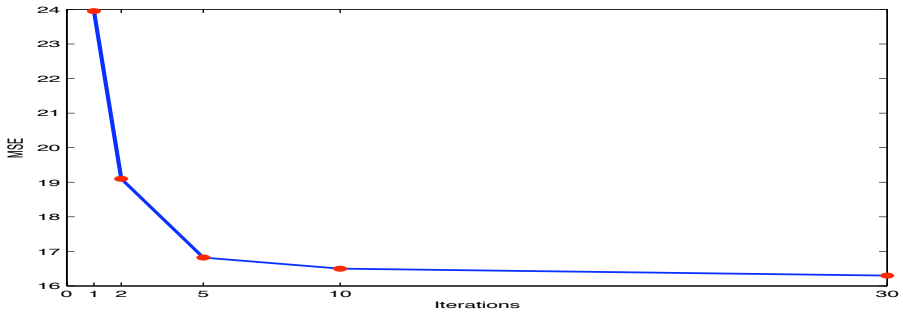

(f) Mean Square Error (MSE) Plot

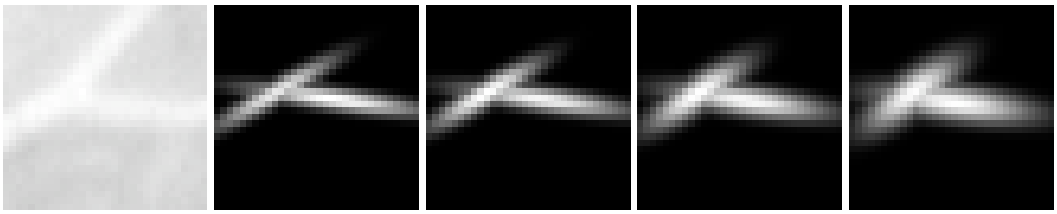

(a2) (b2) (c2) (d2) (e2)

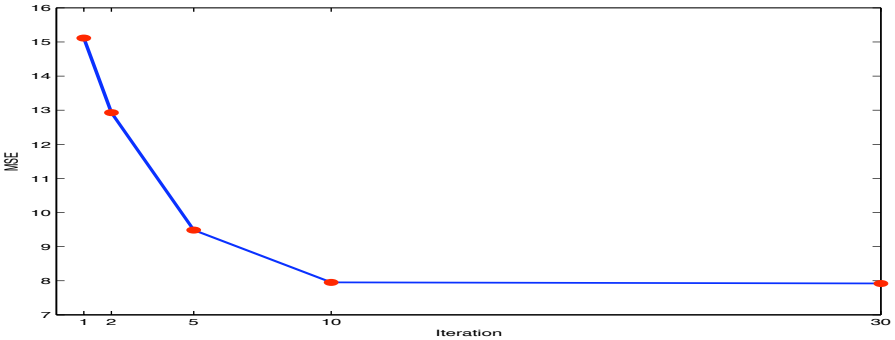

(f2) Mean Square Error (MSE) Plot

Figure 3.13: Optimisation result (Iterations $1, 2, 5, 10$) for single and multiple Gaussian models.

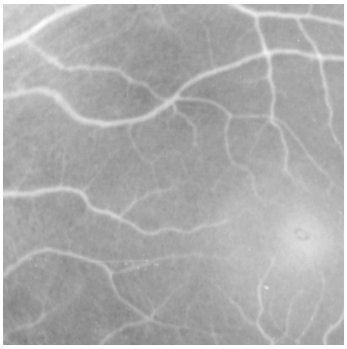

(a) Part of the original retina image

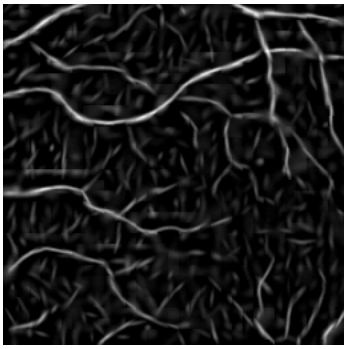

(b) Iterations 2

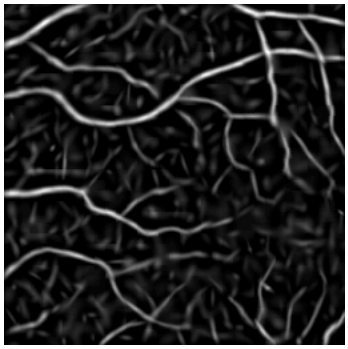

(c) Iterations 5

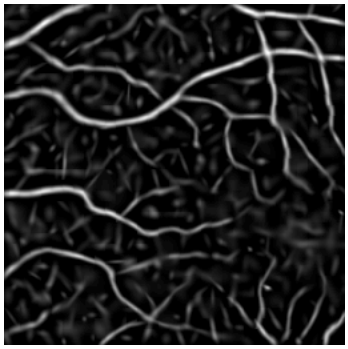

(d) Iterations 10

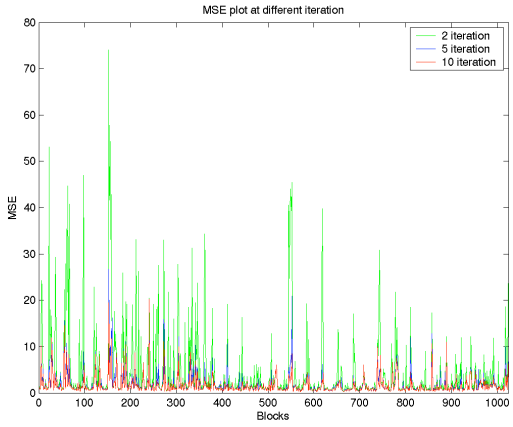

(e) Mean Square Error (MSE) plot for different iterations.

Figure 3.14: Optimisation result for (Iterations 2, 5, 10) using single Gaussian model.

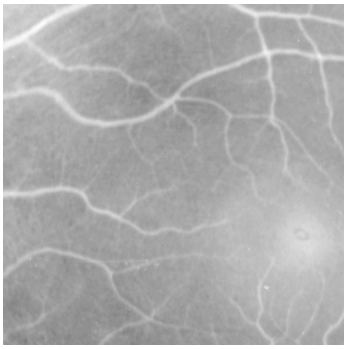

(a) Part of the original retina image

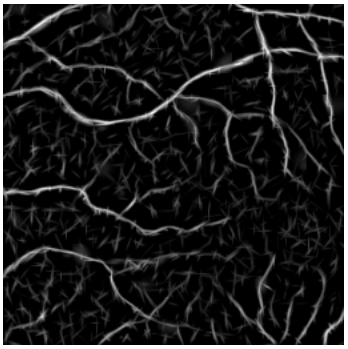

(b) Iterations 2

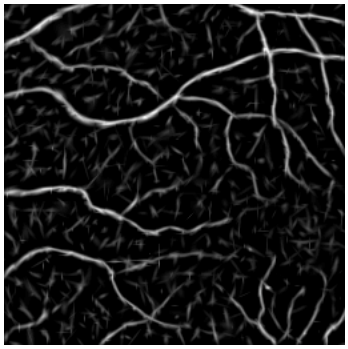

(c) Iterations 5

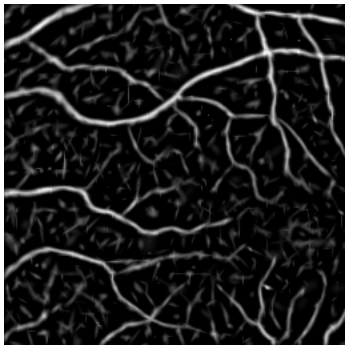

(d) Iterations 10

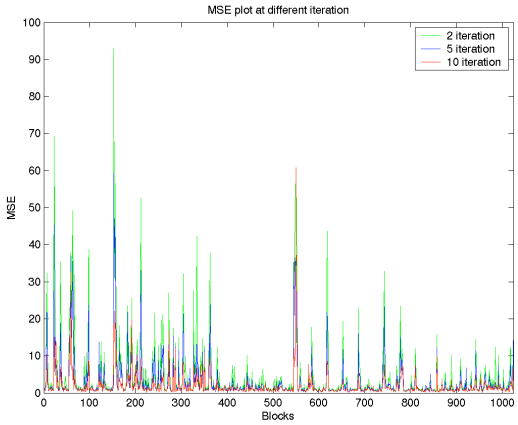

(f) Mean Square Error (MSE) plot for different iterations.

Figure 3.15: Optimisation result for (Iterations $2, 5, 10$) using multiple Gaussian model.

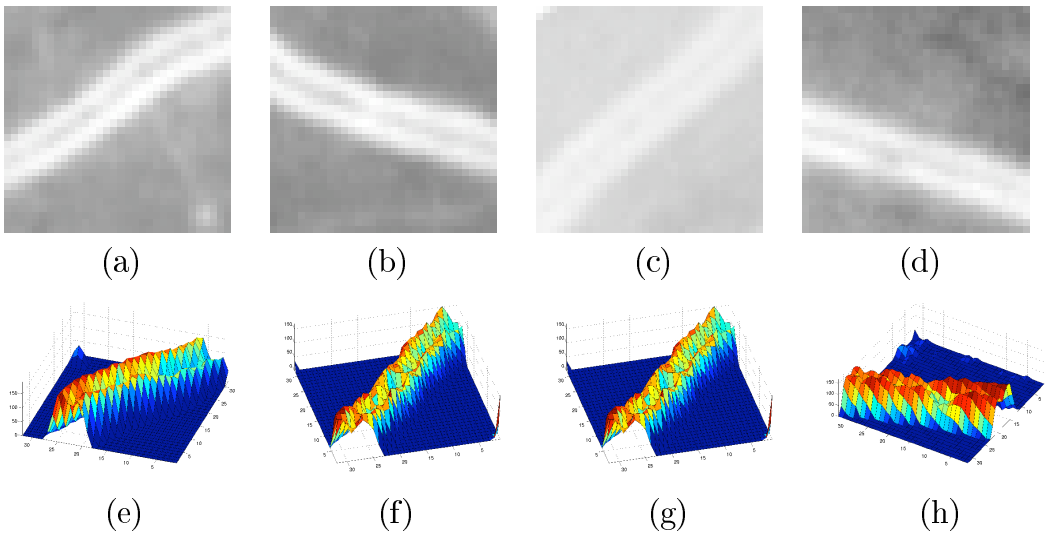

Figure 3.16: Samples of centre light reflex (a)-(d) and their 3D intensity view after background subtraction (e)-(h).

complexity since the number of parameters is doubled.

Our approach to solve this problem uses a *Hermite* approximation applied after the above optimisation scheme which introduces only one additional parameter [82]. The 1d *Hermite* polynomial is defined as;

$$H_n(x) \equiv e^{x^2/2}(x - \frac{d}{dx})^n e^{-x^2/2} \tag{3.33}$$

By Cartesian separability, its 2D extension can be represented as;

$$\mathbb{H}_{mn}(\Theta, a) = H_n(x)H_m(y) \tag{3.34}$$

Here, a second order *Hermite* polynomial $H_{2,0}(x)$ is used with an adaptive

parameter a as a factor that is multiplied by the optimized Gaussian $G(\mathbf{x}|\Theta)$, i.e.

$$\mathbb{H}_{2,0} = (1 + a(x^2 - 1))G \tag{3.35}$$

We can see from figure 3.17, a 1D plot of equation 3.35 with different a, that when $a = 0, \mathbb{H} \equiv G()$ and the two peaks are further apart when a increases. Note that a remains as a scalar parameter perpendicular to the orientation of the Gaussian when we perform 2D modelling.

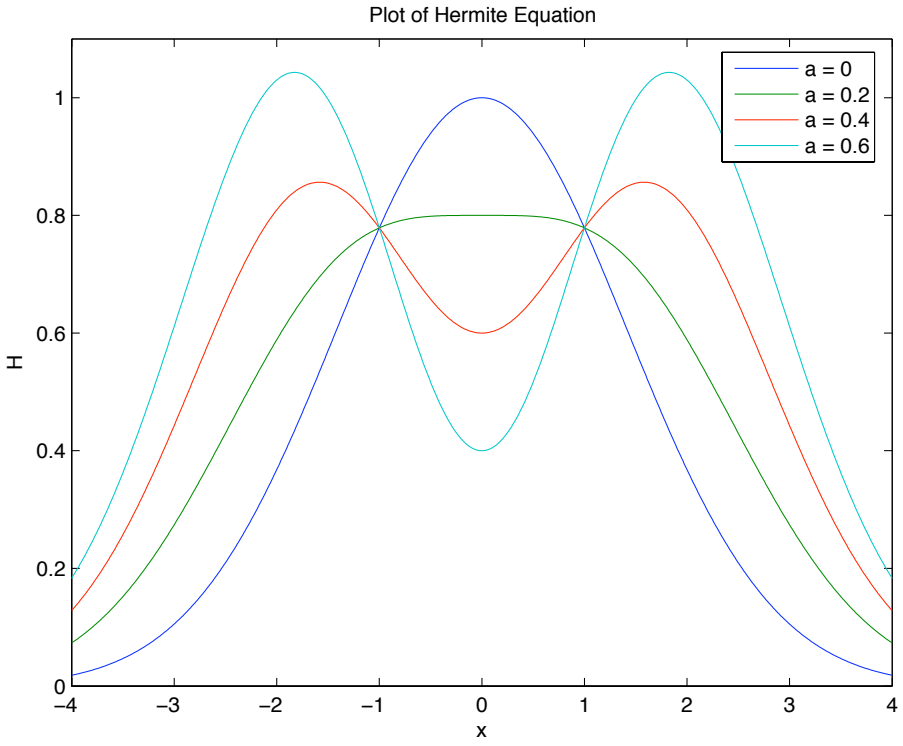

Figure 3.17: Plot of 1D *Hermite* equation with different a.

The estimation results of four sample images are shown at figure 3.18. From the MSE comparison result, we can see that more accurate approximation can be derived by using a *Hermite* equation rather than a simple *Gaussian* formula.

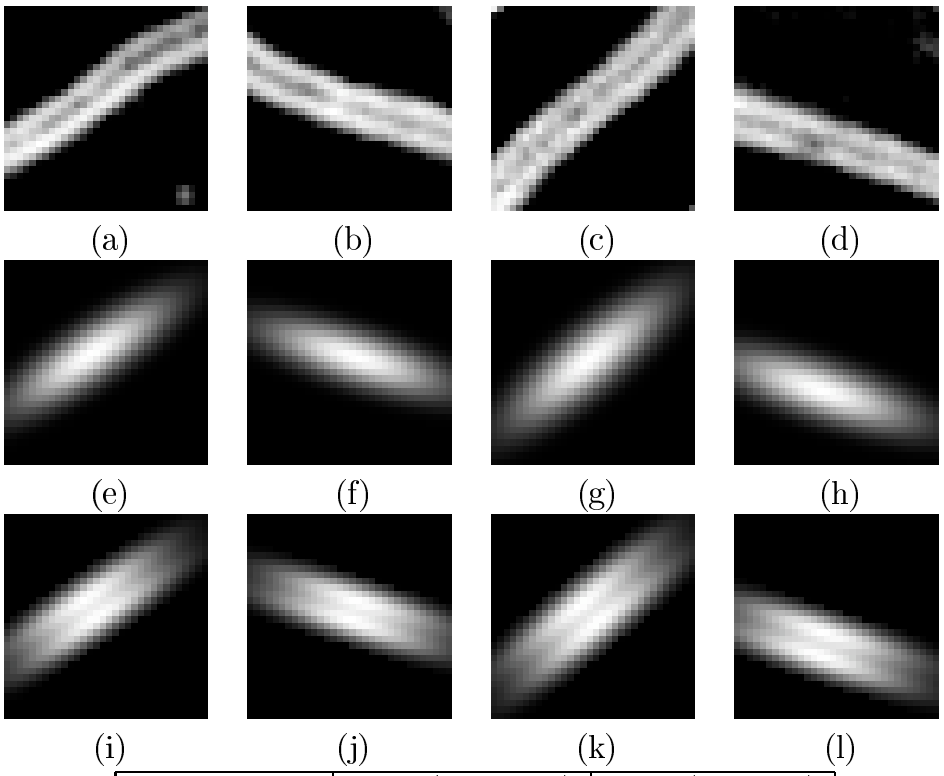

Sample Block	MSE (Gaussian)	MSE (Hermite)
1	12.2	10.1
2	12.5	5.8
3	4.1	2.3
4	6.2	4.4

(m)

Figure 3.18: Example images after background subtraction (a)-(d) Reconstruction results using *Gaussian* function (e)-(h), Reconstruction results using *Hermite* function (i)-(l) MSE table shows better fit using *Hermite* equation (m).

3.4 Multi-resolution Feature Analysis

So far, we have discussed the basic tools for modelling a given region with a fixed window size, each of which provides a view of just a small portion of the image. However, what size should these windows be? We have different models $m = 1, 2$ handling one or two linear features. However, there might be any number of features present and each of these could be from any of the feature classes, and the complexity of these regions could be well beyond the limits of the model. A way to deal with this, is to allow the window size to vary independently of the feature model. The model and scale can then be selected to fit the data best. It requires the accuracy of the hypothesis to be assessed to determine the most fit model and the optimal scale at which to model a particular feature.

The model and scale selection involves a trade off. On one hand, choosing a smaller region or using a multiple feature model ($m = 2$) will generally gain a better fit of the data. However, this will increase the variance (uncertainty) such as noise influence and also the computational cost since there are more model parameters to estimate.

On the other hand, choosing a larger region or simpler model ($m = 1$) will use less uncertain data and require a lower computational cost. Furthermore, it results in a compact representation of the feature which can be of particular importance when the features are used for coding [83]. However, it generally

has a worse fit of the data as each local model explains a larger part of the image.

As suggested by Box and Jenkins [84], the principle of model selection *"...using the smallest possible number of parameters for adequate representation of the data"* is needed from a statistical point of view. The principle of model selection is a bias versus variance tradeoff. In general, bias decreases and variance increases as the number of parameters increases. The fit of any model, generally, can be improved by increasing the number of parameters. However, a trade off with the increasing variance must be considered in selecting a model of inference [85].

The technique described in this work, following Calway's [75] and Bhalerao's [86] method, uses a hierarchical quad-tree structure to perform feature estimation at different levels, i.e. different window sizes. Then a Kullback-Liebler type of penalised distance measure, the Akaike information criteria (AIC) is used to bias the likelihood function with the number of parameters P.

The advantages and drawbacks of a quad-tree structure and the detail of the model selection procedure will be discussed in the next section.

3.4.1 Hierarchical Feature Analysis

The aim of the hierarchical analysis is to select the appropriate model and scale of representation for all regions of the image. The image is firstly estimated using multiple feature models $m = 1, 2$ over a predetermined range of levels B_l, starting at B_{l1} and descending maximally to level B_{ln}. If the block sizes at each scales, l, are chosen to increase by a factor of two, ${B_l}^2 = 2^l$, then each four 'child' blocks, $\mathbf{c_0} = (2i, 2j, l)$, $\mathbf{c_1} = (2i+1, 2j, l)$, $\mathbf{c_2} = (2i, 2j+1, l)$, $\mathbf{c_3} = (2i+1, 2j+1, l)$, will correspond to one 'parent' block $\mathbf{p} = (i, j, l+1)$ at the next level and forming a quad-tree feature representation of the data which is introduced by Klinger [87]. Unlike a traditional top-down fashion of quad-tree structure, however, we use a bottom-up grouping approach:

1. Without making decisions on whether the measures for a local image region are good or not, feature estimation is first carried out at every scale.

2. The process starts at finer scales of the image and merges each four 'children' blocks to one 'parent' block according to the scale selection criteria (see figure 3.19).

A bottom-up type of approach like this is better for exploring fine features but requires more computation than a top-down technique that can prune out subtrees during selection.

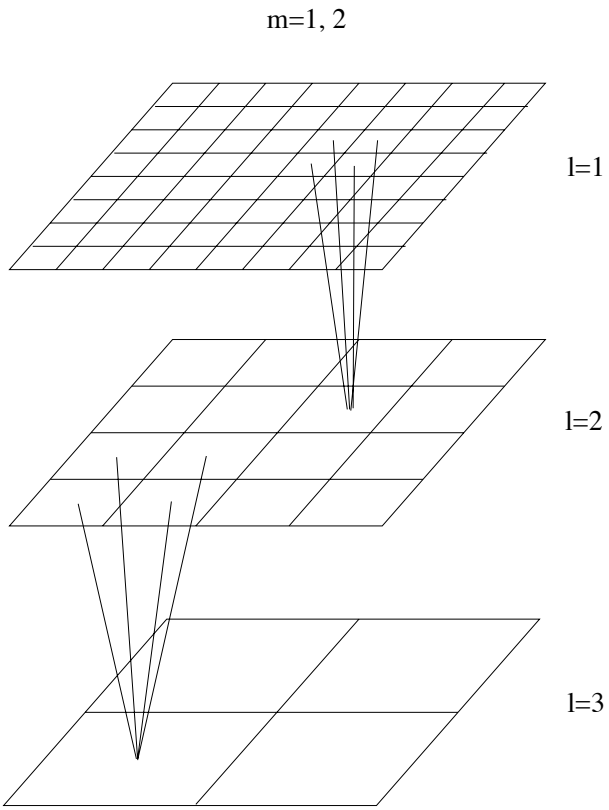

Figure 3.19: Bottom up quad-tree representation.

The quad-tree representation provides a multi-resolution analysis of the data and is computationally more efficient compared with some other techniques such as scale-space methods. The major disadvantage of this quad-tree representation is that it imposes extra constraints on the shape and position of the regions that can be processed. The regions have to be square and have to be at positions within the quad-tree 'window'. This means that a feature cannot always be analysed and represented at its ideal scale. However, after having found the multi-resolution representation of the data, a linking

algorithm is used to explore the global topology of the branching structure.

Once the quad-tree structure is set up and the parameters of each model at each scale have been estimated, the most fit model and 'natural' scale for the features is determined for a given image region by using a penalised distance measure, the Akakie information criteria (AIC). This biases the residual fit error which is expected to fall with the increasing number of parameters P.

AIC is derived from Kullback-Leibler Information which is defined as

$$K(f,g) = \int f(x) log[\frac{f(x)}{g(x|\theta)}]dx \tag{3.36}$$

where f, g are notations for full reality of truth and approximating models in terms of probability distributions respectively. $K(f,g)$ denotes the information lost when g is used to approximate f, or the distance from g to f as a heuristic interpretation [85].

The K-L information provides a distance measure between two models or probability distributions, however, both f and g must be known to calculate the distance using equation 3.36. Therefore, we normally only calculate a relative distance instead. Since equation 3.36 is equivalent to

$$\begin{aligned} K(f,g) &= \int f(x) log(f(x))dx - \int f(x) log(g(x|\theta))dx \\ &= E_f[log(f(x))] - E_f[log(g(x|\theta))] \end{aligned} \tag{3.37}$$

and the first expectation $E_f[log(f(x))]$ is a constant that depends only on the unknown, the true distribution, we are able to calculate the *relative* distance by

$$K(f,g) - C = -E_f[log(g(x|\theta))] \tag{3.38}$$

Since the constant C is the same across all candidate models, it can be ignored. Although equation 3.38 allows us to calculate the distance without knowing the true distribution of f, it remains conceptual since we don't know the true parameters θ for the model g.

Akaike [88] proposed a model selection criterion to estimate the K-L distance based on the empirical log-likelihood function at its maximum point. Since in practice, the model parameters are estimated $\hat{\theta}$, rather than the true parameters θ, we have to change our model selection criterion to that of minimizing the expected estimated K-L distance rather than minimising the known K-L distance over the set of models considered. Akaike [88], showed that the key issue for getting an applied K-L model selection criterion was to estimate $E_y E_x[log(g(x|\hat{\theta}(y)))]$ where x and y are independent random samples from the sample distribution and both statistical expectations are taken with respect to truth (f). He also found that under certain conditions, it can be estimated by the maximised $log(\mathcal{L}(\hat{\theta})|data)$ minus a bias factor which is approximately equal to the number of estimable parameters P in the approximating model. A model selection criteria, **AIC**, based on the log-likelihood

is then defined as

$$AIC = -2log(\mathcal{L}(\hat{\theta}|y) + 2P \tag{3.39}$$

In the special case of least squares estimation with normally distributed errors, AIC can be expressed as a function of residual sum of squares:

$$AIC = N^2 log(RSS/N^2) + 2P \tag{3.40}$$

where N^2 is number of data and RSS stands for the residual sum of squares $\sum \hat{\epsilon}^2$.

One of the conditions of using equation 3.40 is that the sample size is relatively large with respect to the number of estimated parameters $N^2/P > 40$. For small data sets, Hurvich and Tsai [89], reported a second-order bias adjustment which led to a criterion called AIC_c,

$$\begin{aligned} AIC_c &= -2log(\mathcal{L}(\hat{\theta})) + 2P\left(\frac{n}{P-K-1}\right) \\ &= -2log(\mathcal{L}(\hat{\theta})) + 2P + \frac{2P(P+1)}{n-P-1} \\ &= AIC + \frac{2P(P+1)}{n-P-1} \end{aligned} \tag{3.41}$$

when n is large with respect to P then the second-order correction is negligible and $AIC_c \approx AIC$. The full derivation of AIC can be found in [85].

From a heuristic point of view, equations 3.40 and 3.41 can be interpreted as a measure of lack of model fit plus a penalty term for increasing the number

of parameters, shown as a tradeoff between bias and variance. However, the penalty term in AIC is not arbitrary but derived from an asymptotic estimator of relative, expected K-L information or distance between model pairs. Minimising the AIC provides an estimated best approximating model for that particular data set.

The recursive algorithm of this multi-resolution representation can be summarized as follows:

1. Estimate the initial parameters for each model $m = 1$ at some starting block size.
2. Use equations 3.30–3.32 to improve the first estimate for each model m.
3. Compute AIC from RSS using equation 3.40 or 3.41 (which depends on the N^2/P ratio).
4. Repeat steps $(1) - (3)$ for $m + 1 \leq M$.
5. $m_{opt} = \arg_m \min(AIC)$.
6. Repeat steps $(1) - (5)$, for $l + 1$ until m_{opt} is calculated at all levels.

According to the quad-tree structure, the 'natural' scales of the features can also be determined by taking the smaller value of the AIC summations of

child blocks across scales and comparing the information number with their parents;

$$\sum_{k=0}^{3} AIC(\mathbf{c}_k) \longleftrightarrow AIC_m(\mathbf{p}) \tag{3.42}$$

where $\mathbf{c}_k$ represents four 'child' blocks $\mathbf{c_0} = (2i, 2j, l)$, $\mathbf{c_1} = (2i+1, 2j, l)$, $\mathbf{c_2} = (2i, 2j+1, l)$, $\mathbf{c_3} = (2i+1, 2j+1, l)$ and $\mathbf{p}$ is the corresponding to 'parent' block $\mathbf{p} = (i, j, l+1)$. The block(s) with the minimum AIC value is then picked to represent the data in a given region. Figure 3.20 is a flow chart that shows an overview of this multi-resolution estimation algorithm.

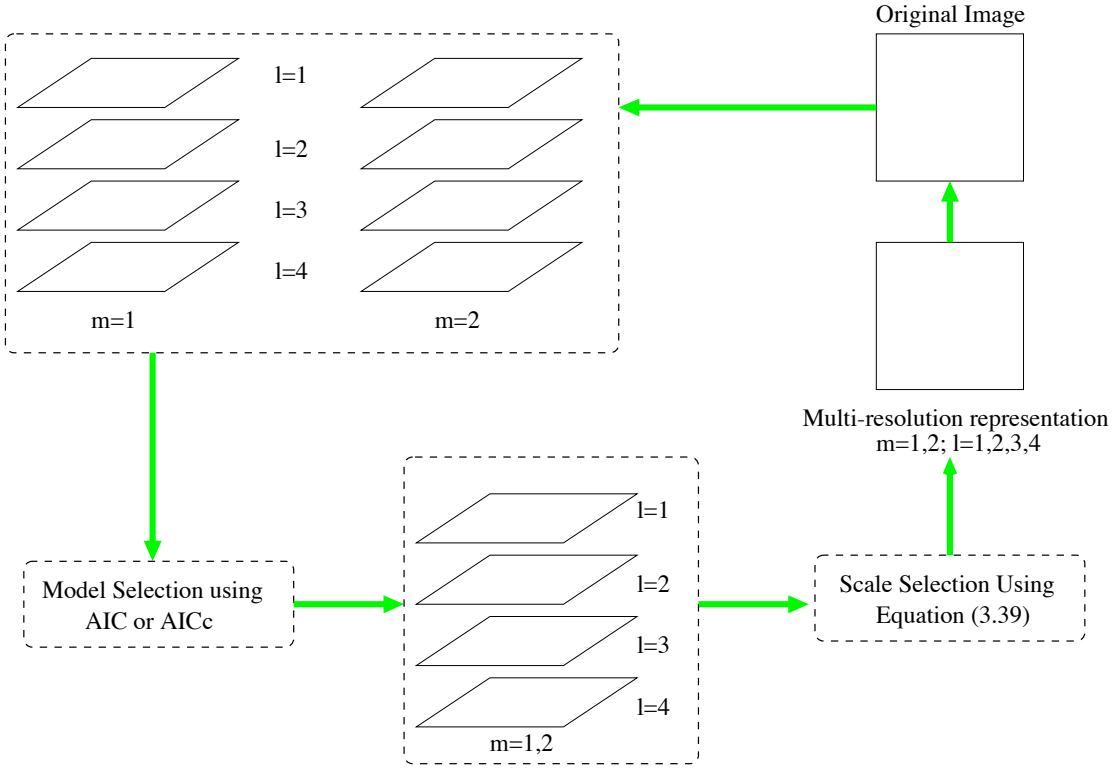

Figure 3.20: Flow chart of multi-resolution modelling and model/scale selection algorithm.

Figure 3.21 shows the model/scale selection results on a small part of a retinal image. As mentioned at the beginning of this section, there is always a tradeoff between bias and uncertainty in the feature modelling. The mean square error between reconstruction and original image against number of parameters used for the data representation are also calculated at figure 3.21 (f). As we can see from the table, using a hierarchical feature representation gains the best MSE using least number of parameters compared with single scale feature modelling.

3.5 Experiment Results

To verify the algorithm's performance, we first test the method on a noise free image. Figure 3.23 is generated by an original retina fundus image multiplied by the hand labelled image to eliminate the background noise. Figure 3.23 (b) & (c) shows the reconstruction result of blocks using single and multiple Hermite-Gaussian models respectively. Different block sizes are highlighted that indicate the region is modelled at different levels. Figure 3.24 shows the results on another image from the database. As we can see from the result, the main vasculature, small blood vessels, bifurcations and crossing points are modelled accurately using the above multi-scale Hermite-Gaussian representation. The mean square errors of the two reconstruction images are also calculated. The experiments were also carried out on the entire

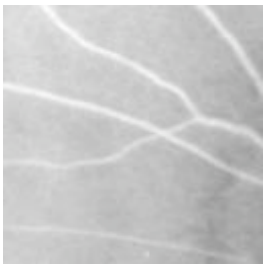

(a) Original

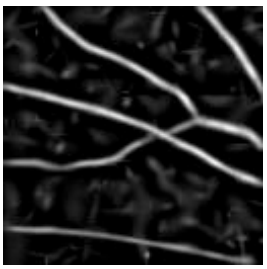

(b) Reconstruction 16x16

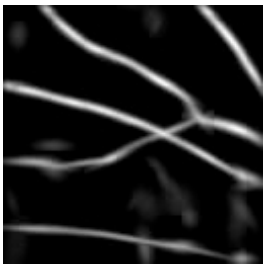

(c) Reconstruction 32x32

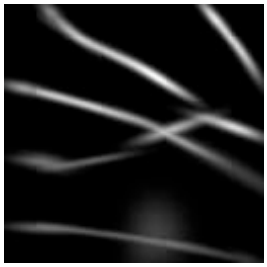

(d) Reconstruction 64x64

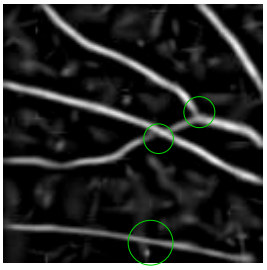

(e) Reconstruction Multi-Scale

Block Size	MSE	Number of Parameters
Multi Scale	29.8	602
64x64	59.3	133
32x32	41.2	483
16x16	23.5	1862

(f) Table of MSE vs Number of Parameters

Figure 3.21: Reconstruction result on a portion of retina image using Hermite-Gaussian modelling. (b)-(d) are the result using H-G modelling at different scale and (e) is the result after model/scale selection using AIC. Blocks using multiple model are also highlighted by a green circle. (f) Table of MSE vs Number of Parameters using single and multi scale representation.

dataset which contains both healthy retinal images and those with pathology.

Figure 3.22 shows the plot of MSE of the whole data set using Hermite-Gaussian approaches.

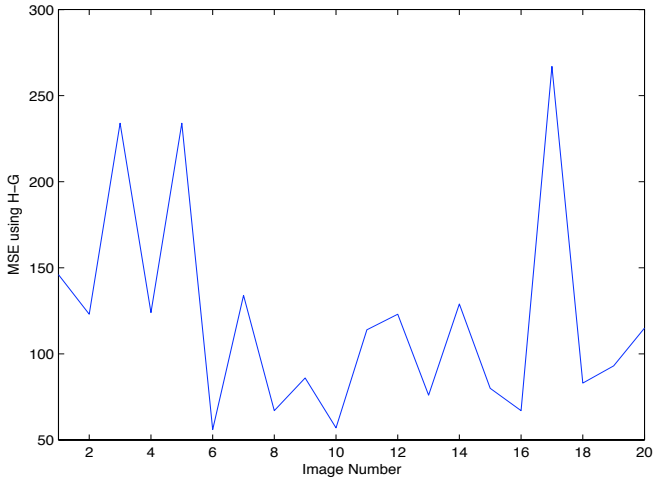

Figure 3.22: Mean Square Error of reconstruction result using H-G modelling on the whole data set.

To assess the robustness of the modelling algorithm, Gaussian additive noise is added to figures 3.23 & 3.24 (a) at 0db. The SNR is calculated as [86] [90],

$$SNR = 20log_{10}[\frac{\mu_f - \mu_b}{\sigma_n}]dB \tag{3.43}$$

where μ_f and μ_b are the gray levels of the vessel and background and σ_n is the standard deviation of the additive Gaussian white noise.

Figures 3.25, 3.26 shows the reconstruction results under the noisy data. The results illustrate the immunity of the algorithm against such noise. Figure 3.27 shows the reconstruction results on the original image. Overall, the Hermite-Gaussian modelling followed by a ML type of estimation and AIC model/scale selection scheme works well. The orientation, position and

Image (Noise Free)	MSE (G)	MSE(H-G)	Image (SNR = 1)	MSE (G)	MSE(H-G)
1	44.6	39.5	1	78.5	58.0
2	58.7	57.5	2	71.5	65.2
3	76.2	32.1	3	99.2	65.2
4	23.5	18.5	4	55.2	48.5
5	68.3	44.2	5	88.4	78.5
6	45.7	32.4	6	78.6	65.0
7	27.5	14.7	7	41.3	35.8
8	66.2	38.7	8	99.2	95.9
9	33.4	32.7	9	65.5	55.1
10	21.3	18.7	10	42.7	25.0

Table 3.1: Reconstruction error using simple gaussian modelling and Hermite-Gaussian modelling for 10 noise free and noisy images.

width of the features both along blood vessels and near bifurcations are accurately modelled on both noise free and noisy data. Table 3.1 summarises the mean square error of the reconstruction results using both approaches for 10 images with and without noise. We can see that by using the Hermite approximation on average reduce the reconstruction error by 23%.

3.6 Summary

This chapter has proposed a multi-resolution Hermite-Gaussian (H-G) modelling algorithm for tree like structural features. Firstly, the original image is divided into imaging blocks forming a quad tree pyramid representation. H-G modelling is then employed at each level, blocks with multiple features

are modelled with superposition of Gaussians. An EM type of optimisation scheme is used to obtain more accurate results on feature parameters i.e. centroid, orientation, width. After segmenting the image at each level, an information criteria (AIC) is used to select the most appropriate model and scale for a given region.

It has been shown that using the above method, we can accurately model not only the main vasculature with relatively high intensity values, but also the small vessels with very low contrast against the background.

For a complete segmentation of the image, some form of neighbourhood linking strategy still remains to be developed to extract the global vascular topology and provide the vessel/non-vessel classification. This will be discussed in length in the next chapter.

(a) Original Image

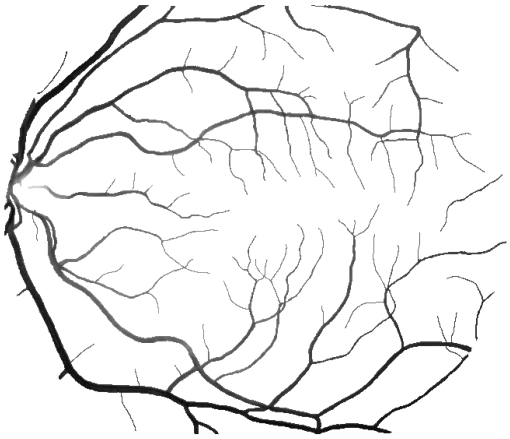

(b) Reconstruction result $m = 1$

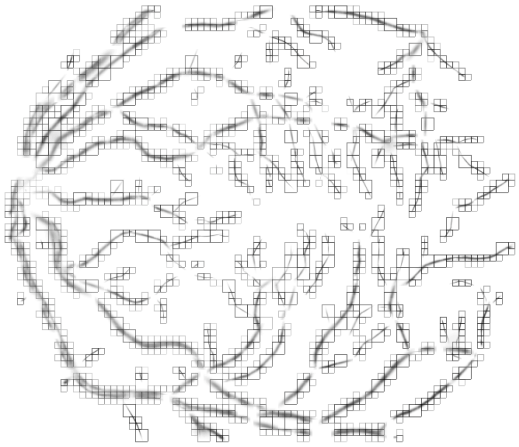

(c) Reconstruction result $m = 2$

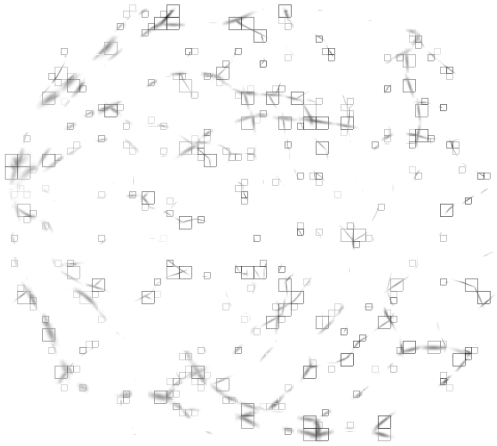

(d) Reconstruction result $m = 1, 2$

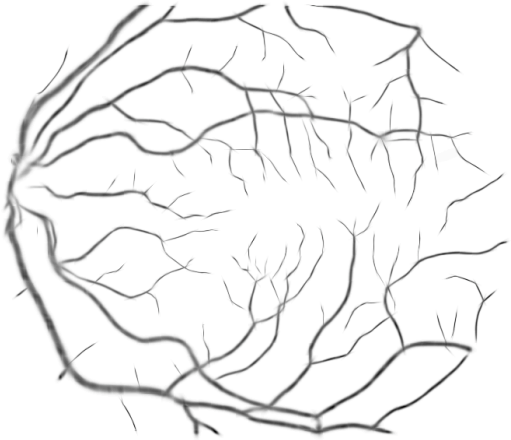

Figure 3.23: (a) Original noise free image generated by a multiplication between the original image and binary hand labelled result.(#IM0077) (b) Reconstruction results contain blocks using a single Hermite-Gaussian model $m = 1$ only. (c) Reconstruction results contain blocks using multiple Hermite-Gaussian models $m = 2$ only. (d) Combined reconstruction result $m = 1, 2$.

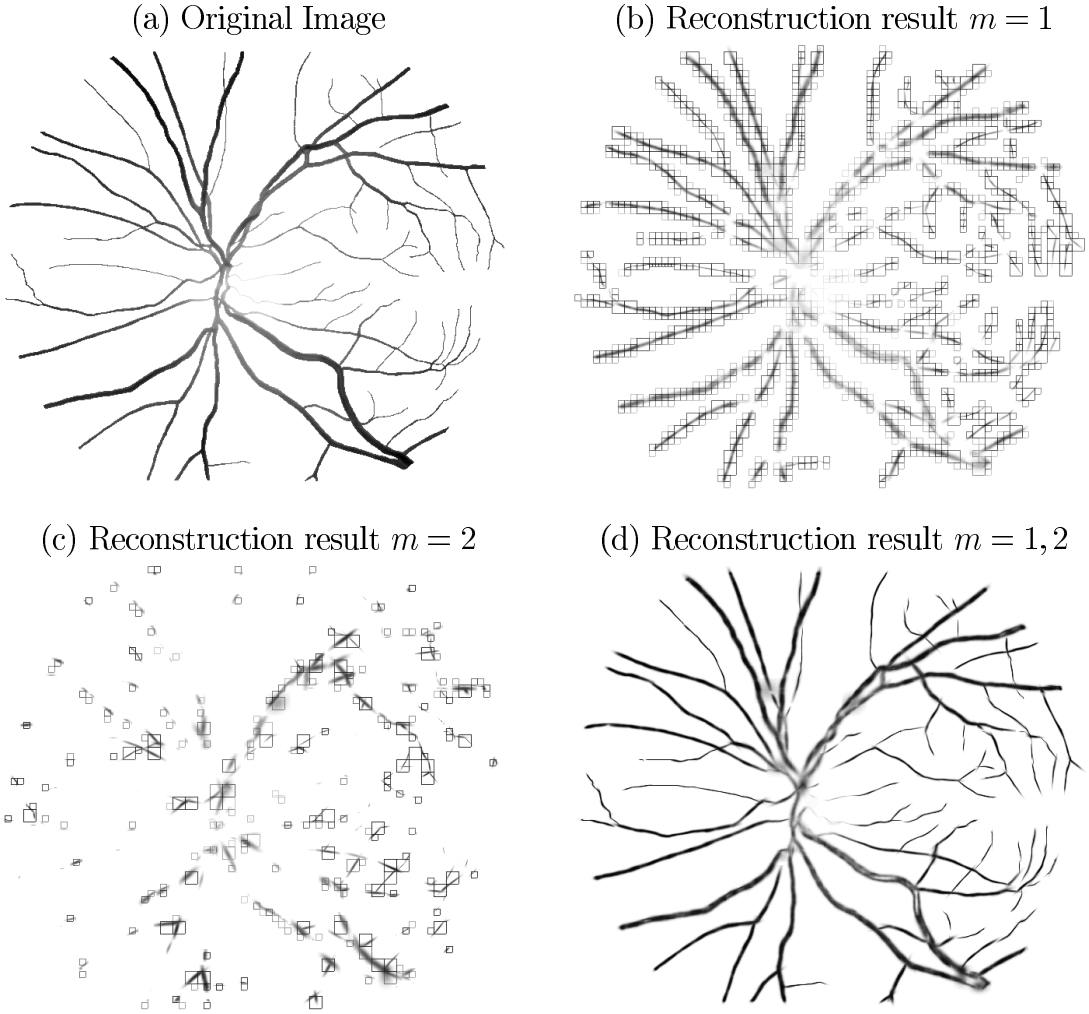

Figure 3.24: (a) Original noise free image generated by a multiplication between the original image and binary hand labelled result.(#IM0163) (b) Reconstruction results contain blocks using a single Hermite-Gaussian model $m = 1$ only. (c) Reconstruction results contain blocks using multiple Hermite-Gaussian models $m = 2$ only. (d) Combined reconstruction result $m = 1, 2$.

(a) Original Image SNR = 1

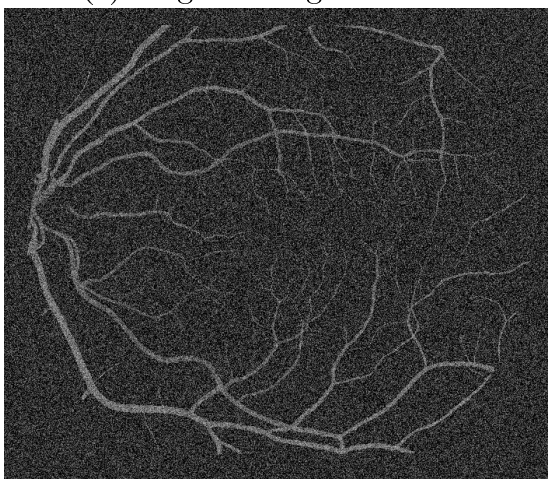

(b) Reconstruction result $m = 1$

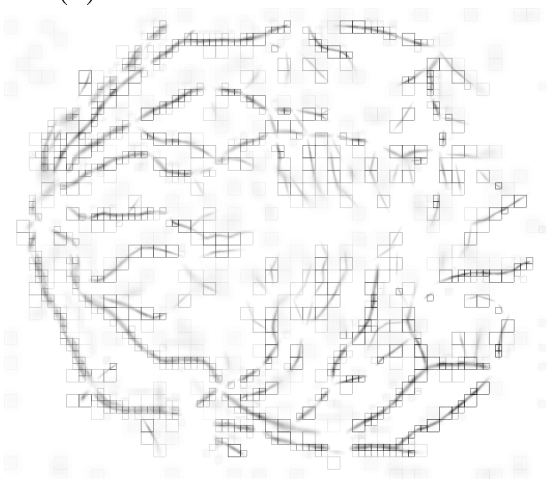

(c) Reconstruction result $m = 2$

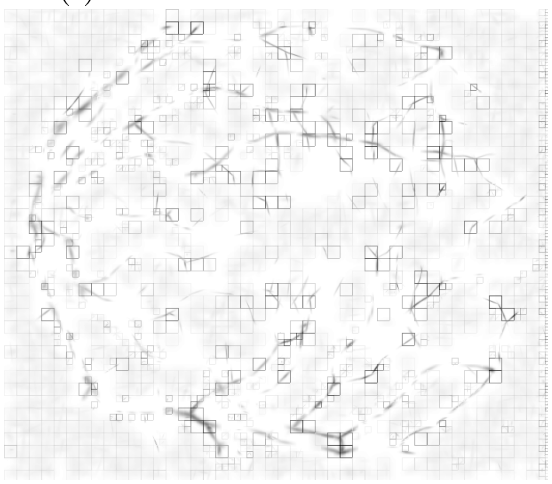

(d) Reconstruction result $m = 1, 2$

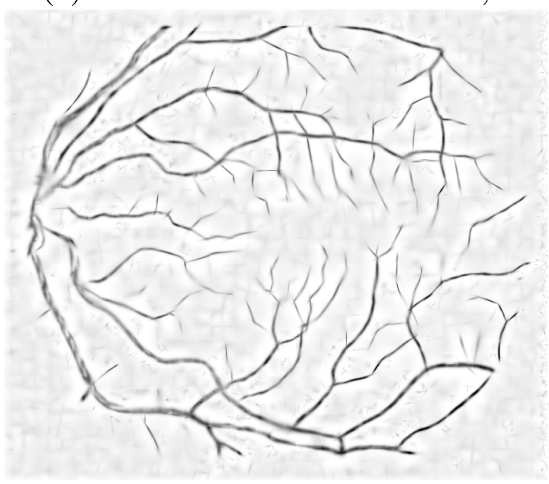

Figure 3.25: (a) Noisy Image (SNR=1) generated by adding white noises to figure 3.23(a).(#IM0077) (b) Reconstruction results contain blocks using a single Hermite-Gaussian model $m = 1$ only. (c) Reconstruction results contain blocks using multiple Hermite-Gaussian models $m = 2$ only. (d) Combined reconstruction result $m = 1, 2$.

(a) Original Image SNR = 1

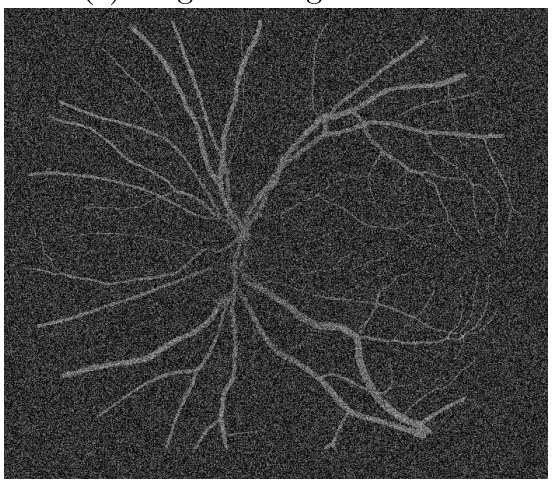

(b) Reconstruction result $m = 1$

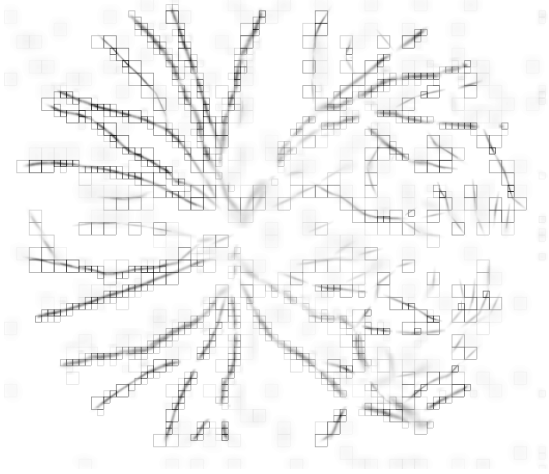

(c) Reconstruction result $m = 2$

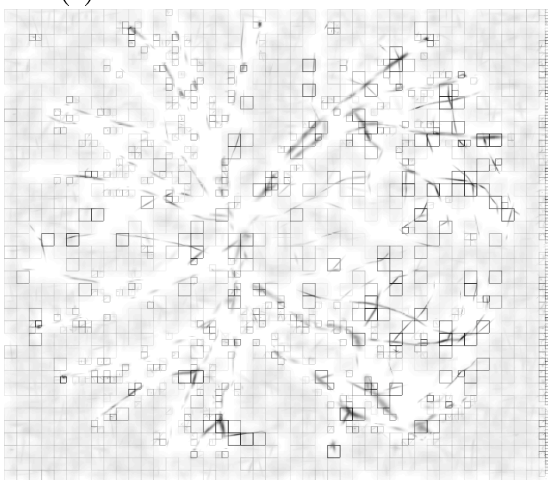

(d) Reconstruction result $m = 1, 2$

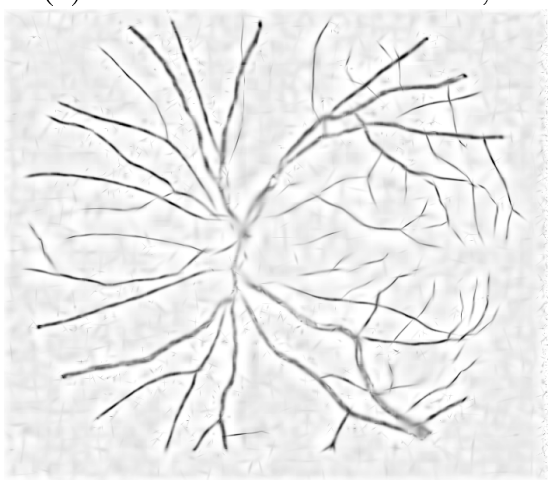

Figure 3.26: (a) Noisy image (SNR=1) generated by adding white noises to figure 3.24(a).(#IM0163) (b) Reconstruction results contain blocks using a single Hermite-Gaussian model $m = 1$ only. (c) Reconstruction results contain blocks using multiple Hermite-Gaussian models $m = 2$ only. (d) Combined reconstruction result $m = 1, 2$.

(a) Original Image

(b) Reconstruction result $m = 1, 2$

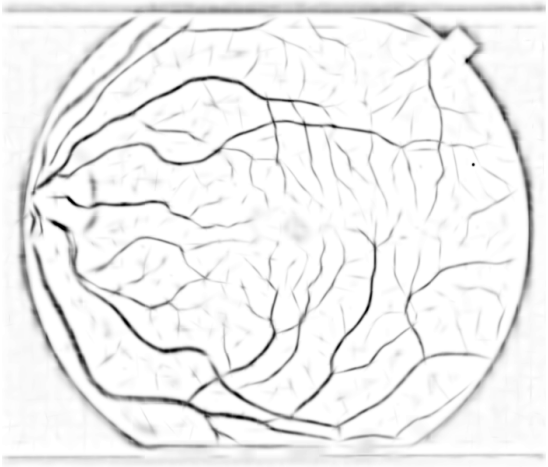

(c) Original Image

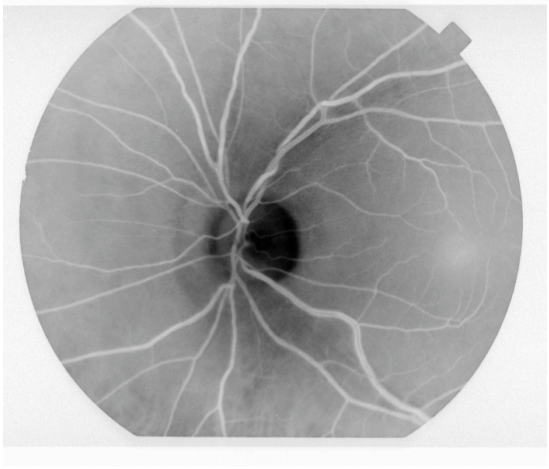

(d) Reconstruction result $m = 1, 2$

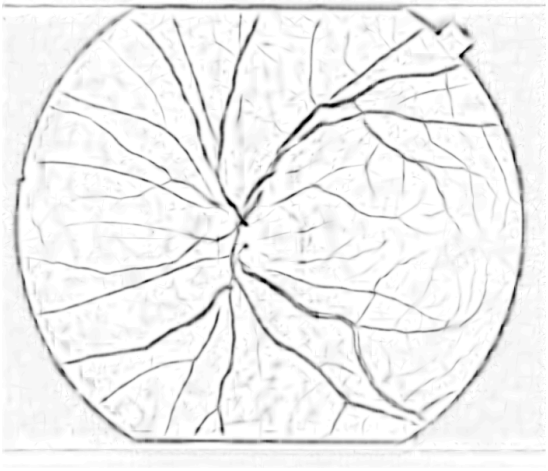

Figure 3.27: (a) & (c) Original images in the database (#IM0077 & #IM0163) (b) & (d) Reconstruction results containing blocks using single and multiple Hermite-Gaussian models $m = 1, 2$.

Chapter 4

Global Structure Inference

In the previous chapter, the emphasis was on identifying and estimating the property of local features such as diameter, orientation, and the position of vessel segments. For a complete segmentation of the image, an analysis of geometrical and topological property of the global structure are needed. The pattern of the retinal blood vessels can be regarded as a branching tree structure. The study of biological branching structures began a long time ago with some of the most studied branching structures being dendrites in the lung and the arterial system.

After a brief discussion of existing algorithms, two different approaches on branching structure inference and linking are described. The methods presented in this chapter concern the measurement and tabulation of geometrical

data, as well as connectivity information from complete retinal vessel trees extracted from the parametric representation of local features obtained from the segmentation method described in previous chapters.

4.1 State of the Art

The analysis of geometry and network properties from branching structures has been widely studied. Branching structures are common in nature, occurring from river networks, lightning discharge pathways to bronchial airways and blood vessels.

The accurate and automated analysis of vessel morphology is a valuable tool in medical imaging for many reasons. It provides a map of the retinal vessels and allows the localisation of landmark points such as bifurcations. Furthermore, it enables the measuring of global properties of vasculature such as tortuosity. Blood vessel delineation and tracking algorithms on medical images can be widely found in the literature, such as on cardiovasculars MR images [91], coronary artery trees from X-ray angiograms [92], and airway trees from CT images [93]. This section presents a brief literature review of current image analysis techniques for retinal blood vessels geometry and topology studies.

Akita and Kuga [32], proposed an algorithm that uses sub images from the

original fundus image to detect a group of vessels and also analyse network neighbourhood connectivity. After the detection of blood vessels, a skeleton method is used to extract the centre line of blood vessels, and characteristic points such as start-points, end-points and branch points are identified in local windows. Vessels segments are labelled between each pair of start-points and end-points. A relaxation method is then used to perform the final step of neighbourhood connectivity based on intensity differences and the angle between neighbouring segments. The optic disc, which appears in retinal images, was also extracted by back tracking the vessel branches and using the fact that it is the entry point of all arteries. The major drawback of this approach is that it depends heavily on the initial segmentation and skeleton results.

Another approach was proposed by Eichel *et al.* [94] in the 1980s, which is based on a sequential search that assigns belief values to each edge and path, according to a probabilistic model called the *path metric*. The value of the path metric increases when the followed path is a member of the vessel edge. However, since the algorithm tracks the edges instead of the vessels, in cases of junctions or forks, the edge is still being followed even if it does not belong to the same vessel.

Tolias and Panas [95] developed a fuzzy C-means (FCM) clustering algorithm based on the fuzzy intensity information. The fussy vessel tracking process is based on finding the membership functions of the two linguis-

tic values: *vessel* and *non vessel*. The initialisation of the algorithms is performed from a bounding circle found through the detection of the optic nerve. Candidate starting points of vessels are identified from pixels around the bounding circle using a FCM. A fuzzy vessel tracking algorithm is then applied to each candidate vessel. False candidates are rejected within two or three iterations of the tracking algorithm. Tracking terminates if any of the predefined conditions are satisfied, such as the vessel contrast is lower than a user defined threshold or the number of separate vessel regions found within a profile is greater than two. The algorithm does not utilise any edge information to locate and track vessels, and thus reduces the effects of noise in the tracking procedure.

Another well-known technique for vessel extraction is the match-filter method already mentioned in Chapter 2. After convolving with a set of matched filters that consist of twelve 16×16 1D Gaussian kernels with fixed width and different orientations, a threshold probing algorithm is used to perform vessel tracking. During each *probe*, a set of criteria is tested to determine the threshold of the probe and ultimately to decide if the area being probed is a blood vessel. At each iteration, the probe examines the region-based attributes of the pixels in the tested area and segments the pixels classified as vessels. Pixels that are not classified as vessels from probes are recycled for further probing. The algorithm is reported to be capable of managing bifurcations while gaining both low false positives and true

negatives. However, it requires intensive computation since the convolution with large kernels is used. Also, the threshold selection of the probing step may be critical.

Zhou *et al.* [43], developed an algorithm based on a matched filtering approach which uses a prior knowledge about retinal vessel properties. An adaptive iterative procedure is used that models the vessel profile using a Gaussian function. The method provides an accurate modelling of blood vessels and also utilises spatial continuity properties of the vessel segments to improve computational efficiency in regions where the vessels have less curvature. However, it requires user intervention on identifying start and end search points and the direction of the first vessel.

Labelling each tree of vessels involves three steps: analysis of network neighbourhood connectivity, tracking local vessel segments and identifying branch points and cross points. It requires both efficient computation and effective procedures, which are robust in the presence of various types of noise and distortions that often plague medical images.

In this work, two algorithms are reported for measuring the global topology of vasculature. Firstly, a heuristic linking algorithm using a graph representation is proposed. Using a modified Kruskal type of maximum-cost spanning tree algorithm, the linking process is reduced to finding the optimum path in a graph representation of the image. The deterministic linking

approach is able to successfully track and characterise much of the vessel topology. However, it is prone to becoming trapped in local maxima and unable to explore less certain, alternative explanations of the data.

The second approach discussed in this chapter, includes the prior knowledge of anatomical structure. A Markov chain is employed to sample from the posterior distribution, given the local feature estimates. The sample distribution is an approximate equilibrium of a random process configured in the space of a tree-like structure. As well as gaining information about the global structure, variation in the posterior samples indicates the uncertainties about the image interpretation.

4.2 Heuristic Linking Algorithm

If we regard vessel segments at each block as vertices and all linking possibilities among neighbouring blocks as edges, the linking process can be reduced to finding the optimum path in a graph representation.

Adjacency Graph

In this context, a *graph* consists of:

- A finite, nonempty and disjoint set of nodes/vertices V. (In our work,

these are represented by the centroid of each vessel segment.)

- A set of unordered pairs of distinct elements of V, which are lines running between the nodes. Such arcs may be directed or undirected and undirected arcs often called links or edges E.

- I, an incidence relation such that every element of E is incident with exactly two distinct elements of V and no two elements of E are incident to the same pair of elements of V.

A *graph* can normally be defined as,

$$S = (V, E, I) \tag{4.1}$$

V and E are usually called the *vertex set* and *edge set* respectively, and

$$E = \{(v_i, v_j)\} \tag{4.2}$$

where v_i and v_j are in V.

The *degree* of a vertex v, $d(v)$, is the number of edges with which it is incident. Two vertices with a common edge are defined as *adjacent*. A set of vertices which are adjacent to v are defined as *neighbours*, $N(v)$. A cost $c(v_i, v_j)$ can be associated with every arc (v_i, v_j). A sequence of vertices $v_1, v_2, ..., v_k$ with each node n_i being a successor of node n_{i-1} is called a path

from n_1 to n_k, and the cost of the path is

$$c = \sum_{i=2}^{k} c(v_{i-1}, v_i) \tag{4.3}$$

Spanning Tree (ST)

The *spanning tree* of a graph is the set of $|v|$ edges that connect all vertices of the graph. In general, it is possible to construct multiple spanning trees for a graph S. If a cost, c_{ij}, is associated with each edge, $e_{ij} = (v_i, v_j)$ then the minimum/maximum weighted spanning tree (MST) is the set of edges, E_{span}, forming a spanning tree, such that:

$$C = \sum_{ij} (c_{ij}|e_{ij}) \tag{4.4}$$

is a minimum [96]. In conclusion, the requirements to construct a minimal spanning tree include:

- all the points are connected together.
- the total cost of the links used is a minimum.
- the tree is connected with no cycles.

To use the above theorem, the image data are modelled as a tree-like structure and each node of the tree is associated with a Gaussian kernel

G. Adjacent blocks are linked to form a region adjacency graph where each vertex is a feature from the scale selection.

Figure 4.1 shows a typical neighbourhood for a block in the region tessellation. The degree of each node will be at least 8 for all blocks except those that lie at the edges. For example, the centre block in figure 4.1 has 8 neighbours whereas the blocks on the edge have less. Nodes from higher levels of scale will have a greater degree than the nodes from a smaller scale.

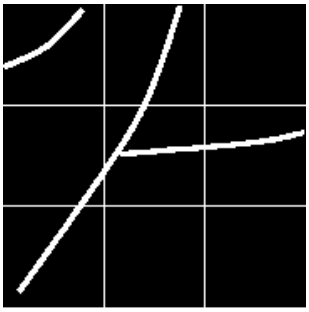

Figure 4.1: Region adjacency neighbours

As shown in Figure 4.2, part of the retina image (figure 4.2 (a)) is modelled using the methodology discussed in the last chapter (figure 4.2 (b)). A graph structure can be obtained by marking each centroid of the vessel segments as vertices and the route among neighbouring vertices as links/edges (figure 4.2 (c) & (d)).

The cost of arcs between each adjacent blocks are calculated using the *Gaussian Product Theorem*. The theorem states that the product of two

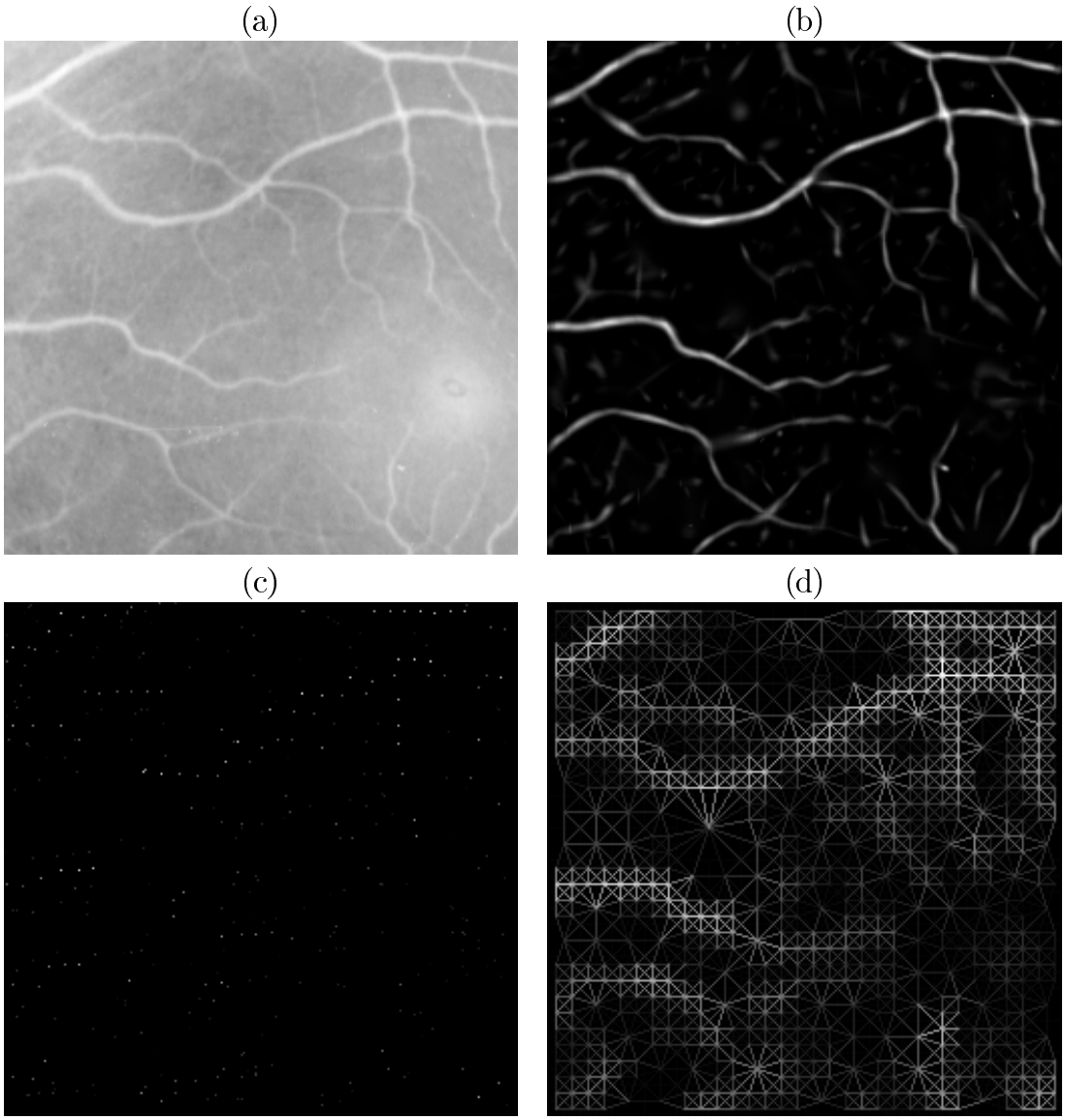

Figure 4.2: (a) Part of retinal fundus image. (b) Reconstruction result after the modelling step. (c) Vertices/node of the graph structure. (d) Arcs/edges of the graph structure. (Intensity information of the nodes and edges are reflected by the brightness.)

arbitrary angular momentum Gaussian functions on different centres can be written as a form of third Gaussian $G_1 \cdot G_2 = G_3$. (The proof can be found in Appendix B). Using this theory, the probability that two adjacent blocks i and j are part of the same vessel is estimated by calculating a link weight W_{ij} in an n-neighbour system by integrating the product of the two Gaussian feature models along a line $\mathbf{y}(t) = \mu_\mathbf{i} + (\mu_\mathbf{j} - \mu_\mathbf{i})t,\ 0 \leq t \leq 1$, joining their centroids. The number of neighbours n vary according to the block sizes.

$$W_{ij} = e^{-(A_i - A_j)^2/(2\sigma_A^2)} \int_0^1 G_{\{\mathbf{A_i}, \mu_\mathbf{i}, \mathbf{y}(t)\}} \cdot G_{\{\mathbf{A_j}, \mu_\mathbf{j}, \mathbf{y}(t)\}} dt \tag{4.5}$$

where $e^{-(A_i - A_j)^2/(2\sigma_A^2)}$ is a coefficient which is formed by a normal distribution of the difference of the amplitude and models the likelihood of changes in amplitude between features. σ_A^2 is estimated from the data.

As we can see from a synthetic branching structure (figure 4.3), the cost of edges W_{ij} is bigger when they join with relatively low curvature compared (block 2, 4, 6, 7) with the neighbouring Gaussian kernels which are disjointed or have high curvature (block 1, 3, 8, 9). Note that the intensity information is also included in the calculation, i.e. the edges are more likely to be joined when they have similar intensity values.

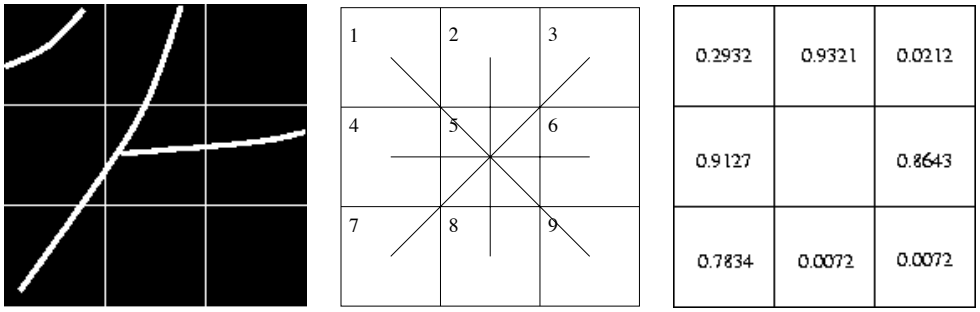

Figure 4.3: (a) Simple Branch Structure. (b) Graph paths for middle block. (c) Cost of each edge between neighbours.

Modified Kruskal Adjacency Graph

The standard graph-theoretic adjacency matrix for a graph has elements that indicate whether the corresponding vertices are connected. In the absence of loops and multiple edges: if the linking state $A_{ij} = 0$ then V_i and V_j are not connected, if $A_{ij} = 1$ then V_i and V_j are connected. Using function (4.5), the nodes can then be connected using a modified Kruskal (mKruskal) method for finding a MST of a weighted graph, W_{ij}, as the cost along the arcs [97]. The algorithm creates a forest of trees. Initially the forest consists of n single node trees and no edges. At each step, each entry to the graph indicates the smallest vertex number to which vertices are connected; eg, if $K[j] = [i]$, then $i \leq j$ and i is the vertex of smallest numeric label to which vertex V_j is connected. Edges are progressively added to the graph. At each step, we add the edge with the highest cost (W_{max}) without creating circuits. From a mathematical point of view, it can be stated as: *Let S be a weighted graph*

and let $E' \subset E$. If E' is contained in a MST T and e is the smallest edge in $E - E'$ which does not create a cycle, $E' \cup e \subseteq T$.

Based on the biological nature of the data, we further constrain the resulting tree to be binary in this application, i.e vertices can have degree 3 or less. The algorithm proceeds as follows:

1. Pre-sort the edge costs, E, into descending order of weight.
2. Examine each edge and add to the tree T if it satisfies:
   (a) It connects two vertices from different components.
   (b) The degree of vertices at each end is currently less than 3.
3. Terminate when the weight of the current edge is lower than some user defined threshold.

Figure 4.4 shows the result on a small portion of a retinal fundus image. Different colours are used to show the ability of the algorithm to successfully track and characterise much of the vessel topology.

4.2.1 Experiments and Discussion

We have presented a neighbourhood linking algorithm using a modified Kruskal algorithm. The Hermite-Gaussian representation of the image is first converted into a *Spanning Tree* graph structure and the local conductivities are

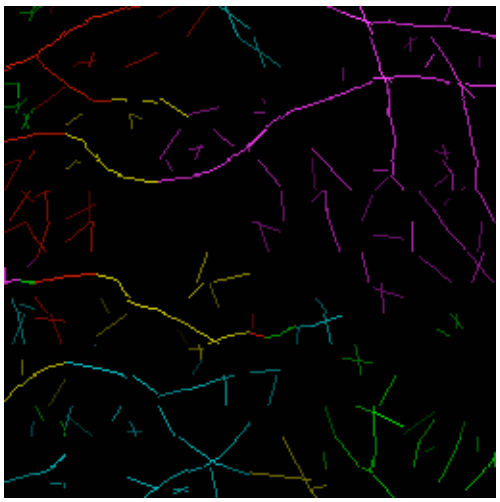

Figure 4.4: Chosen paths with highest weighting factor. Different colours reflect the linkage between features from different blocks.

then identified by finding the highest weighted arcs/edges among the neighbours and a MST is constructed.

The experimental results presented in this section illustrate the operation of the heuristic linking process using a modified Kruskal MST algorithm. Two noise free retina images of figures 4.5 (a) & (c) are first used to test the algorithm. The results after the linking process are shown on the right hand side of figure 4.5, different colours indicate the separate tree structures. To test the robustness of the method, noise was added to the *clean* image at $SNR = 1$ and original noisy images (See figures 4.6 and 4.7).

The results demonstrate the ability of the greedy algorithm to successfully track and characterise much of the vessel topology, however, the linking result degrades as the uncertainty of the data increases, as we can see from

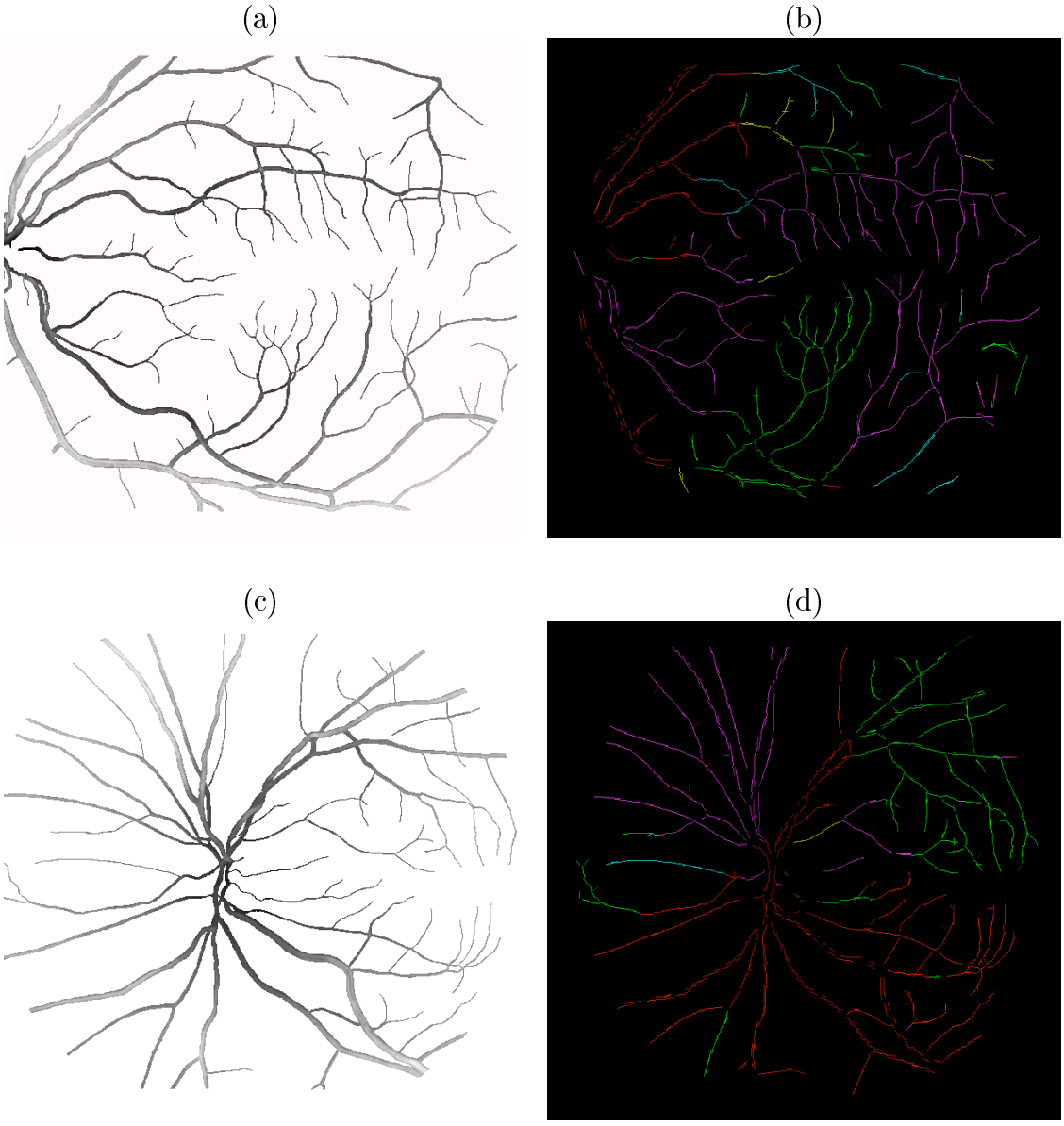

Figure 4.5: (a) & (c) Noise free retina image. (b) & (d) The linking result using the Kruscal minimum spanning tree algorithm.

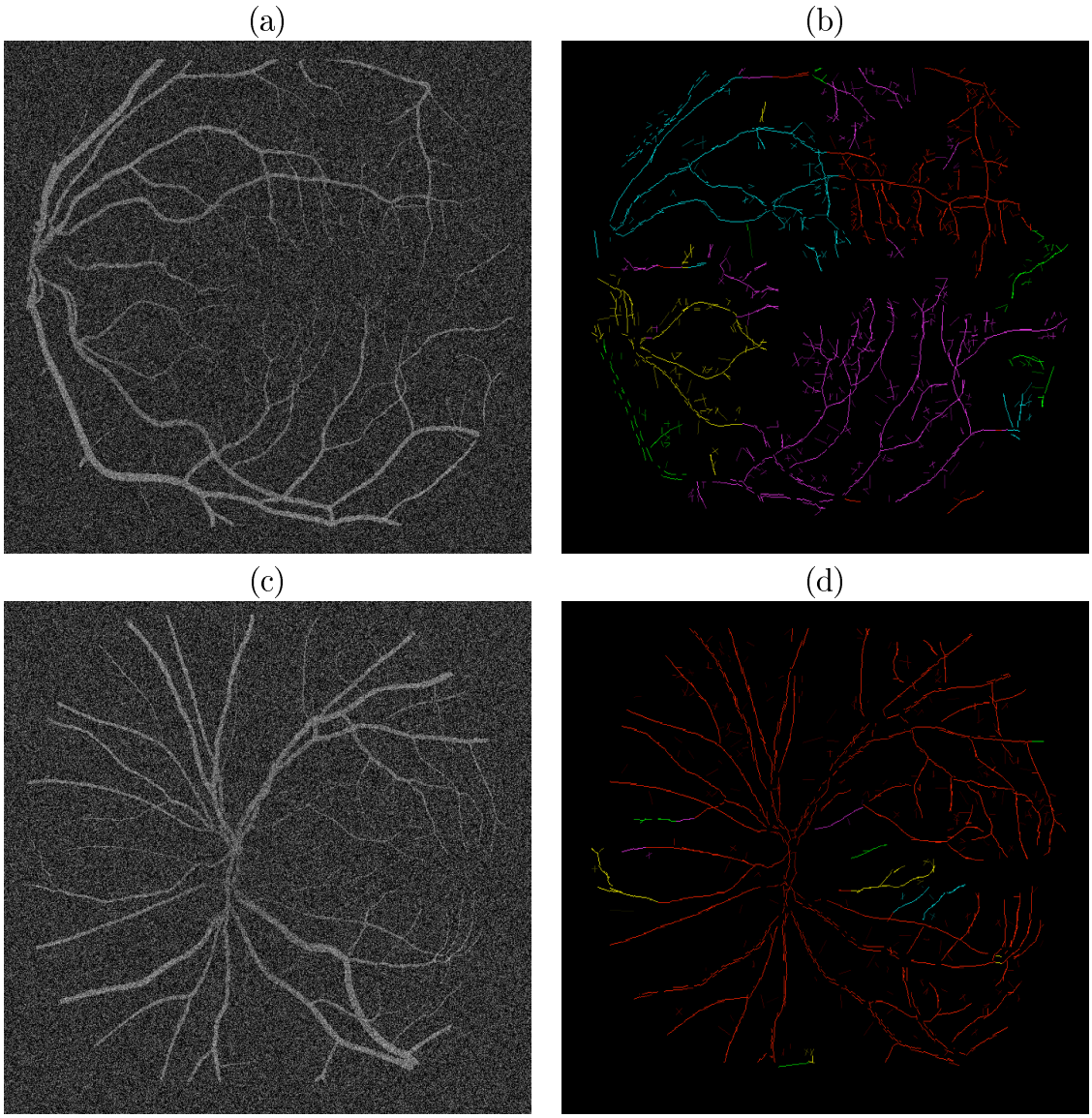

Figure 4.6: (a) & (c) Noise retina image (SNR=1). (b) & (d) The linking result using the Kruscal minimum spanning tree algorithm.

figures 4.5 to 4.7. To overcome this drawback, *prior* knowledge can be incorporated into the simulation and locally uncertain solutions in the data can

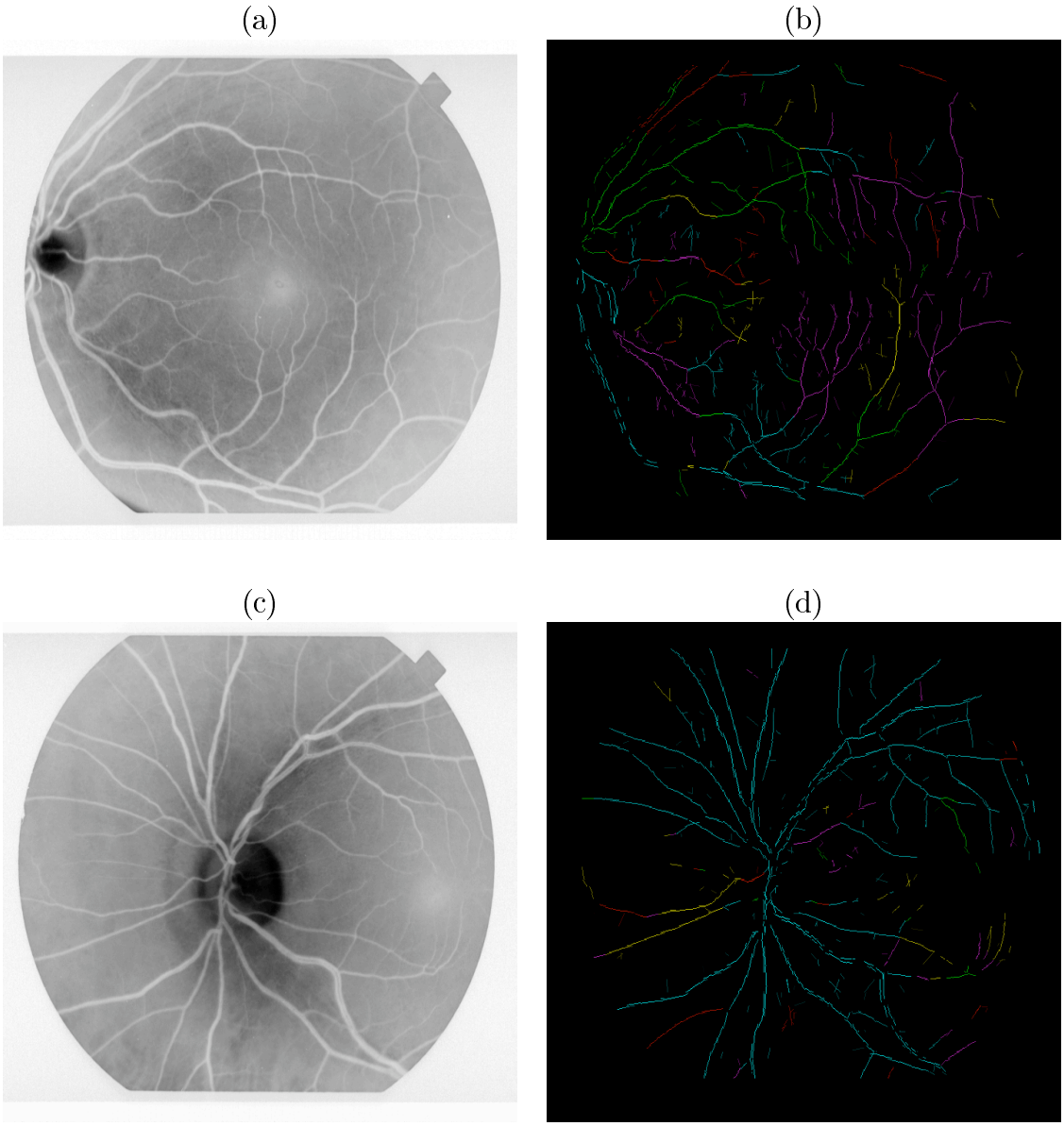

Figure 4.7: (a) & (c) Original image in the database (#IM0077 & #IM0163) (b) & (d) The linking result using the Kruscal minimum spanning tree algorithm.

be explored, which leads to a Markov chain type of algorithm.

4.3 Stochastic Linking Algorithm

As shown in the previous section, the Kruskal deterministic algorithm can produce a fast and reliable neighbourhood linking result in low noise images. However, since the heuristic linking algorithm is a greedy operation, at no stage does it try to look ahead more than one edge and is prone to becoming trapped in a local maximum. A Bayesian, stochastic type of approach can be used instead of the deterministic algorithm to explore less certain, alternative explanations of the data.

Common statistical methods for such medical image analysis tasks have typically used likelihood techniques such as Expectation Maximisation [98] [99]. Although EM methods can be computationally efficient, they provide only a limited way of incorporating *prior* information [100] [101]. General Bayesian methods such as maximum a *posterior* (MAP) can be used to include further *prior* knowledge.

4.3.1 Bayesian Approach

This section summaries the theory of Bayesian approaches and introduces terminology used throughout the section. Firstly, all variables are assumed to have a finite number of possible values. The *probability density* of variable X is denoted as $p(X)$, whereas $p(X|Y)$ is defined as the *conditional probability density* function of X given Y.

In a general Bayesian framework, if we assume $Y = Y(i,j); (i,j) \in S$ is the observed image and $X = X(i,j); (i,j) \in S$ is the true image, where S is a set of Gaussian representations, we will have;

1. $f(Y|X)$, the observed image distribution given the true image (the likelihood)
2. $\pi(X)$, a priori 'true' image distribution (the prior).

In order to explore the true image linking distribution we look for $max\, f(X|Y)$, and according to Bayes' rule,

$$f(X|Y) = \frac{f(Y|X)\pi(X)}{f(Y)} \tag{4.6}$$

A maximum of the *posteriori* probability can then be derived given the observed image i.e.

$$\hat{X} = argmax\{f(Y|X)\pi(X)\} \tag{4.7}$$

However, due to the complexity of the statistical distributions, parameters generally can not be obtained analytically from function 4.7. Some approximate methods, often based on sampling by simulation, searching or conditioning are often used in complex systems that have many variables [102].

A popular solution for approximated inference is offered by Monte Carlo Markov Chain methods [103] [104] (MCMC), that include Metropolis-Hasting algorithms. The data are modelled as a random tree-like structure and the sampling distribution is an approximate equilibrium of a random process whose configuration space is the space of the structures whose equilibrium is designed to be the target conditional distribution [105].

4.3.2 Linking Probabilities

The probability of the link state given the data in the neighbourhood can be written as the probability of the link state given the parameters of an edge between a neighbouring block

$$P(l(\zeta,\xi)|f(\mathbf{\Theta})) \tag{4.8}$$

Using Bayes's law of conditional probability equation 4.8 can be rewritten as;

$$\begin{aligned} P(l(\zeta,\xi)|f(\boldsymbol{\Theta})) &= \frac{P(l(\zeta,\xi))P(f(\boldsymbol{\Theta})|l(\zeta,\xi))}{P(f(\boldsymbol{\Theta}))} \\ &\propto P(l(\zeta,\xi))P(f(\boldsymbol{\Theta})|l(\zeta,\xi)) \end{aligned} \tag{4.9}$$

where $P(l(\zeta,\xi))$ is a predefined prior distribution which, in the simplest case, works by setting $P(l()=1)=2/N$ for blocks represented by a single Hermite-Gaussian model and $P(l()=1)=3/N$ for multiple H-G models, where N is the number of neighbouring blocks. The sample distribution $P(f(\boldsymbol{\Theta})|l(\zeta,\xi))$ can be defined by;

$$P(f(\boldsymbol{\Theta})|l(\zeta,\xi)) = \phi(\gamma_\nu|\gamma_\eta, \eta \in \mathcal{A}(\nu)) \times \mathcal{L}(l,f) \tag{4.10}$$

in which $\phi(\gamma_\nu|\gamma_\eta)$ is the distribution of the parameters of the vertex, γ_ν [106]. It forms a first order auto-regressive process $AR(1)$. That is, the location of the root vertices γ_η are selected by choosing the centroid of the Hermite-Gaussian model which has biggest width w_{max} among the sampling windows. The location of the children $\phi(\gamma_\nu)$ are selected by a directional Gaussian distribution centred at the root. The *AR(1)* process is there to ensure the tree models do not get tangled in a small area and to govern the branch linking/growing process. By transforming the original image pixels into a parametric H-G representation, the likelihood function $\mathcal{L}(.,f)$ can be esti-

mated by integrating the product of the two Gaussian feature models along a line $\mathbf{y}(t) = \mu_\mathbf{i} + (\mu_\mathbf{j} - \mu_\mathbf{i})t,\ 0 \leq t \leq 1$, joining their centroids.

$$\mathcal{L}_{ij}(l() = 1, f) = e^{-(A_i - A_j)^2/(2\sigma_A^2)} \int_0^1 G_i \cdot G_j dt \tag{4.11}$$

$$\mathcal{L}_{ij}(l() = 0, f) = (1 - e^{-(A_i - A_j)^2/(2\sigma_A^2)}) \int_0^1 (1 - G_i) \cdot (1 - G_j) dt \tag{4.12}$$

where $e^{-(A_i - A_j)^2/(2\sigma_A^2)}$ is a coefficient which is formed by a normal distribution of the difference of the amplitudes, and models the likelihood of changes in amplitude between features (σ_A^2 is estimated from the data).

4.3.3 Metropolis-Hasting Algorithm

In order to arrive at a maximum *posteriori* (MAP) estimate from a given image, it is necessary to sample from the *p.d.f.* A Metropolis algorithm is used to generate a sequence of selections from the distributions as follows [103]:

1. Start with any initial value θ_0 satisfying $p(x) > 0$

2. Using current θ value, sample a *candidate point* θ^* from some jumping distribution $q(\theta_1, \theta_2)$, which is the probability of returning a value of θ_2 given a previous value of θ_1. The distribution is also referred to as the proposal or candidate-generating distribution. The only restriction on the jump density in the Metropolis algorithm is that it is symmetric,

i.e. $q(\theta_1, \theta_2) = q(\theta_2, \theta_1)$.

3. Given the candidate point θ^*, calculate the ratio of the density at the candidate (θ^*) and current (θ_{t-1}) points,

$$r = \frac{p(\theta^*)}{p(\theta_{t-1})} \tag{4.13}$$

4. If the jump increases the density ($r > 1$), accept the candidate point (set $\theta_t = \theta^*$) and return to step 2. If the jump decreases the density ($r < 1$), then with probability r accept the candidate, else reject it and return to step 2.

The Metropolis sampling can be summarised as

$$r = min\left(\frac{f(\theta^*)}{f(\theta_{t-1})}, 1\right) \tag{4.14}$$

The proposing move will be accepted with probability r. The equation 4.14 leads to the generation of a Markov chain as the transition probabilities from θ_t to θ_{t+1} depend only on θ_t and not any previous stages $(\theta_0, ..., \theta_{t-1})$. To eliminate the symmetric requirement of the Metropolis test, i.e. $q(\theta_1, \theta_2) = q(\theta_2, \theta_1)$. Hastings generalised the Metropolis algorithm by using an arbitrary transition probability function $q(\theta_1, \theta_2) = Pr(\theta > \theta_2)$, and the testing

equation defined as

$$r = min\big(\frac{f(\theta^*)q(\theta^*, \theta_{t-1})}{f(\theta_{t-1})q(\theta_{t-1}, \theta^*)}, 1\big) \tag{4.15}$$

An iterative simulation is then designed based on the above formulae (4.9-4.12), in order to maximise a posteriori probability. At each iteration, the Metropolis-Hastings test [107] is used to determine whether to accept or reject the linking between the visiting nodes and each of their neighbours using equation 4.15;

1. Calculate the proposed posteriori density $Pr(\theta^*|f)$ at time t.

2. Calculate the ratio of the densities

$$r = \frac{Pr(\theta^*|f)}{Pr(\theta^{t-1}|f)} \tag{4.16}$$

3. Set

$$\theta^t = \begin{cases} \theta^* & \text{with probability min}(r, 1) \\ \theta^{t-1} & \text{otherwise.} \end{cases} \tag{4.17}$$

This is effectively a simplified form of a Monte Carlo simulation using just *one* move at each iteration. As a result of this, the simulation rapidly converges to a MAP estimate. Figure 4.8 shows the simulation converging to its stationary distribution as the iteration increases.

(a) The posterior value of the first million iterations shows that the distribution converges when the iteration increases (#IM0077)

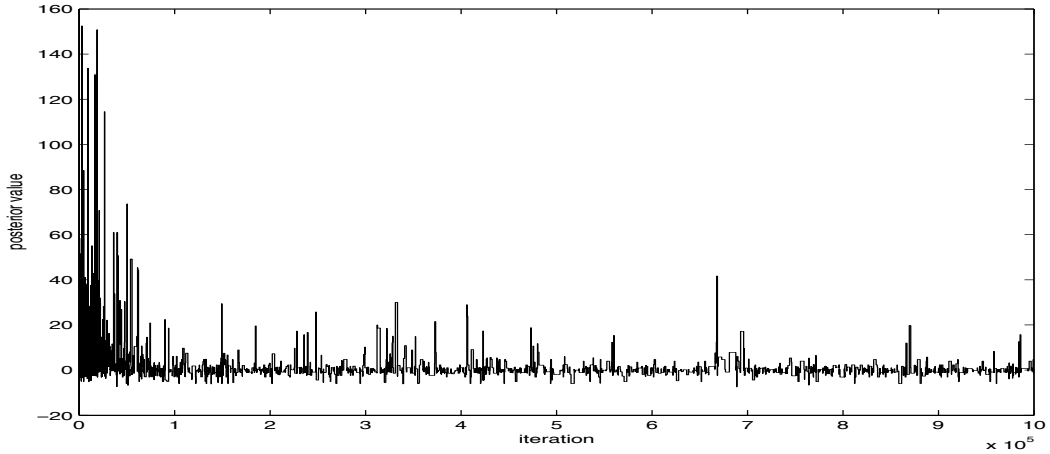

(b) The posterior value of the first million iterations shows that the distribution converges when the iteration increases (#IM0163)

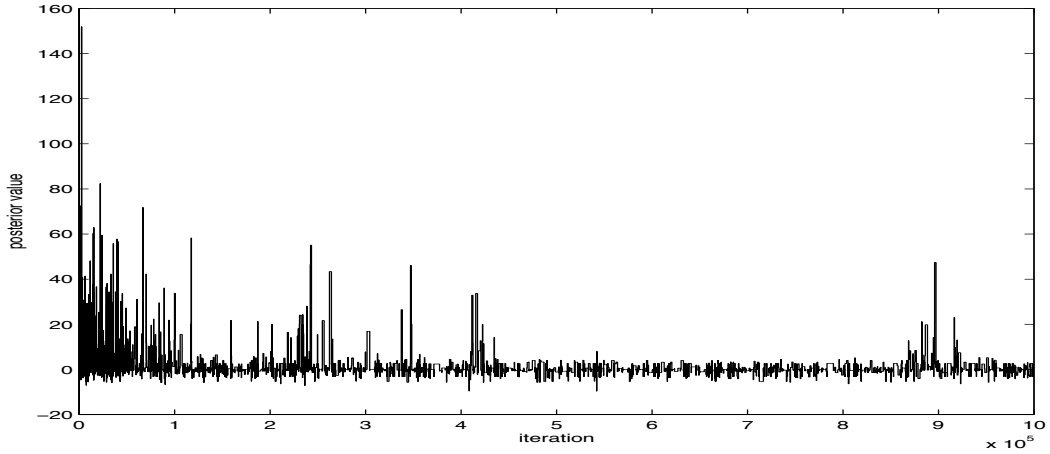

Figure 4.8: Plot of posterior distribution shows the simulation converge to its stationary distribution as the iterations increase.

Some other simple moves like alternating the vertices or adding and deleting the branch can be added to the simulation to better explore the state space of solutions. The detail of these proposals are mentioned in the last chapter.

4.3.4 Experiments and Discussion

The results presented in this section illustrate the performance of the stochastic linking algorithm.

The first experiment was carried out on a set of images with different signal to noise ratios *(SNR)*. Figures 4.9– 4.11 show the performance of the stochastic linking algorithm on a noise free image, an image with 0dB white noise and the image with original background. As we can see from the result, the simulation is able to explore the majority of the vessel structures despite the increase in noise.

The results shown above illustrate the ability of a Markov Chain type of stochastic linking strategy on exploring the vessel topology on the data with high uncertainty. The algorithm needs approximately 10 million iterations to converge to its equilibrium distribution which takes 75 mins to process the example data (#IM0077) on a Sun Ultra-10 machine. The results demonstrate the robustness of the method when the uncertainty of the data increases compared with the deterministic algorithm. Since the random sampling is restricted to 1 move, the convergence of the simulation is faster than a full MCMC algorithm. However, it requires a good estimation of the parameters of the modelling, including orientation, centroid and width of any blood vessel segments.

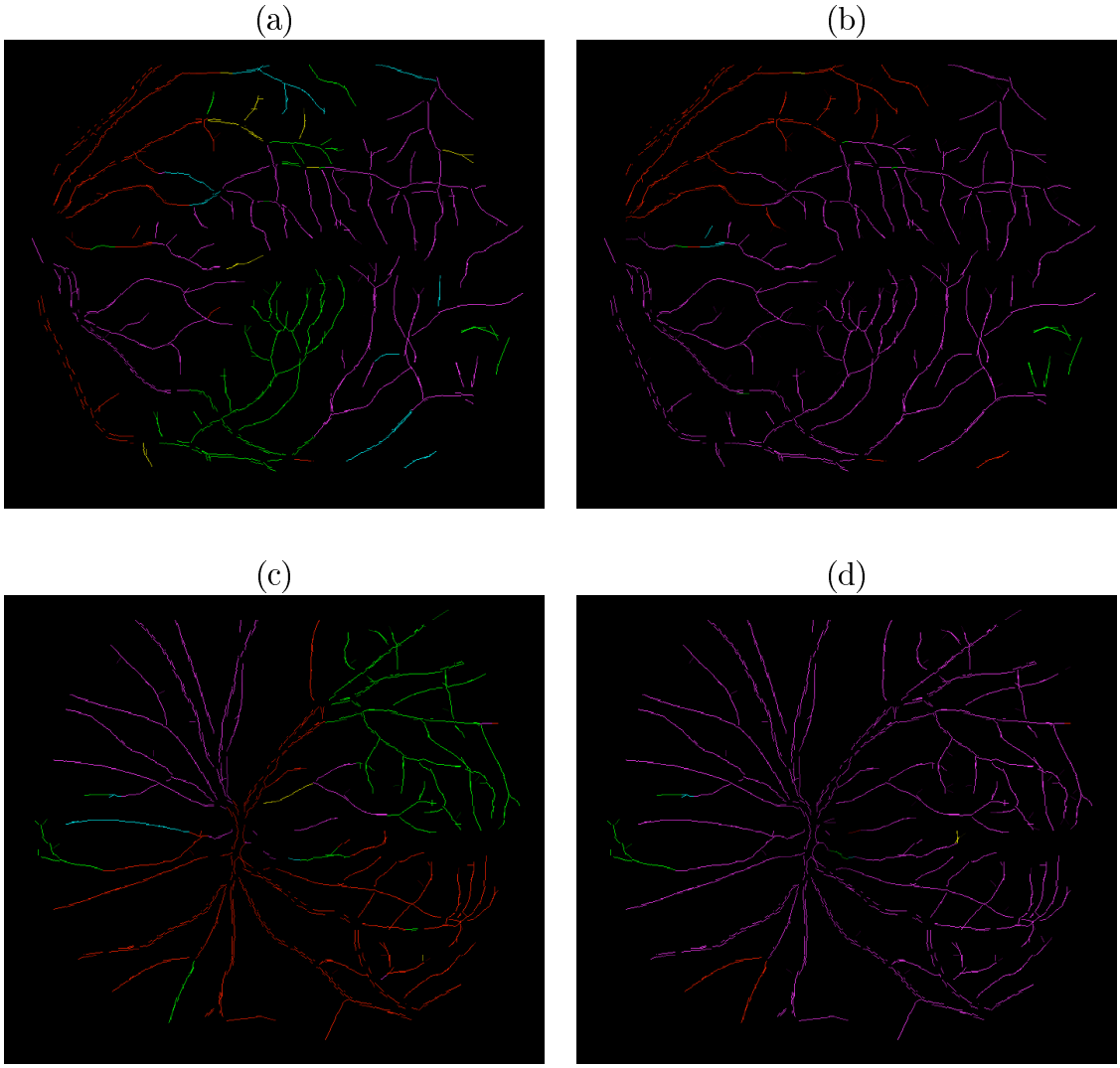

Figure 4.9: (a) & (c) Linking result using Kruskal minimum spanning tree algorithm, (Noise free). (b) & (d), The linking result using Markov chain stochastic algorithm, (Noise free).

4.4 Summary

This chapter has proposed two types of linking algorithms. Each block from the multi-resolution Hermite-Gaussian model is treated as a vertex and the

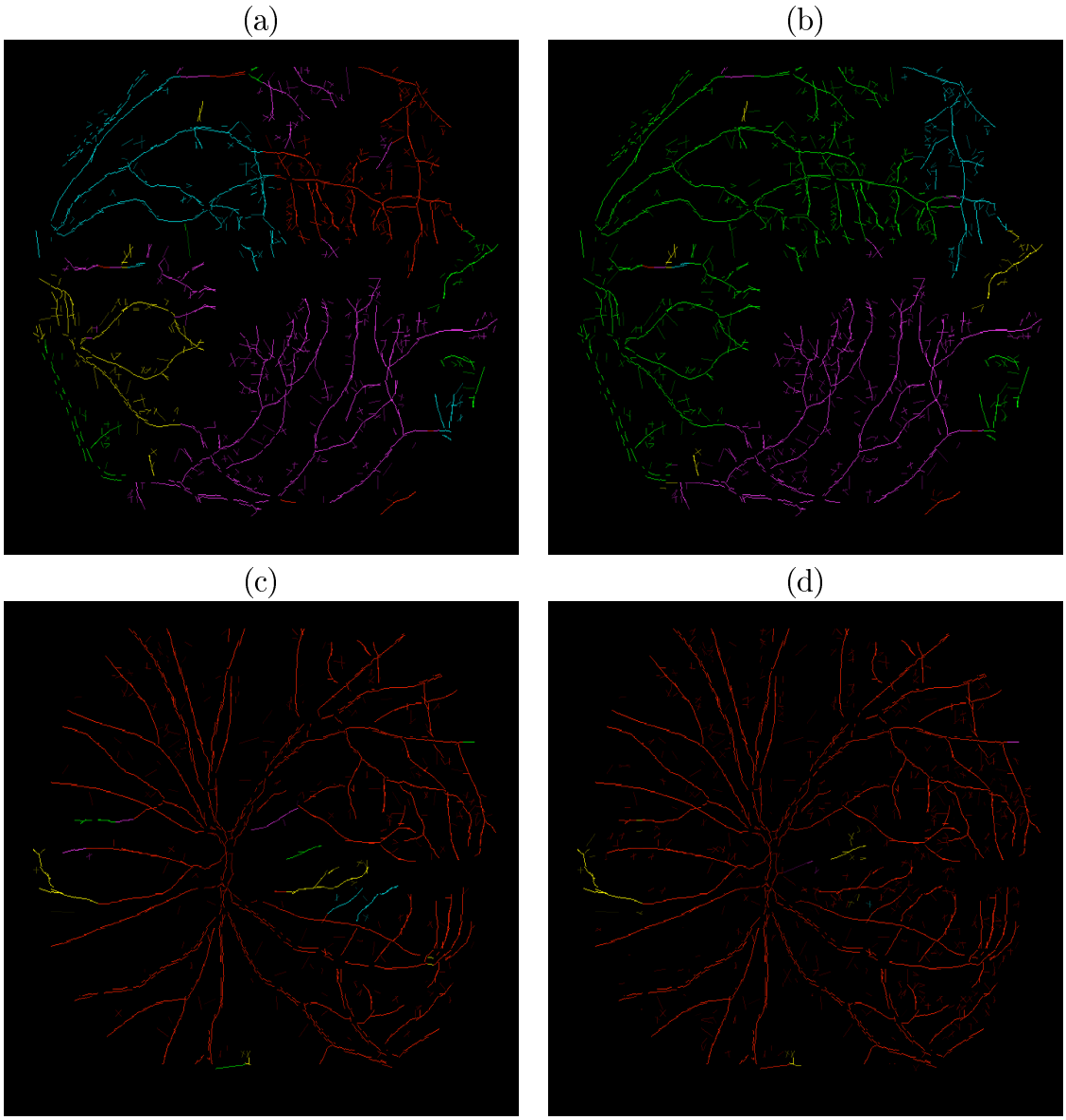

Figure 4.10: (a) & (c) Linking result using Kruskal minimum spanning tree algorithm, (SNR=1). (b) & (d), The linking result using Markov chain stochastic algorithm, (SNR=1).

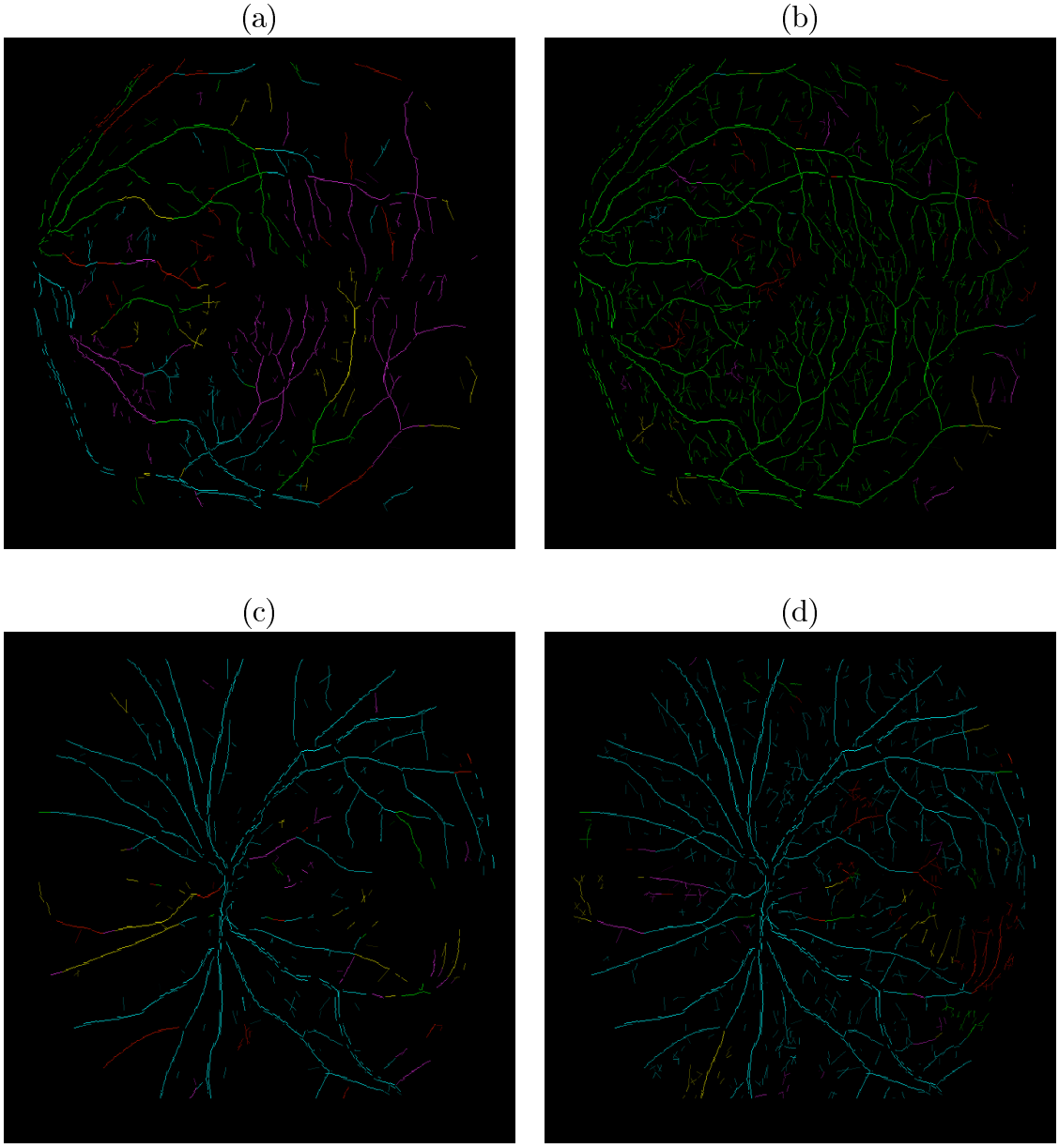

Figure 4.11: (a) & (c) Linking result using Kruskal minimum spanning tree algorithm, (Original sample image). (b) & (d), The linking result using Markov chain stochastic algorithm, (Original sample image).

links between them are regarded as edges. In the deterministic algorithm, the weight between each neighbouring block is calculated based on the Gaussian integration theorem and a modified Kruskal maximum spanning tree is then used to explore the optimised path of the graph structure. The estimator can explicitly model bifurcations and is computationally efficient. For example, the processing time of the data (#IM0077) is 2 minutes on a SUN Ultra-10 machine. However, due to the nature of greedy algorithms, it is prone to becoming trapped in local maxima and unable to explore less certain, alternative explanations of the data.

The second method proposed in this chapter extends the linking algorithm by incorporating a *prior* knowledge of the vessel topology. A Metropolis-Hasting test is used to generate the sequence of draws in a Markov Chain simulation to obtain the maximum of a posterior (MAP) estimation of the vessel structure.

As we can see from the comparison plot of figure 4.12, the stochastic algorithm is more robust in the presence of uncertainties in the image with low signal to noise ratios.

To extend the stochastic linking algorithm into a full MCMC simulation to explore random space and obtain a better estimation of the p.d.f, more moves need to be added, such as adding/deleting branches and alternating the location of vertices. The detail of these proposals are discussed in the

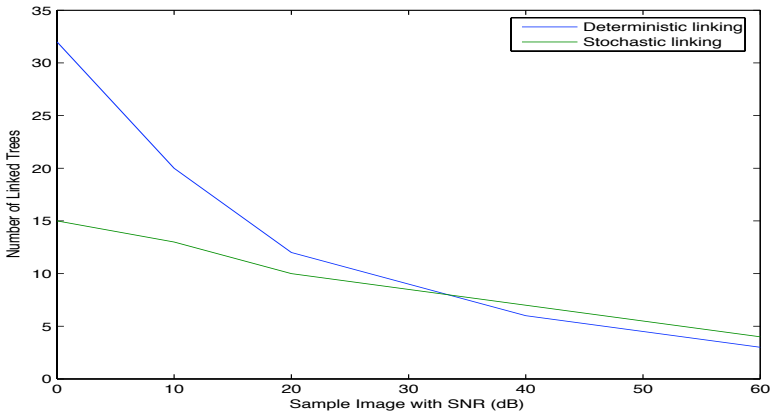

Figure 4.12: Number of linked trees increases more slowly using stochastic linking algorithm than deterministic strategy when the SNR is low

next chapter.

Chapter 5

Evaluation and Comparison

The goal of this chapter is to provide a quantitative analysis to verify the performance of the algorithms. For this purpose, two validation studies against manual measurements for diameters and branching angles were undertaken. Automatic measurements of individual bifurcations were compared with manual measurements for randomly chosen bifurcations from fundus retina images. The final classification results are also measured against the hand-labelled results. A specificity/sensitivity plot is produced to demonstrate the algorithm's performance. By means of comparison, two other commonly used methods are also discussed in length. Results from both methods are presented and a comparative analysis is given towards the end of the chapter.

5.1 Algorithm Evaluation

To verify the performance of the above mentioned methodology, experiments were carried out on twenty fundus image data sets provided by Hoover et al. [41]. The images were digitised slides captured by a TopCon TRV-20 fundus camera at 35 degree field of view. The slides were digitised to 700×605 pixels, 8 bits per colour channel. There are hand labelled images in the database observed by an expert. Evaluation is computed with the hand labelled results as ground truth.

A full parametric representation of the original image is generated from the neighbourhood linking strategy discussed in the previous chapter. By setting different threshold values of the standard deviation along the principal axes, a binary image of the two classes (vessel and background) can be obtained. The performance of the system is measured with a receiver operating characteristic (ROC) curve [108]. An ROC curve plots the sensitivity (Eqn: 5.1) against specificity (Eqn: 5.2) of the pixel classification. The closer a curve approaches the top left corner, the better the performance of the system. A single measure to quantify this behaviour is the area under the curve, A_{roc}, which is 1 for a perfect system. A system that makes random classifications has an ROC curve that is a straight line through the origin with slope 1 and $A_{roc} = 0.5$.

$$Specificity(SP) = \frac{FalseNegative(FN)}{(FalsePositive(FP) + FalseNegative(FN))} \quad (5.1)$$

$$Sensitivity(SE) = \frac{TruePositive(TP)}{(TruePositive(TP) + TrueNegative(TN))} \quad (5.2)$$

Using the multi-resolution H-G representation of the data (figure 5.1), three types of geometrical features are automatically measured: lengths, areas and angles. These measurements can lead to a potential application used in clinical practice since there are multiple eye diseases that affect the vasculature in the retina. For instance, hyper-tension increases retina artery dilation by as much as 35% [109]. Age and hyper-tension are thought to cause changes in the bifurcation geometry of retinal vessels [110]. Additionally, retinal arteriolar narrowing is an indication of the onset of diabetes and may be related to the risk of coronary heart disease for female patients [111]. Many of the diseases such as hyper-tension, angiogenesis and blood vessel congestion can also increase the tortuosity of the blood vessels[24].

5.1.1 Measuring the Width

The work presented here focuses on quantifying the thickness of the retinal vasculature. As stated above, the width of blood vessels is also an indication of many diseases. Typical vein diameter is about $100um$ near the optic

(a)

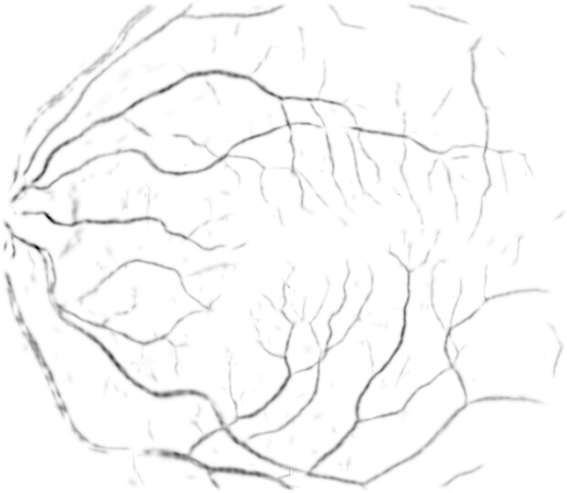

(b)

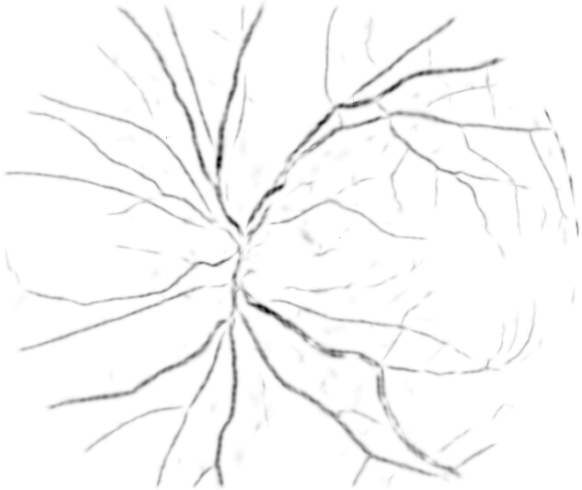

Figure 5.1: H-G representation of two original retina images (#IM0077 & #IM0163) after neighbourhood linking strategy.

disc and gradually reduces to approximately $20um$ towards the end of the vessel. It translates into 4-5 pixel diameter and can be as thin as 1 pixel depending on the resolution [66]. From the parametric Gaussian-Hermite representation of the image, further experimentation has been carried out to produce the binary output of the gray-level reconstruction image. Two types of approaches are provided to determine the factor of diameter estimation, i.e. where to cut Hermite-Gaussian tails to determine vessel edges.

The first approach is to use a simple iterative minimum mean square error (MMSE) fitting method to determine a threshold on the standard deviation of the H-G model on the minor axes which are perpendicular to the principal orientation of the vessel segments. A vessel/nonvessel classification can be produced based on the chosen threshold at each block of the H-G model. (see figure 5.2). The performance is examined by comparing the sensitivity vs specificity.(Eqn. 5.1 & 5.2). Table 5.1 shows the sensitivity and specificity result against the hand label images across the data set comprising 20 images. An optimum choice of threshold using the MMSE method yields a sensitivity of 82% and a specificity of 93%.

The second approach is to use a combination of global thresholding and local connectivity known as, *Hysteresis thresholding* [112]. An ordinary threshold operation, T, sets all pixels x of the input image I whose values lie in the range $[t_i, t_j]$ to 1 and all others to 0, i.e.

(a) Binary classification using MMSE

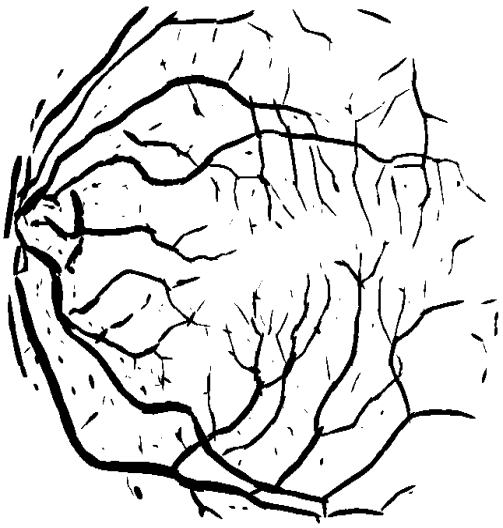

(b) Hand labelled classification

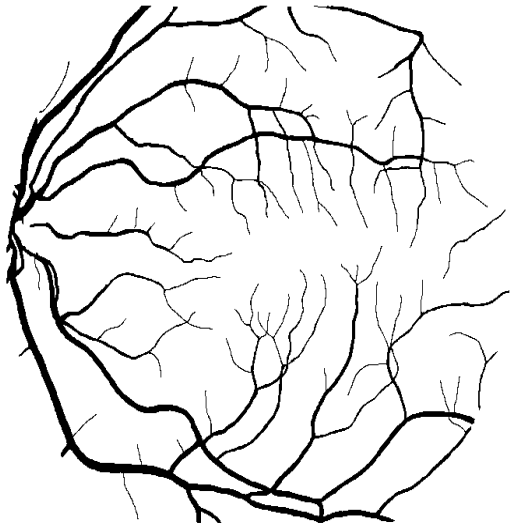

(c) Binary classification using MMSE

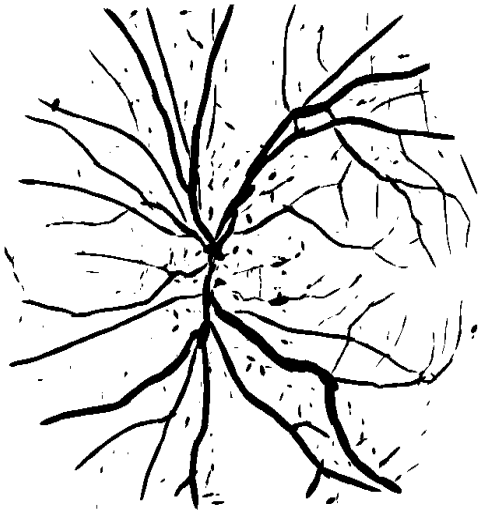

(d) Hand labelled classification

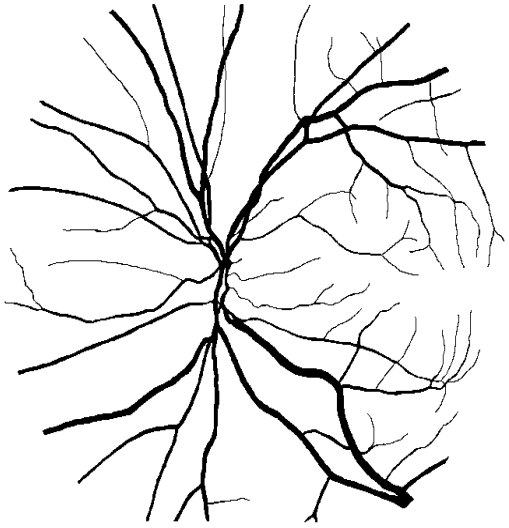

Figure 5.2: (a) & (c) Binary vessel, nonvessel classification results using MMSE, (b) & (d) Hand labelled ground truth classification results

Image	SE(%)	SP(%)	Image	SE(%)	SP(%)	Image	SE(%)	SP(%)
1	74.6	90.5	8	88.5	93.0	15	85.5	94.1
2	76.6	92.5	9	91.5	93.2	16	85.4	93.5
3	76.1	90.1	10	79.2	92.2	17	87.2	92.5
4	87.2	89.5	11	85.2	96.5	18	76.2	96.5
5	70.4	94.2	12	88.2	95.5	19	71.5	94.6
6	80.5	92.4	13	78.8	95.0	20	85.0	92.9
7	90.6	92.7	14	81.7	95.0			

Table 5.1: The table of SE/SP results across 20 images ($t_\sigma = 2$)

$$[T_{[t_i,t_j]}(I)](x) = \begin{cases} 1, & \text{if } t_i \leq I(x) \leq t_j, \\ 0, & \text{otherwise.} \end{cases} \tag{5.3}$$

The Hysteresis thresholding technique uses two threshold levels t_{low} and t_{high}. Pixels with intensity value higher than t_{high} are set to 1 (vessel) and those with value lower than t_{low} are set to 0 (background). Then, a local connectivity process is implemented to relax the thresholding, i.e. pixels that have an intensity value between (t_{low}, t_{high}) and that are connected to pixels above t_{high} are also set to 1 (vessel). The relaxation procedure uses the property of tree like structures, i.e vessels are connected to each other, to classify small/thin vessels that have similar intensity values with some background features. Figure 5.4 shows the binary results obtained by this method. An alternative way of presenting this information is use a receiver-operating characteristic (ROC) curve, (figure 5.3). This is a plot of $(1 - Sp)$ versus Se, the closer the curve is to the top left corner, the better the

performance. The Hysteresis thresholding algorithm brought the average sensitivity to 78% and specificity to 88% over the entire date set. The result is less accurate than using the MMSE algorithm due to the large variety of blood vessel intensities across different images.

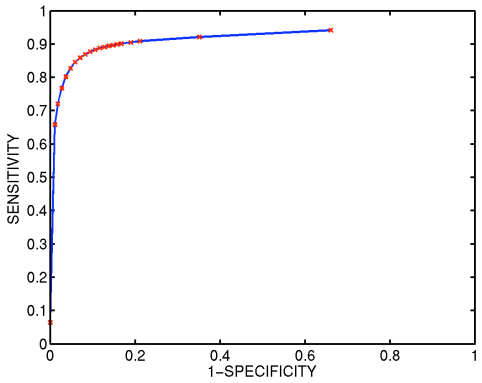

Figure 5.3: ROC curve on a sample image by varying the binarisation threshold $t_\sigma = (0.5 - 3.5)$

Classification results can be verified by comparing the sensitivity and specificity. However, this calculation is pixel based and does not take into account the object size. To verify how well the algorithm is detecting thick vessels and small vessels, we measured the width at every point in the vessel segment skeleton. The width at a skeleton point Sp is defined as the largest line segment passing through the point Sp that is perpendicular to the principal orientation of the vessel segment.

Figures 5.5 and 5.6 show the plots of the width of vessels in the H-G classification results and hand labelled images. Figure 5.7 shows the width

(a) $t = 2$

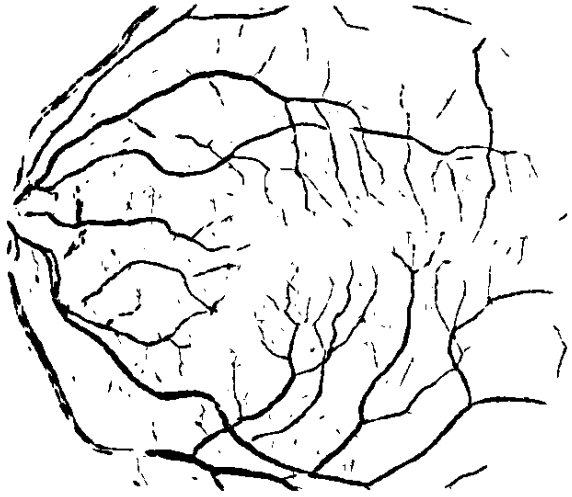

(b) $t = 4$

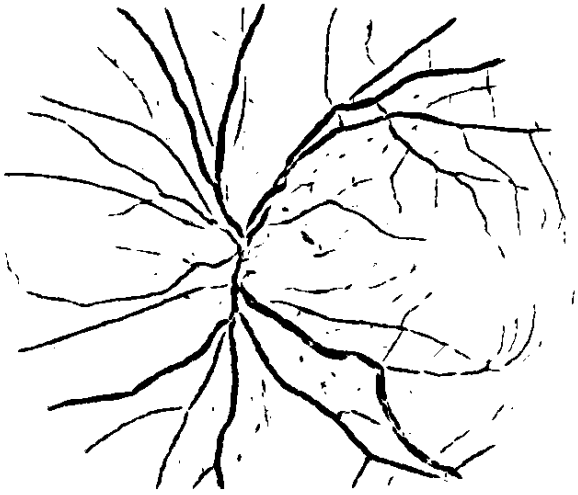

Figure 5.4: Binary classification of same images as in figure 5.2 but after using the hystersis thresholding technique.

histogram of the sum of twenty images in the data set. The similarity between the two histograms shows that H-G segmentation and the classification method are able to detect the majority of main blood vessels as well as small vessel segments.

5.1.2 Measuring Length and Tortuosity

Based on the measurement of arc length, the tortuosity of the vascular structure can be quantified. Information about disease severity or change of disease with time may be inferred by measuring the tortuosity of the blood vessel network [113].

The length and curvature of the blood vessels are calculated based on a skeletonized binary image representing the centre line of vasculature (figure 5.8). The arc length of a vessel segment C is defined as

$$s(C) = \int_{t_0}^{t_1} \sqrt{x'(t)^2 + y'(t)^2} dt \tag{5.4}$$

The chord length (straight length) of C is

$$ch(C) = \sqrt{(x(t_0) - x(t_1))^2 + (y(t_0) - y(t_1))^2}. \tag{5.5}$$

where t_0 and t_1 are the start and end points of the vessel segment. The

(a) Classification using MMSE

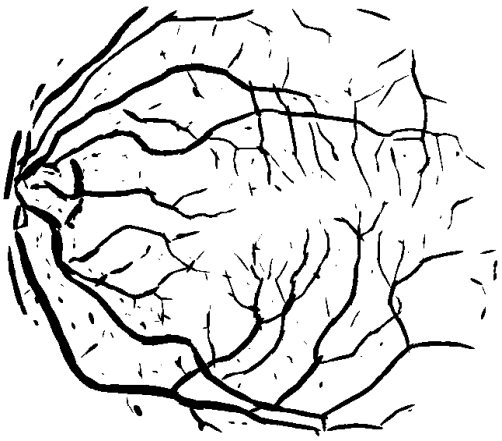

(b) Hand label image.

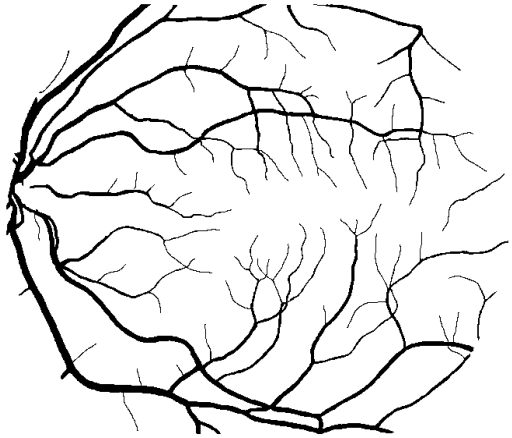

(c) Plot of the width of vessels

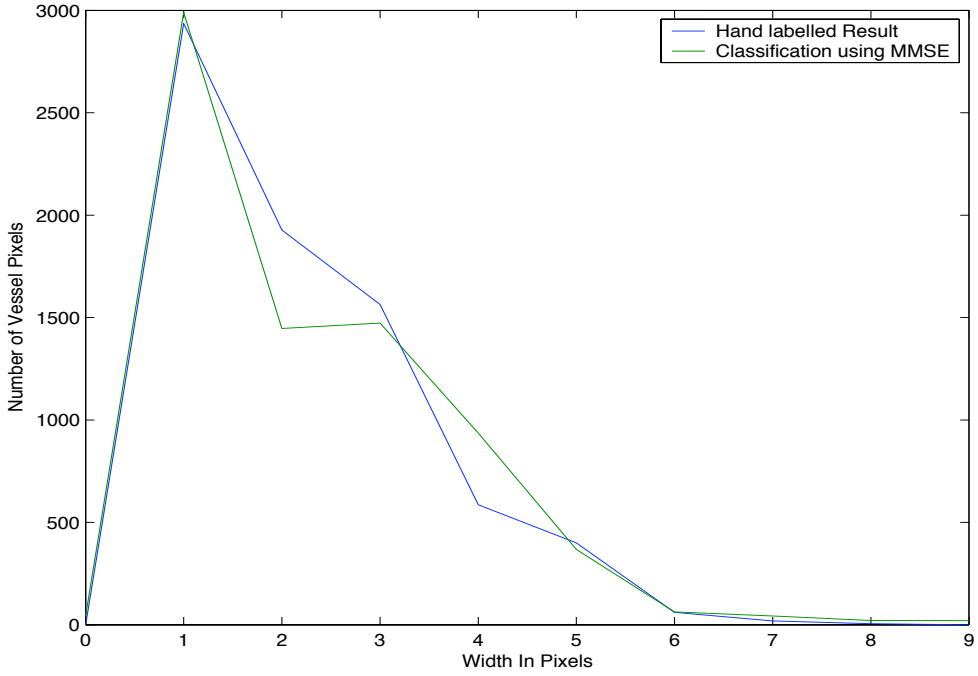

Figure 5.5: Plot of the width of vessels of hand label and automatically classified images (#IM0077).

(a) Classification using MMSE

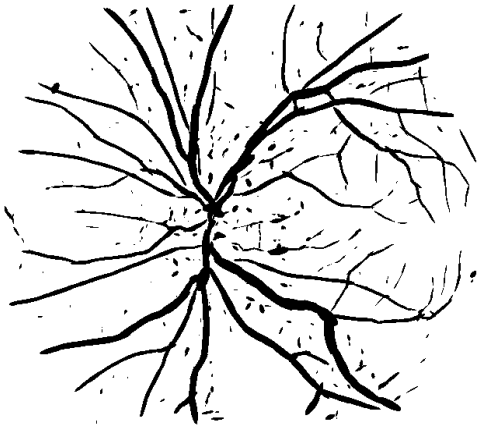

(b) Hand label image.

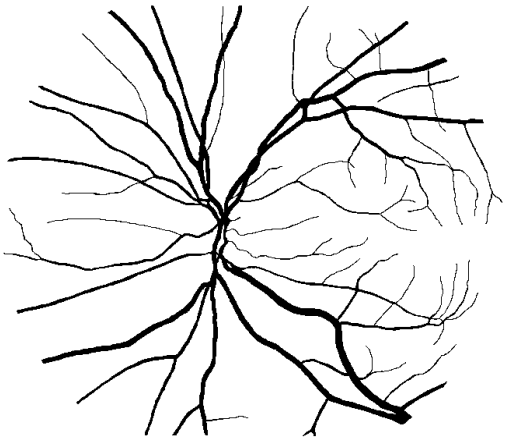

(c) Plot of the width of vessels

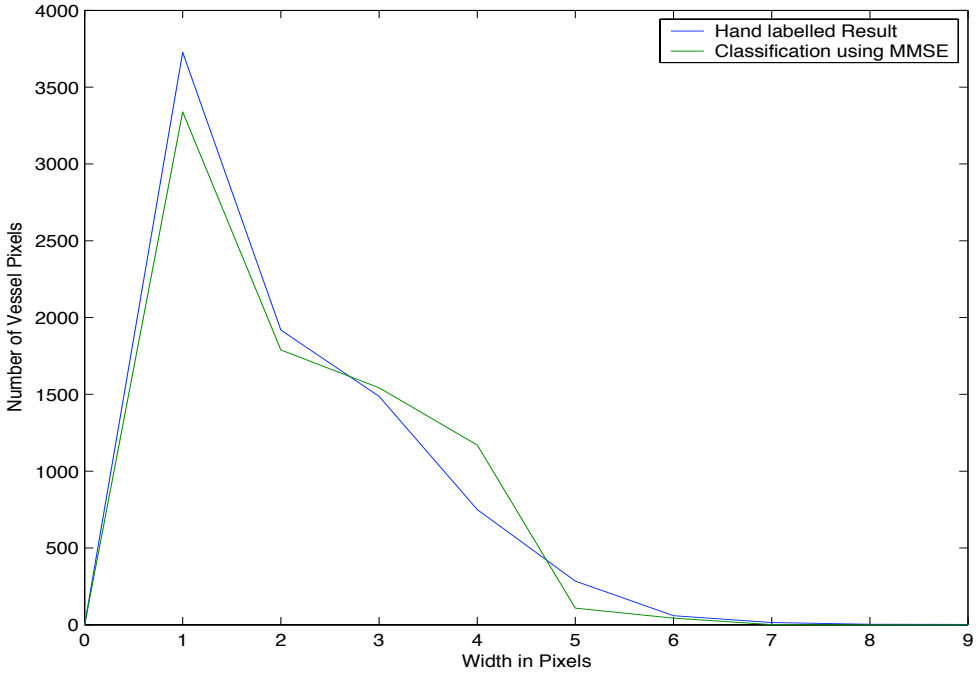

Figure 5.6: Plot of the width of vessels of hand label and automatically classified images (#IM0163).

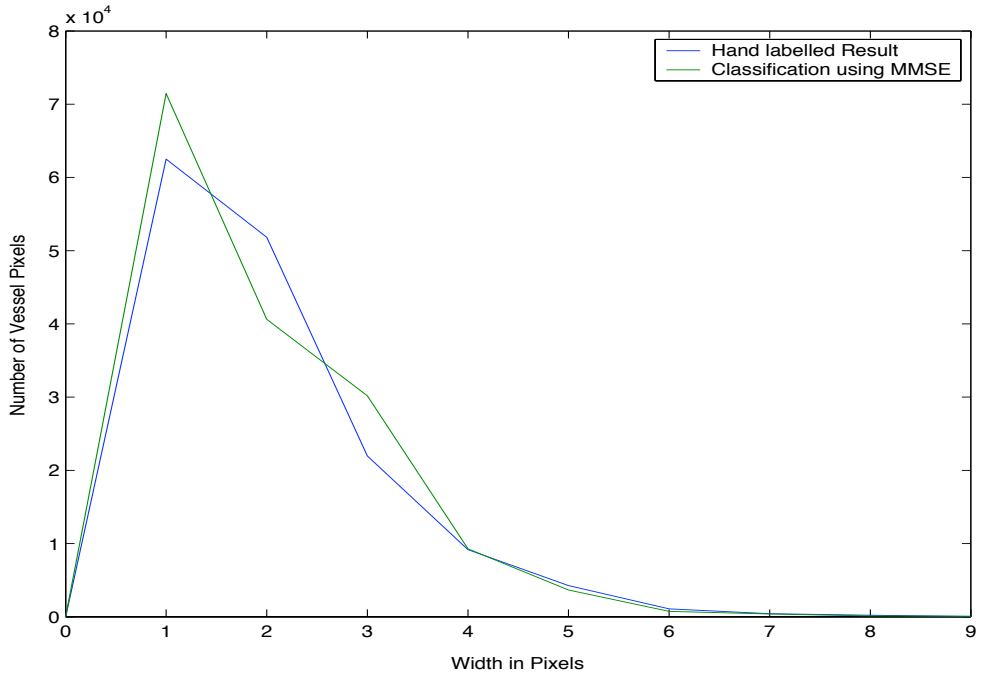

Figure 5.7: Plot of the width of vessels of hand label and automatically classified images (sum of twenty images in the data set).

curvature at point t is also defined as

$$\kappa(t) = \frac{x'(t)y''(t) - x''(t)y'(t)}{[y'(t)^2 + x'(t)^2]^{3/2}} \tag{5.6}$$

The total curvature of a curve segment is $tc(C) = \int_{t0}^{t1} |\kappa(t)^2|$.

In this section, two types of measurements are used to calculate the vessel

tortuosity.

$$\tau_1 = s(C)/ch(C) \tag{5.7}$$

$$\tau_2 = tc(C)/ch(C) \tag{5.8}$$

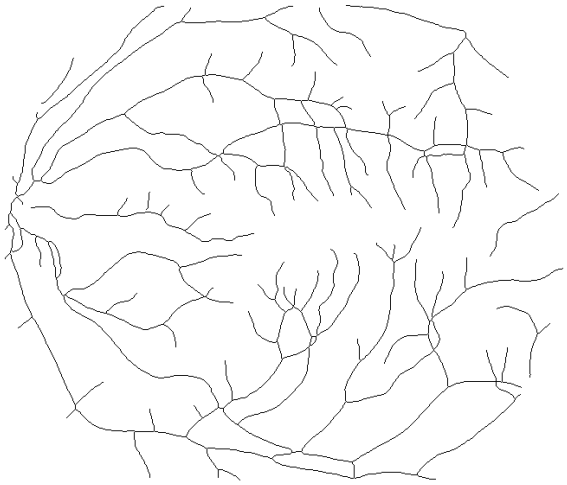

Figure 5.8: Skeleton image generated from the auto-classification result.

The measure τ_1 simply measures the tortuosity of the vessel segment by examining how long the curve is relative to its straight length. It is called *distance factor tortuosity measure*, described by Smedby [114]. The drawback of this measurement is that it can not distinguish the two types of vessels which have different pathological meaning (see figure 5.9). An alternative way of measuring tortuosity is using τ_2 defined above, which is named the *length normalised total curvature measure* [114]. Using this type of measurement, figures 5.9 (a) and (b) can be very well distinguished.

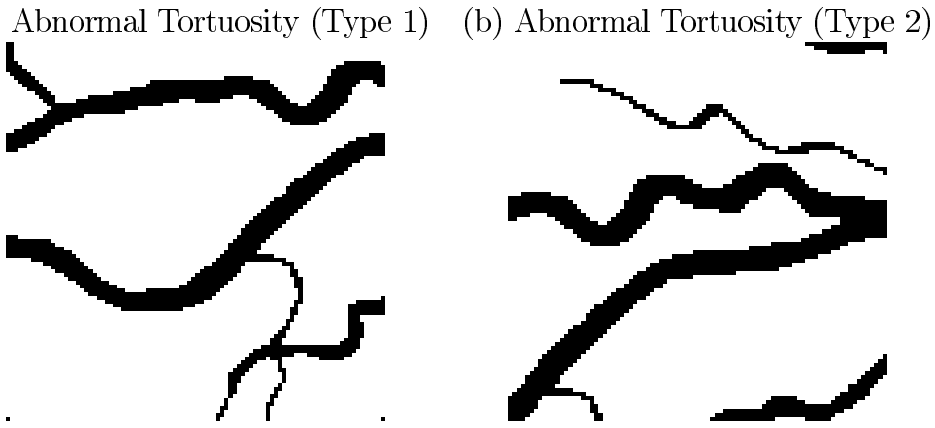

Figure 5.9: (a) Sinuours curves in long normally straight vessels. $\tau_1 = 1.3$, $\tau_2 = 0.4$. (b) Tight coils or sine waves $\tau_1 = 1.35$, $\tau_2 = 1.2$.

5.1.3 Accuracy of Width and Tortuosity Measurement

To verify the accuracy of the measurement of width and tortuosity, a synthesised image containing a set of different features (figure 5.10) was created. The image contains 'vessels' of known width, length and tortuosity. The straight vessels on the left of figure 5.10(a), range in width from 1 to 10 pixels. The tortuous vessels on the right side are simple sinusoidal curves with different frequency and amplitude, the diameter of the curves is 3 pixels.

The measured tortuosity and width are compared with the theoretical tortuosity and known width for this noise free sample. The results are almost identical. Figure 5.10(b) shows the measured tortuosity against the ideal tortuosity value. Due to the discrete nature of the image, pixels have a finite size hence measuring the distance from centre to centre of each pixel will

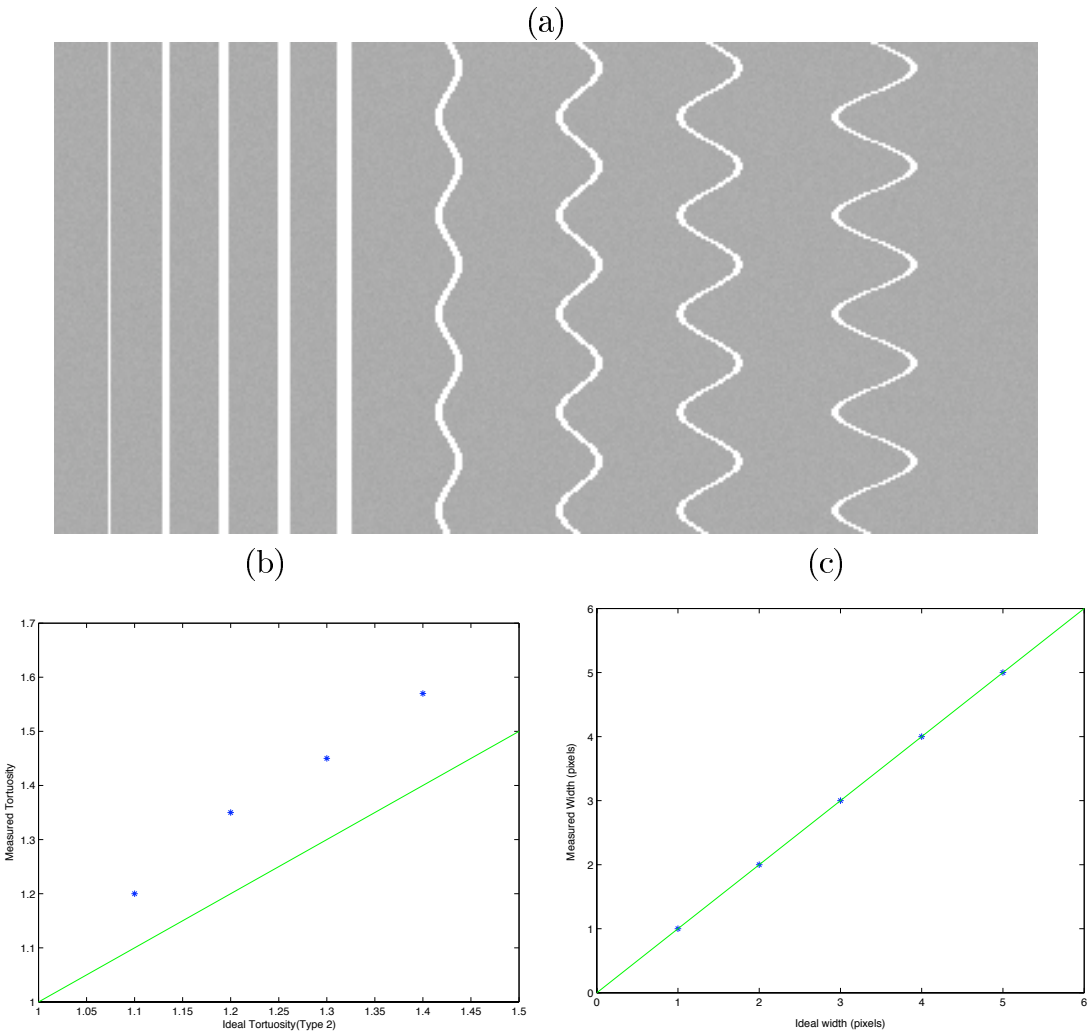

Figure 5.10: (a) A simple test image that was used to test the accuracy of vessel width and tortuosity measurement. The test image consists of linear features of known width between 1 and 5 pixels and 4 sine waves with known tortuosity between 1.1 to 1.5. (b) A comparison between vessel tortuosity τ_2 measured using the automated technique and theoretical tortuosity. A consistent bias is seen due to finite geometric effects. (c) A comparison between vessel width measured using MMSE technique and actual real vessel width.

force a theoretically smooth curve to follow a zig-zag path with a longer length. The tortuosity measuring algorithm τ_2 consistently over-estimates the tortuosity by some constant value.

Figure 5.11 shows the results of the same experiment but on an image with $SNR = 1$. From the results shown in figures 5.11(b) and 5.11(c), we can see that despite the low SNR of the image, the width and tortuosity measurement is still very similar to the theoretical values.

5.1.4 Detection of Vascular Intersections and Bifurcations

Vascular intersections and bifurcations are important landmark points for registration and segmentation processes [93] [15]. Corner and branch point detection algorithms can be broadly classified into those that first estimate image boundaries or curves using image gradient operators of one sort or another and then infer the position of the junction, to those that directly apply a curvature measure or template to the grey level data. Methods that use the intersections of boundaries to label corners necessitate the thinning of curves to a single pixel width e.g. skeletonisation. Because of ambiguities caused by the line thinning, the subsequent labelling of branch points can be problematic, particularly in 3D. In general, methods that use second or greater order differentials of the image intensity are sensitive to noise, whereas template

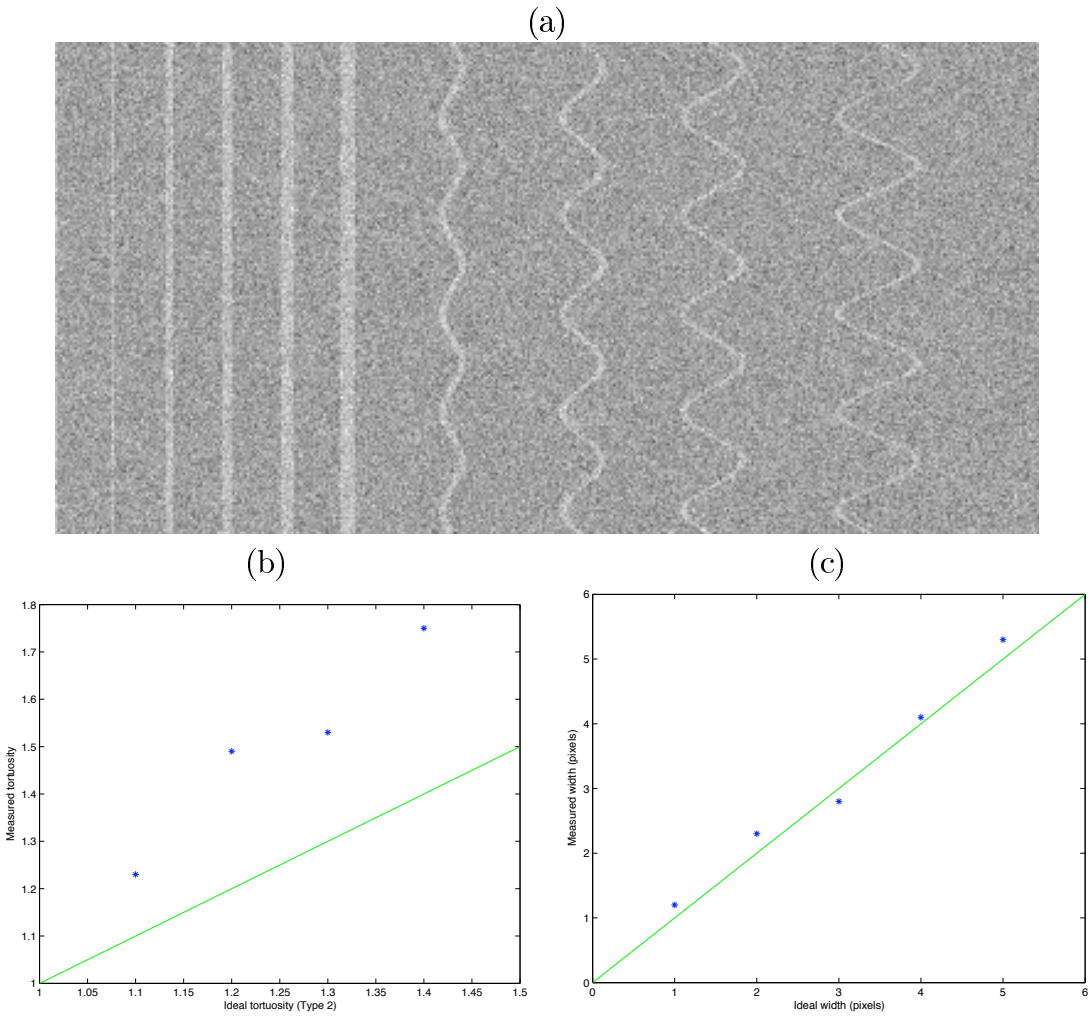

Figure 5.11: (a) A simple noisy test image (SNR=1) that was used to test the accuracy of vessel width and tortuosity measurement. The test image consists of linear features of known width between 1 and 5 pixels and 4 sine waves with known tortuosity between 1.1 to 1.5. (b) A comparison between vessel tortuosity τ_2 measured using the automated technique and theoretical tortuosity. A consistent bias is seen due to finite geometric effects. (c) A comparison between vessel width measured using MMSE technique and actual real vessel width.

approaches are limited in the range and type of branch points that can be described [115]. Scale-space curvature provides some trade-off between these approaches because of the noise immunity gained by repeated smoothing, plus the ability to naturally model the size of features and by tracking curvature through scale, allowing labelling decisions to be confirmed by comparing estimates at different scales in the feature space.The disadvantages are that branch points are not modelled explicitly and the implementation does not readily extend to 3D [52].

Based on the Multiresolution Hermite-Gaussian modelling and feature selection scheme, potential areas which contain branch points or crossovers can be identified by highlighting the multiple Gaussian $M > 1$ regions. A skeleton of the classification result after the application of the Bayesian linking algorithm is also used to verify the type of intersections. The detection process contain two steps:

- Highlight all the regions represented by multiple Gaussian models $M > 1$ from the AIC model selection result, (see figure 5.12). Potential bifurcations are identified by labelling the intersection of the Gaussian functions at each region.

- High curvature and crossover points from figure 5.12 can be eliminated by examination of the skeleton results, (figure 5.13), i.e. a point is classified as a bifurcation if only 3 of its neighbours are vessel points.

Figure 5.14 shows the results of branching points detection.

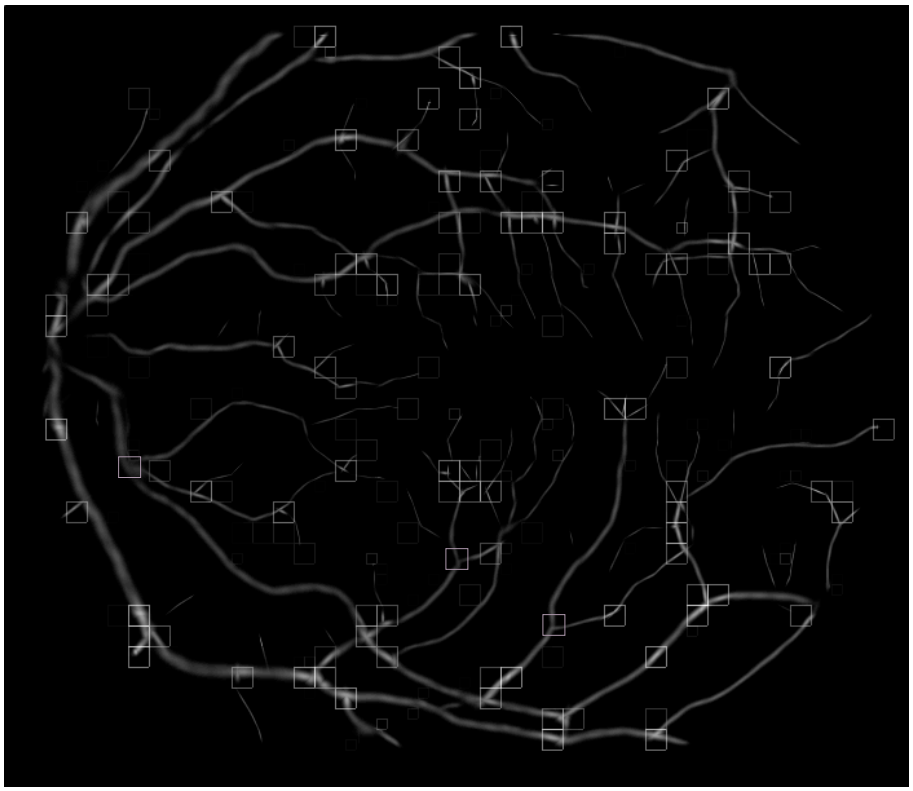

Figure 5.12: Potential branch point regions are identified by highlighting the area using multiple Gaussian models $M > 1$.

The accuracy of the algorithm are also assessed by comparing the automatic detection against human measurement and yield 95% specificity and 92% sensitivity.

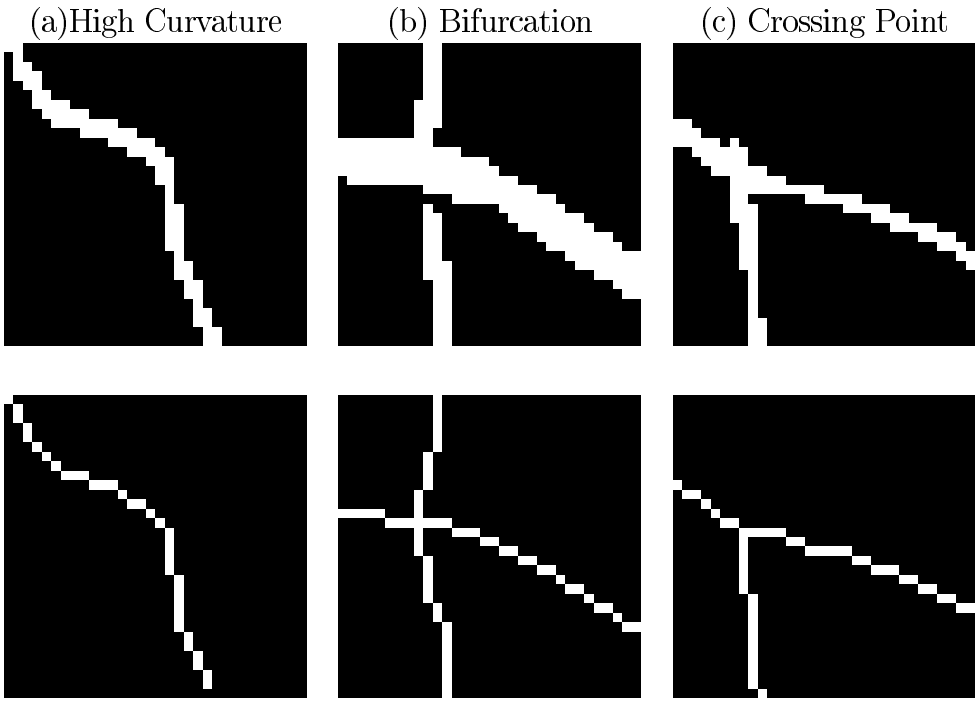

Figure 5.13: The binary and skeleton of three types of feature.

5.2 Comparison Between Different Algorithms

5.2.1 Scale Space Method

The basic idea behind a scale-space representation is to separate out information at different scales [20]. Any image can be embedded in a one-parameter family representation which is derived by convolving the original image $F(\mathbf{x})$ with Gaussian kernels of increasing variance t. For any N-dimensional signal, $I : R^N \rightarrow R$, the scale-space representation $S : R^N * R_T \rightarrow R$ is defined by letting the scale-space representation at zero scale be equal to the original

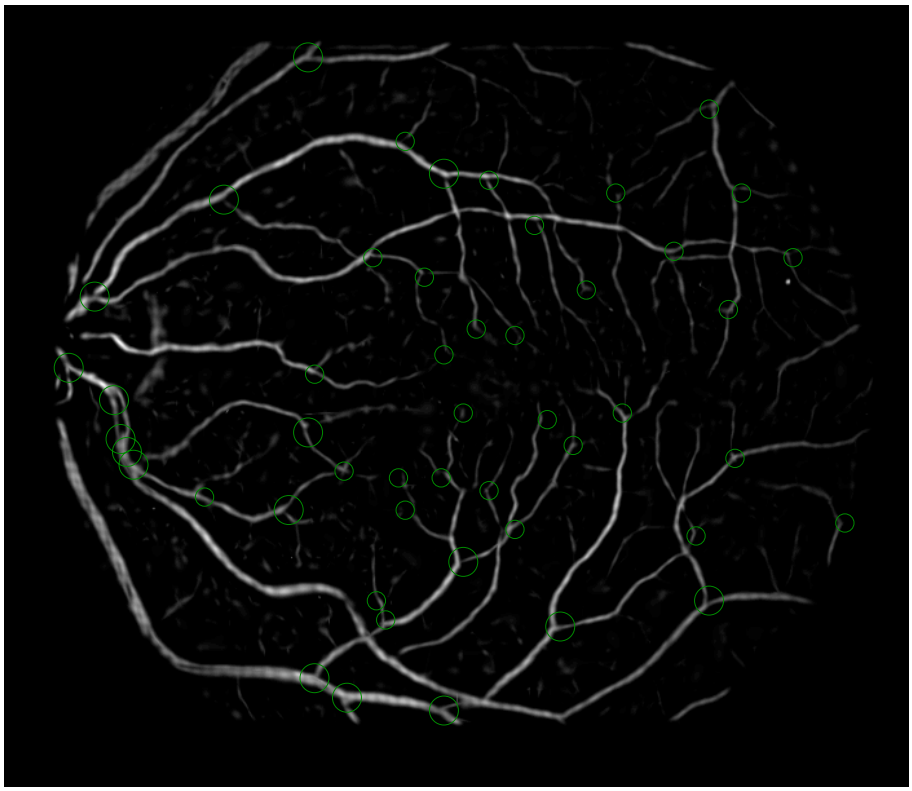

Figure 5.14: Bifurcations are extracted by verifying the skeletonisation of the binary classification results.

signal $L(:;0) = f(x)$ and for $t > 0$,

$$L(\mathbf{x};t) = F(\mathbf{x}) * \mathcal{G}(\mathbf{x};t) \tag{5.9}$$

where $\mathcal{G}(\mathbf{x};t)$ denotes the Gaussian kernel which can be written as

$$\mathcal{G}(\mathbf{x};t) = \frac{1}{(2\pi t^2)^{\frac{D}{2}}} e^{-\frac{x^T x}{2t}} \tag{5.10}$$

in an arbitrary dimension D.

Under this representation, for a 2D image, the multi-scale spatial derivatives can be defined as;

$$S_{\mathbf{x}^n}(\mathbf{x};t) = F(\mathbf{x}) * \mathcal{G}_{\mathbf{x}^n}(\mathbf{x};t) \tag{5.11}$$

where $\mathcal{G}_{\mathbf{x}^n}$ denotes a derivative of some order n.

With the Gaussian scale-space representation, the fine scale information is suppressed with increasing values of the scale parameter. The use of Gaussian convolution as a smoothing operation satisfies certain sufficiency requirements such as the new local extrema cannot be created when increasing the scale-parameter t. It was first proved by Koenderink [116] who also introduced an extension of the scale-space theory to higher dimensions. He introduced the concept of *causality*, which means that new level surfaces must not be created in the scale-space representation when the scale parameter is increased. It has been proved that the family is uniquely determined to consist of Gaussian Kernels [20].

The use of Gaussian kernels also ensures that the objects in the images are invariant with respect to translation, rotation and scaling which are important properties for the scale-selections and feature detection. One of the most useful properties in linear scale-space theory is that to calculate the

derivative of the observed image,

$$L = F * \mathcal{G} \tag{5.12}$$

We may interchange the differential and the convolution operator due to their linear property

$$L_x = \frac{\partial}{\partial x}(F * \mathcal{G}) = F * \frac{\partial \mathcal{G}}{\partial x} \tag{5.13}$$

Therefore, a derivative of the observed image can be calculated by convolving the original signal F with a Gaussian derivative operator. In order to keep the structure at different scales in a similar manner, a scale-normalised Gaussian derivative operator can be defined as;

$$\frac{\partial^n G}{\partial \tilde{x}^n} \rightarrow t^n \frac{\partial^n G}{\partial \tilde{a}^n} \tag{5.14}$$

where $\tilde{x} \rightarrow \frac{x}{t}$.

The above mentioned, Gaussian filtering, followed by derivative computations can be used as initial steps in early processing of image data and a framework for relating filters of different types and at different scales. However, such linear filtering cannot be used as the only component in a vision system aimed at deriving symbolic representations from images. Some further steps are required for combining the output of these Gaussian derivative operators of different orders and at different scales into more explicit descriptors of the image geometry.

In the particular case of retinal blood vessels, gradient magnitude and principal curvatures are used in order to detect the edge and ridges of vascular structure. According to the notion of non-maximum suppression, an edge point is defined as a point at which the gradient magnitude assumes a maximum in the gradient direction [112] [117]. After expansion to Cartesian coordinates and simplification, this edge definition assumes the form

$$\begin{cases} L_x^2 L_{xx} + 2L_x L_y L_{xy} + L_y^2 L_{yy} = 0 \\ L_x^3 L_{xxx} + 3L_x^2 L_y L_{xxy} + 3L_x L_y^2 L_{xyy} + L_y^3 L_{yyy} < 0 \end{cases} \tag{5.15}$$

A ridge point is a point for which the intensity image has a local maximum in the direction for which the gradient of the image undergoes the largest concavity [118]. A ridge detector can be expressed in a conceptually similar way, at points where the gradient does not vanish, a ridge can be expressed as follows

$$\begin{cases} L_x L_y (L_{xx} - L_{yy}) - (L_x^2 - L_y^2) L_{xy} = 0 \\ (L_x^2 - L_y^2)(L_{xx} - L_{yy}) - 4L_x L_y L_{xy} > 0 \end{cases} \tag{5.16}$$

In Martinez's [15] work, gradient magnitude strength is measured using Canny's optimal kernel, i.e. a point is weighted by the magnitude of its gradient for a particular value of scale-space parameter t and the first derivatives

of an image $F(x, y)$ are defined as

$$\begin{cases} L_x = F(x, y) * tG_x \\ L_y = F(x, y) * tG_y \end{cases} \tag{5.17}$$

where the gradient magnitude is defined as $|\nabla L| = \sqrt{(L_x^2 + L_y^2)}$.

To extract the ridge information, we need to calculate the second derivatives of the intensity image:

$$\begin{cases} L_x x = F(x, y) * t^2 G_{xx} \\ L_x y = F(x, y) * t^2 G_{xy} \\ L_y y = F(x, y) * t^2 G_{yy} \end{cases} \tag{5.18}$$

Derived from the Hessian Matrix of the intensity image $F(x, y)$, the maximum eigenvalue $|\lambda_{max}|$ which corresponds to the *maximum principal curvature* is defined as:

$$\lambda_{max} = max[\frac{L_{xx} + L_{yy} \pm \sqrt{(L_{xx} + L_{yy})^2 + 4L_{xy}^2}}{2}] \tag{5.19}$$

Once the whole stack of images with edge and ridge responses are obtained, an automatic scale selection algorithm [119] is then used to select levels from the scales at which normalised measures of feature strength as-

sume local maxima with respect to the scale. Figures 5.15 and 5.16 show two scale-space representations with the local maxima along the scales for the two example images from the data set after applying the scale-normalisation factor to each level, i.e.

$$\beta = max_t[\frac{|\nabla L(t)|}{t}]; \qquad \gamma = max_t[\frac{|\lambda(t)|}{t}] \tag{5.20}$$

Using the maximum response of these two features, β and γ, an iterative relaxation technique is then employed to perform a foreground/background classification based on the Otsu threshold algorithm [120]. Mean and standard deviation of two classes μ_v, σ_v (*vessel*) and μ_b, σ_b *background* of image γ are calculated respectively from the histogram. The gradient information, μ_g, σ_g, are also calculated from the histogram of image β.

The algorithm includes two stages. Firstly, an unlabelled pixel is classified to belong to class i if it has at least one neighbour of class i already classified and if it fulfils a specific condition with initial parameters $a_i = 1$ (Eqn: 5.21). Growing is repeated until no more pixels are classified. The parameter a_i is relaxed by 0.5 at each growing step.

(a) Maximum Edge Response β

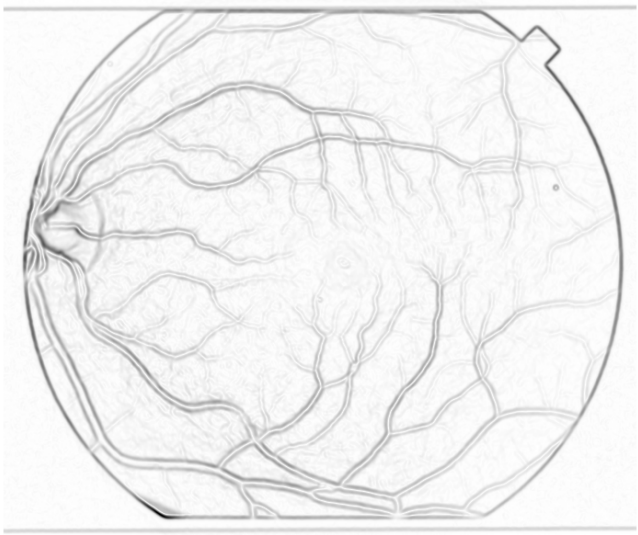

(b) Maximum Ridge Response γ

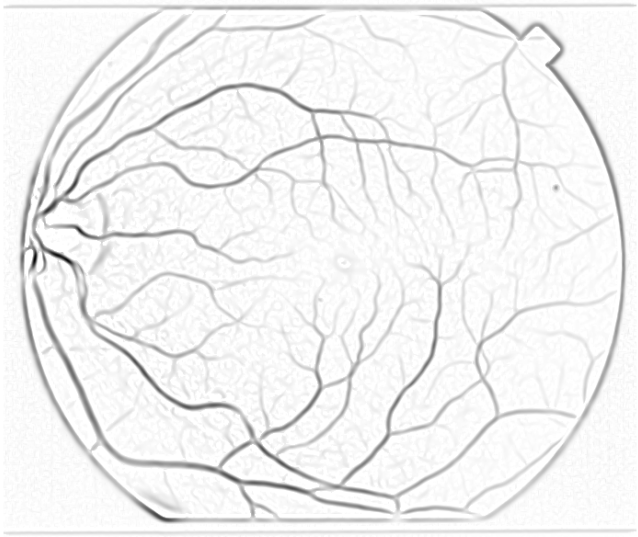

Figure 5.15: (a) Maximum gradient magnitude strengths along the scales-space representation. (b) Maximum ridge response along the scale-space representation (#IM0077).

(a) Maximum Edge Response β

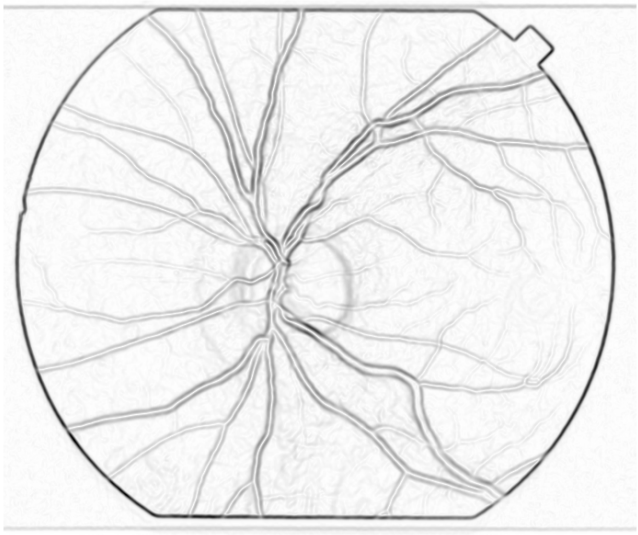

(b) Maximum Ridge Response γ

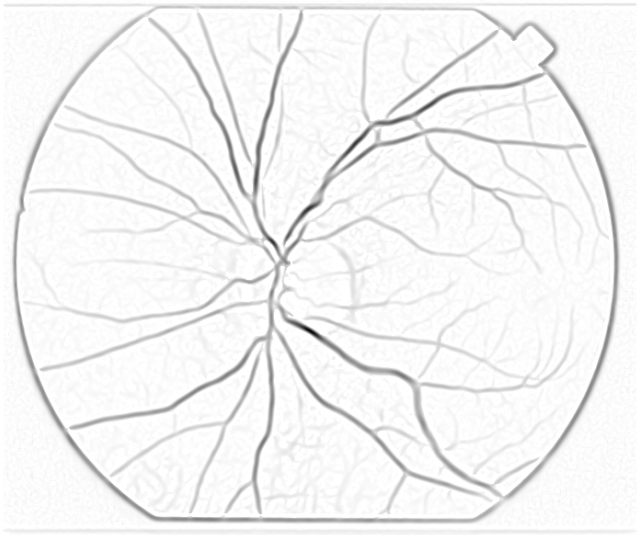

Figure 5.16: (a) Maximum gradient magnitude strengths along the scales-space representation. (b) Maximum ridge response along the scale-space representation (#IM0163).

$$\begin{cases} \textit{Vessel if: } \gamma \geq (\mu_v - a_v\sigma_v)\ AND\ \beta \leq (\mu_g + a_g\sigma_g)\ AND\ N_v \geq 1 \\ \textit{Background if: } \gamma \leq (\mu_b + a_b\sigma_b)\ AND\ \beta \leq \mu_g\ AND\ N_b \geq 1 \end{cases} \tag{5.21}$$

where μ_v, σ_v are the mean and standard deviation of vessel and N_i is the number of neighbours already labelled as class i.

The second stage of the relaxation process is to grow vessel and background classes simultaneously without the gradient restriction.

$$(\mu_i - a\sigma_i) \leq \gamma \leq (\mu_i + a\sigma_i)\ AND\ N_i \geq 1 \tag{5.22}$$

The classification results are shown in Figure 5.17.

In table 5.2, specificity and sensitivity results for the whole data set are listed. Using the scale-space region growing technique, an average of 72% sensitivity and 80% specificity is achieved.

5.2.2 Matched Filter Response Method

Another typical enhancement-detection process in the **STARE** project [42] [121] [41] approximates the gray level profile of the cross section of a blood vessel by a Gaussian shaped curve with fixed width and orientation. The concept of

(a) Sensitivity=78% & Specificity=82%

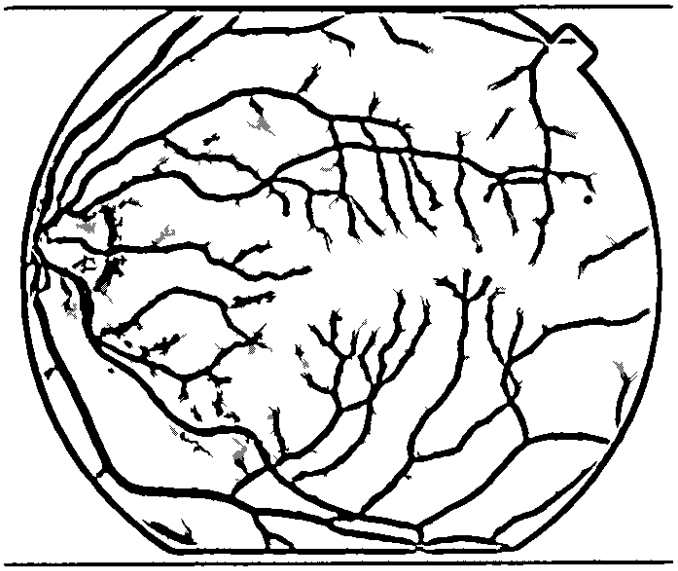

(b) Specificity = 75% & Specificity=80%

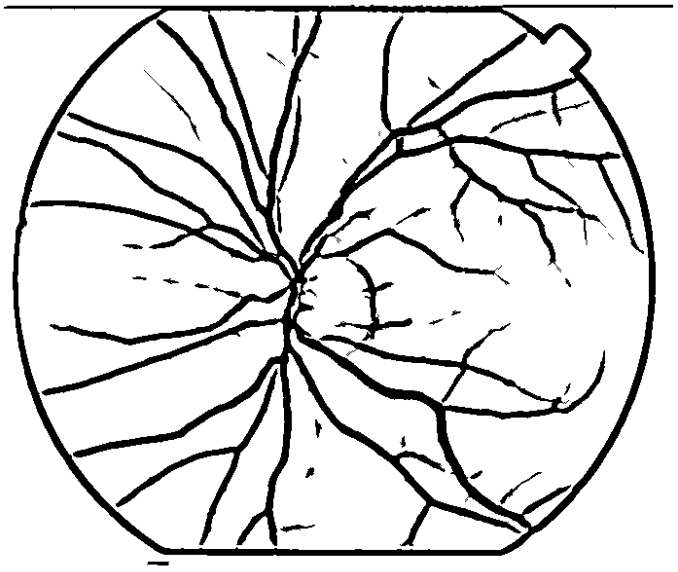

Figure 5.17: Classification results for two sample images using Otsu thresholding and region growing.

Image	SE(%)	SP(%)	Image	SE(%)	SP(%)	Image	SE(%)	SP(%)
1	68.6	80.5	8	68.5	73.0	15	75.0	80.2
2	70.2	72.5	9	78.3	73.2	16	65.9	78.3
3	76.3	75.3	10	78.2	82.1	17	63.8	72.5
4	81.2	85.5	11	67.2	76.5	18	71.8	76.7
5	60.5	90.2	12	80.4	85.5	19	71.5	84.6
6	65.2	91.4	13	81.8	78.4	20	74.2	82.1
7	73.6	73.7	14	60.6	90.5			

Table 5.2: Table of SE/SP using region growing method across 20 images ($t_\sigma = 2$)

matched filter detection of signals was used to enhance blood vessels. An inverted Gaussian-shaped zero-sum matched filter rotated by twelve discrete angles of 15^o each was designed to detect piecewise linear segments of blood vessels. A threshold probing method is then used to segment blood vessels from the background. At each iteration, region based attributes of the segments are tested to consider probe continuation and ultimately to decide if the segments are vessels. Pixels from probes that are not classified as vessel are recycled for further probing.

5.2.2.1 Matched Filter for Blood Vessels

In essence, matched filter technique describes the expected appearance of a desired signal from the original image. In [42], the gray-level profile of the cross section of a blood vessel is approximated by a Gaussian shaped curve. The concept of matched filter detection is used to detect piecewise linear

segments of blood vessels in retinal images. Blood vessels usually have poor local contrast. A set of two dimensional segment profiles, in equiangular rotations, is used as a filter bank to cover vessels appearing in different orientations. The kernels are designed to convolve with the original image in order to enhance the blood vessels. The filters are implemented using twelve 16×16 pixel kernels. A prototype matched filter kernel is expressed as

$$K_i(x, y) = -exp(-x^2/2\sigma^2), for|y| \leq L/2 \tag{5.23}$$

where L is the length of the segment for which the vessel is assumed to have a fixed orientation. In equation 5.23, the direction of the vessel is assumed to be aligned along the y-axis, however, since the vessel may be oriented at any angle, the kernel needs to be constructed to span all possible orientations. The details for computing the actual values in the kernels may be found in [42]. Original images are convolved with all twelve kernels and the matched filter response (MFR) is taken as the value of the highest scoring kernel at each pixel.

5.2.2.2 Threshold Probing

An iterative probing technique is then performed on the matched filter response (MFR) image. During each probe, a set of criteria are tested to determine the threshold of the probe to ultimately decide if the area being

probed is a blood vessel. To identify the start and end point of each vessel segment, the following steps are needed:

- After producing the MFR image by convolving the matched filter described in [42], a threshold value based on the histogram is chosen to produce a binary image.
- A standard thinning algorithm is used to generate the skeleton image.
- In the skeleton image, all branch points are erased and the vessel network is broken into segments that contain two endpoints.
- Segments with less then ten pixels are discarded.

This process of initialisation allows the pixels with a strong response to the matched filter to act as candidate vessels. Unlike tracking-based methods [55] [95] [54], these starting points can be at any position in the vessel network, therefore, pathology and branches do not cause parts of the network to be missed [41]. After identifying the start and end points, an iterative probing/thresholding relaxation technique is used to grow the region. Once the region growing is completed, the desired attributes of the grown region are tested. Passed regions are labelled as vessel and failed ones remain unlabelled. In either case, the next starting point will be selected for probing. The algorithm is complete after exploring all the candidate points.

Final classification results are presented in figure 5.18.

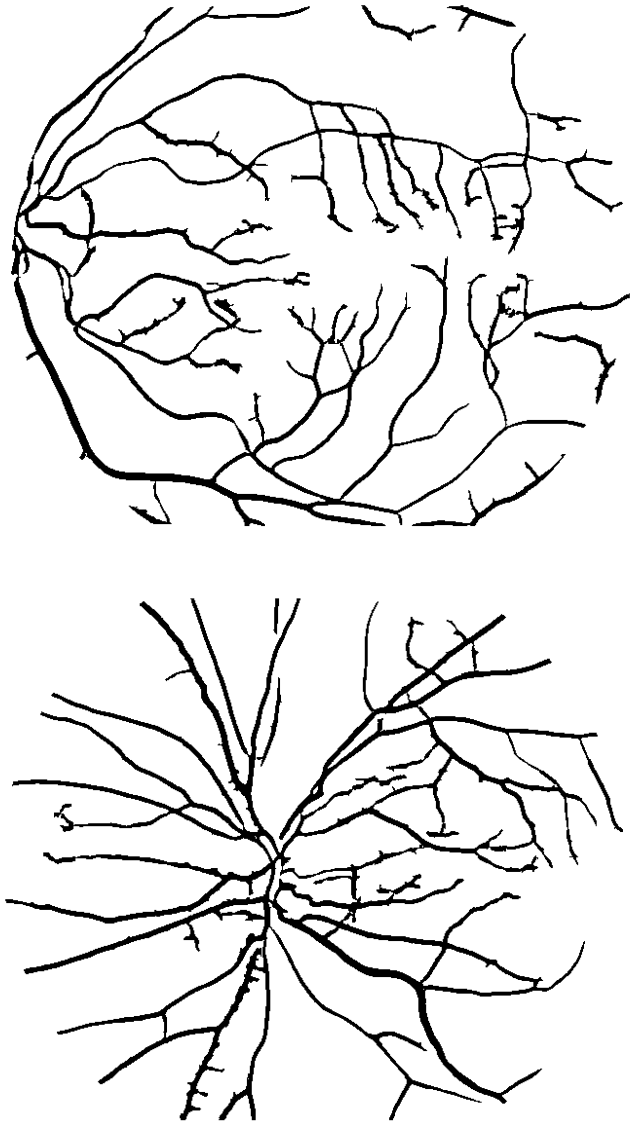

(a)

(b)

Figure 5.18: Classification results using probing algorithm based on matched filter response.

Using this algorithm 83% sensitivity and 90% specificity are achieved, which compares well with the H-G modelling algorithm. However, a his-

togram of the width of the blood vessels (figure 5.19) shows that during the Gaussian filter procedure, the widths of original vessels have been altered. The peak of the histogram is shifted to the right compared with the hand labelled result, indicating that there are more small vessels that have been miss-detected using this algorithm.

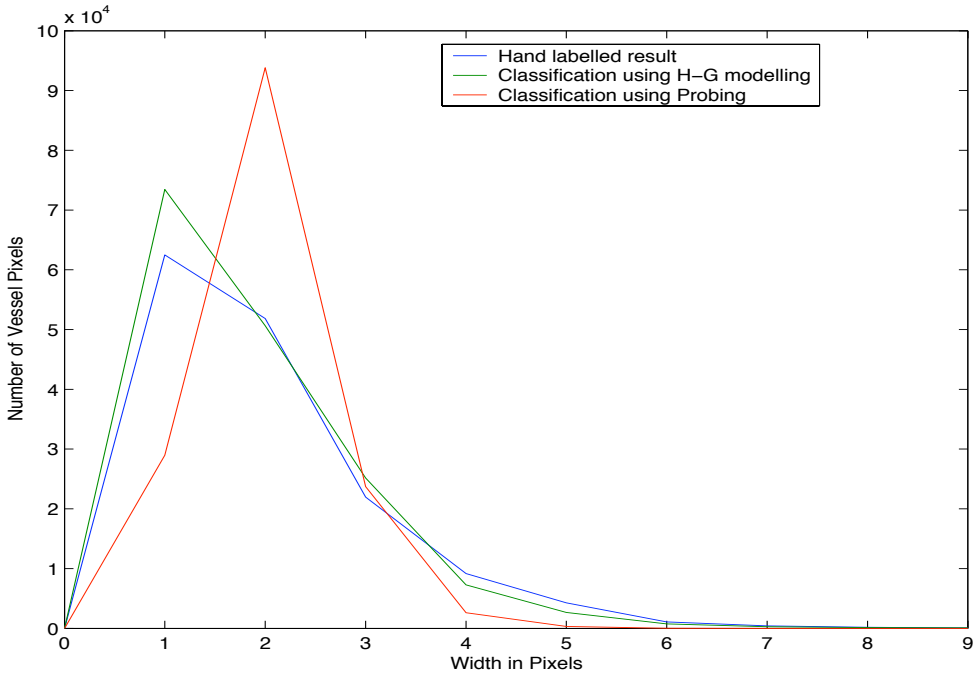

Figure 5.19: Plot of the width of vessel pixels between hand label images and the auto-classification results using different methods.

5.3 Summary

This chapter focuses on the evaluation of the algorithm performance. The vessel/nonvessel classification results are measured against hand labelled images. A ROC curve is plotted to demonstrate the system performance. The measurements of other tree properties, namely width, length, tortuosity and bifurcation were also tested. The measurements were made on noise free images as well as noisy data.

A validation process is concluded by comparing our proposed algorithm with two popular approaches, i.e. scale-space region growing and threshold probing based on the Matched Filter Response algorithm.

The results show that segmentation of the vascular structure in retina images is possible by the use of multi-resolution Hermite-Gaussian modelling followed by a neighbourhood linking algorithm. Successful segmentation allows a variety of further processing such as;

- Visual highlighting of vessels in the image.
- Accurate characterisation of vessel parameters such as width, length and tortuosity.
- Detection of vessel bifurcation and crossings which can act as intrinsic features for registration purpose.

Further extensions and developments of the proposed algorithm will be discussed in the following chapter together with conclusions of this research.

Chapter 6

Conclusions and Future Work

The work described in this thesis has been concerned with image segmentation within a multi-resolution framework. A new Gaussian-Hermite modelling algorithm is proposed together with an EM type of optimisation scheme and statistical linking algorithm for the modelling and analysis of vascular structure from retinal fundus images. A number of interesting features of the proposed algorithm have been described and shown to be effective and robust on vessel segmentation from noisy data.

- The vessel profile is accurately modelled using a multi-resolution Gaussian-Hermite model followed by an EM type of optimisation scheme.
- Bifurcations and branches are handled by the superposition of Hermite-Gaussian modelling.

- Global topology and complete segmentation of the vascular structure is achieved by using a stochastic linking algorithm.

6.1 Thesis Summary

In Chapter 1, a general introduction of the state and challenges of medical image analysis was first presented. The importance of image segmentation on the success of medical image applications was then addressed which led to the main focus of this dissertation; extraction/segmentation of tree like structures present in medical images such as retinal fundus images.

The objectives of this thesis were to present a general model for images containing tree like structures. A Hermite-Gaussian modelling algorithm is introduced and based on this model, a multi-resolution feature estimation algorithm together with an optimisation scheme and a linking strategy, were developed to provide a complete scheme for the segmentation of the objects. The algorithm is robust to noise and relatively cheap to compute. The stochastic linking strategy proposed, provides a global inference of the tree topology and accommodates the uncertainties of the data.

The main application of the modelling algorithm was tested on retina fundus images, the background to this image modality was discussed together with the needs of automatic detection of vascular structure on clinical di-

agnosis and screening. Towards the end of the chapter, we discussed some distinctive features of vasculature that can be used for image processing techniques to segment the blood vessels. A number of factors that may obstruct vessel segmentation were also listed to set the context for this work.

A review of common segmentation algorithms for branching structures was discussed in Chapter 2. In order to identify common themes in the various approaches, the methods were reviewed in four main classes: *pattern recognition techniques, neural network-based approaches, artificial intelligence-based approaches and morphology based enhancement and detection.* Some of the classes had sub-categories to further distinguish the methods.

In early use of the pattern recognition approach, researchers focussed on vessel segmentation using edge and/or ridge based techniques. Following some kind of gradient or morphological operation, the edges/ridges of the vessels were highlighted and used to detect vessel structure. The drawback of these types of approaches includes, difficulty in handling bifurcations, sensitively to noise and less robustness at training the tree structure without fragmentation. Later on, many researchers proposed various region growing methods to tackle the vessel segmentation problem [36] [15] [38] [39]. In principle, the region growing approach is the process of joining neighbouring pixels into larger regions subject to two major criteria: *similarity* and *spatial proximity.* Based on these two criteria, various algorithms were developed such as single-linkage, centroid-linkage and combined linkage methods. Re-

cently, some researchers have used region growing algorithms on a scale-space representation to obtain the robustness and accuracy gained by a multi-resolution framework [15]. Very encouraging results have been reported that classify vessel and non-vessel pixels, however, the segmentation results depend on the underlying growing algorithm, the choice of seed points, and the thresholding used for limiting the region growing. Match filtering techniques and tracking based techniques are two other commonly used algorithms. In match filtering techniques, regions of interests are highlighted by convolving with multiple matched filters (2D Gaussian) with fixed standard deviations and at different angles. The output is an image with pixel values proportional to the best filter response. Hoover [56] proposed a tracking/probe algorithm based on a matched filter response output and yields a vessel segmentation with good connectivity. The shortcoming of this approach is the amount of distortion inherently incurred at the convolution step, which may lead to substantial classification error and distortion of geometry.

Model based approaches were emphasised since they are directly related to the main focus of this thesis. These approaches have similarities to the human cognitive process that can directly extract the required primitives from the unprocessed raw range images thus avoiding the distortion occurred at a smoothing or convolving stage. Broadly speaking, such methods can be divided into two main classes; deformable models and parametric models. Deformable models use parametric curves that deform under the influence

of both internal and external forces for finding object contours. They can generate smooth curves or surfaces that accurately fit the vessel edges, however, the amount of user interaction and computation required makes them impractical for extracting entire vascular structures. Parametric models impose primitive geometric features that are matched to the data, then employ some kind of estimation-optimisation scheme to obtain the parameters of the data. Algorithms using different parametric models were discussed and compared on modelling vasculature for different image modalities. The algorithm proposed in this thesis uses a Gaussian-Hermite model in a multiresolution framework. The model is able to handle blood vessels with a variety of shapes as well as branching points and bifurcations. It is cheap to compute and robust to noise. In the latter part of the chapter, a brief discussion of different types of approach including, neural network-based, artificial intelligence-based and morphology based enhancement and detection methods, were carried out to address the issues presented in Chapter 1 and to discuss how they have been tackled by various methodologies.

Chapter 3 starts with a discussion of pre-processing steps for the removal of anatomical and pathological features such as the optic disc and exudates from the retinal image. After comparing different approaches, such as the Hough transform, fuzzy C-means clustering and neural networks based on the simplicity and effectiveness of removing such features, we employed a morphological approach which was introduced in [71]. A morphological fil-

tering technique is used to locate the candidate regions of both the optic disc and exudate. The contours of the candidate regions are determined by means of morphological reconstruction. In the latter part of the chapter, the operation of local feature modelling and estimation was detailed along with a discussion of an EM type of optimisation scheme and a model/scale selection algorithm. Firstly, we described a multi-resolution method for estimating orientation, position, width of the vessel segments. Multiple linear features were estimated by using a superposition of Gaussian models. An EM type of iterative optimisation step was then employed to improve initial estimation. Although, the regression leads to a similar set of equations as an EM algorithm, the conceptual basis between our approach and the EM algorithm is rather different. Unlike EM, our regression model implicitly takes into account the spatial information of the data relative to the intensity model, whereas, EM estimates the underlying distribution from which the data are drawn. A Hermite polynomial equation is also used to increase the accuracy of the model to fit a wider range of data profiles.

Chapter 3 was concluded with a description of hierarchical feature analysis which provides a multi-resolution analysis of the data and is computationally more efficient compared with some other techniques such as scale space methods. A bottom up grey-level pyramid is first constructed and feature estimation is carried out at each level without making a decision on whether the measures for local image region are good or not. After constructing the

whole pyramid space, the Akaki Information Criteria is used to choose the optimum model/scale for given regions. The multi-resolution framework allows global information(main vessels) and local information (small vessels) to propagate smoothly across different resolutions.

Chapter 4 detailed the operation of a global inference process for the branching structures. After a brief review of current techniques, two different approaches on branching structure inference and linking were proposed. Based on the parametric representations of local features obtained in Chapter 3, a Region Adjacency Graph was formed by regarding each region as vertices and considering all linking possibilities among neighbouring regions as edges. The basic definitions of graph theory were introduced and followed by a detailed explanation of how we applied a modified Kruskal Maximum Spanning Tree algorithm to the vasculature inference application. The Gaussian-Hermite representation of the image was first converted into a *Spanning Tree* graph structure. The cost of each link between the selected region and its neighbours was recorded. The local conductivities were then identified by finding the highest weighted arcs/edges among the neighbour and to construct a maximum spanning tree (MST). The iterative process ended after all the nodes had been visited. Using the Kruskal type of greedy algorithm, the linking process is reduced to finding the optimum path in a graph representation of the image. The deterministic linking approach is able to successfully track and characterise much of the vessel topology, however,

it is prone to becoming trapped in local maxima and unable to explore less certain, alternative explanations of the data.

The second approach proposed in this chapter is a Markov chain type of stochastic linking strategy. The linking status test is a MAP decision, which incorporates the *prior* knowledge into the posterior distribution. From a stochastic point of view, the Kruskal MST algorithm can be regarded as a simplified MAP estimation with a uniform *prior*, i.e. $P(1) = P(0) = 0.5$. By incorporating a more realistic prior model, the posterior distribution of each mode is calculated according to Bayes rule. A Metropolis-Hasting algorithm is employed which generates a sequence of draws from the *p.d.f.*. The iterative simulation strategy is based on a Markov chain random walk; at each step the Metropolis-Hasting test is used to determine whether to accept or reject the linking between visiting nodes and each of its neighbours.

Effectively, this simulation is a simplified form of Monte Carlo simulation using just one move at each iteration. Based on a good initial estimation of feature parameters provided by multi-resolution Gaussian-Hermite modelling, the simulation rapidly converges to a MAP estimate. As noted in Chapter 4, some other simple moves like alternating the vertices or adding and deleting the branches could be added to make the simulation less dependent on the initial state and better at exploring the state space of solutions.

Chapter 5 provides a quantitative analysis to validate the algorithm per-

formance. A vessel/non-vessel classification was firstly measured with receiver operating characteristic (ROC) curves against the hand-labelled 'gold standard' results. Several important tree geometrical features, including width, length and the tortuosity of the vascular structure, were also measured to further evaluate the algorithm's validity. Vascular intersections and bifurcations are implicitly detected and measured since they are important landmark points for exporting the tree structure, registration and further segmentation processes.

By means of comparison, two other commonly cited algorithms; a scale-space approach [15] and a matched filtering response method [41] were implemented. In the essence of multi-resolution, a scale-space (SS) representation provides coherent information across different resolutions. Based on the SS representation, gradient magnitude and principal curvature were calculated at different scales. Maximum responses were gathered to detect the edges and ridges of the object with various sizes. A region growing technique was then used to classify the region into background and foreground using a thresholding and relaxation technique. In the last part of the chapter, a probing technique based on a Matched filter response (MFR) image was implemented and compared with the Gaussian-Hermite modelling. Experimental results of the different algorithms were listed at the end of the chapter.

6.2 Recommendations for Future Works

Although the results presented here have shown the effectiveness of our approach, it could be further developed in a number of ways:

Extending the algorithm to three dimensions

In principle, the proposed modelling and linking algorithm is dimension independent, however, the larger variety and complexity of 3D data, especially the inter-slice gap between the 3D data, increases the difficulty of the estimation and linking process. Some initial efforts have been made to explore the extendibility of the algorithm to 3D. Using the same algorithm but adding an additional dimension, we executed it on a 3D synthetic tree-structure image, which is shown in figure 6.1. Figure 6.1(b) shows the model reconstruction result at a block size of $16 \times 16 \times 16$.

The results on synthetic images show the potential of the algorithm for working on 3D data. The application to medical imaging would be for blood vessel segmentation in phase contrast angiograms (PCA) or human air-way tree segmentation in 3D CT data [122] [22] [93].

Some preliminary results on two PCA images are shown in figures 6.2 and 6.3. Reconstruction results are overlapped with a line for each estimated feature. Note that colours indicate the orientation of the feature.

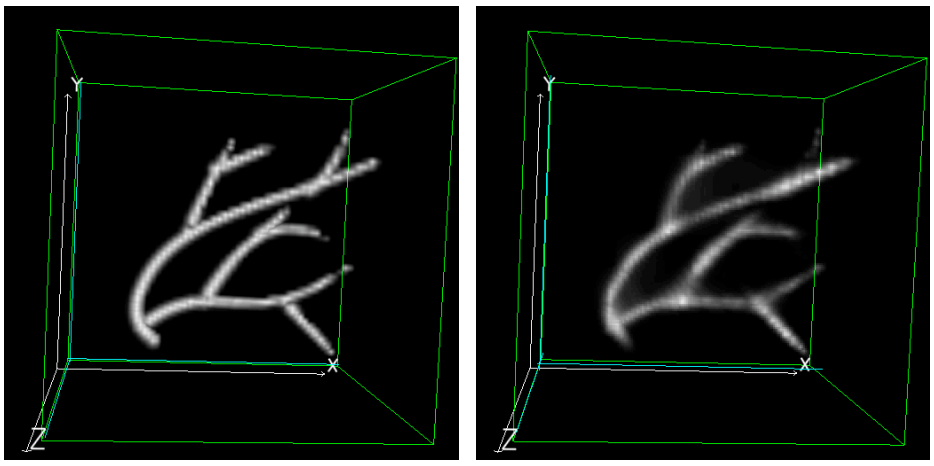

(a) (b)

Figure 6.1: (a) Synthetic 3D tree-Structure date ($64 \times 64 \times 64$) (b) Multiple feature reconstruction with block size $16 \times 16 \times 16$

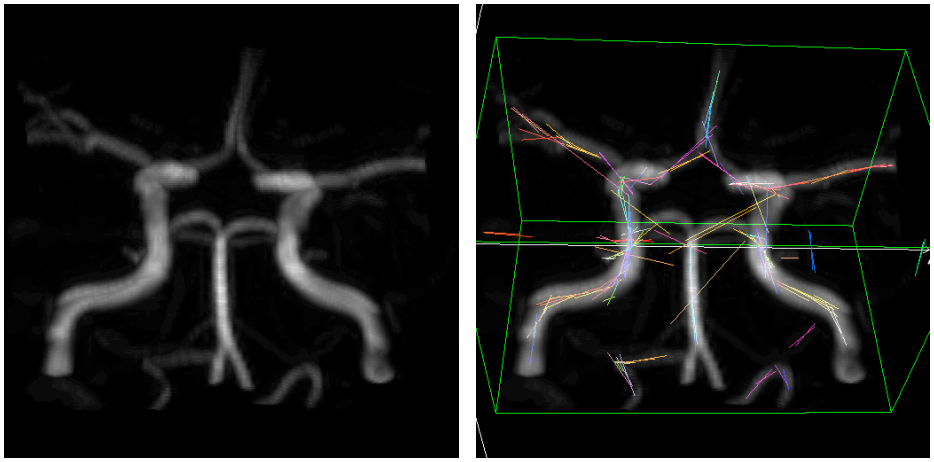

(a) (b)

Figure 6.2: (a) 3D Phase Contrast Angiogram (PCA) (b) Multiple feature reconstruction with block size $16 \times 16 \times 16$. Results are overlapped with lines indicating the accurate estimation of the feature parameters. Different colours represent the estimated orientation of each feature.

Due to time constraints and lack of appropriate 3D data, the scale selection and linking algorithms have not been implemented for 3D images.

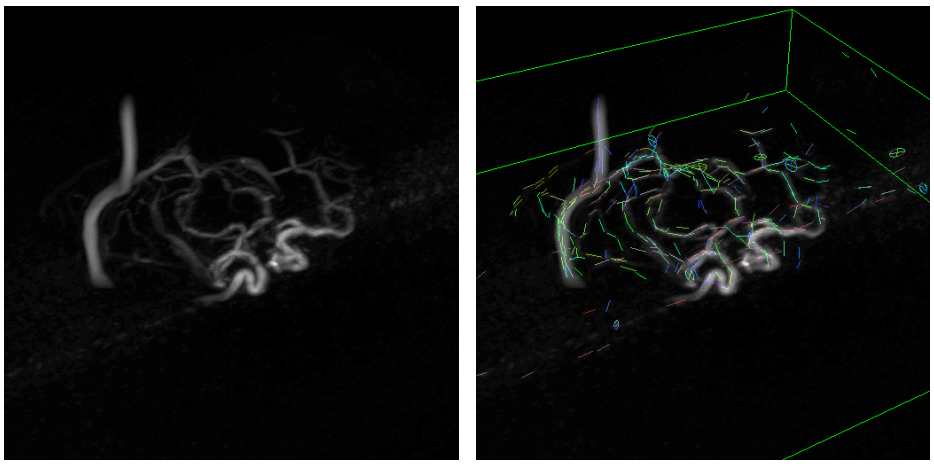

(a) (b)

Figure 6.3: (a) 3D Phase Contrast Angiogram (PCA) (b) Multiple feature reconstruction with block size $16 \times 16 \times 16$. Results are overlapped with lines indicating the accurate estimation of the feature parameters. Different colours represent the estimated orientation of each feature.

Extending the Bayes stochastic linking algorithm to a full MCMC simulation

As mentioned at Chapter 4, the stochastic linking algorithm in a Bayes framework takes into account both the data and some prior parameters on the feature to be extracted. Vascular structures in the image are described in the form of random tree models by their branches (vertices) and connecting vessels (edges). A Metropolis-Hasting test was used in a simplified MCMC algorithm which formed a random process that the configuration space is the space of structure where equilibrium is designed to be the target conditional distribution. At each state, currently there is only one move included, that

is, whether to link the neighbouring feature region or not. By incorporating other moves into the simulation, such as altering the vertex positions or adding/deleting a branch, we could obtain more reliable results that lead to the global optimisation stage and be less dependent on the starting configuration.

6.3 Concluding Remarks

This work has sought to unify a number of different ideas which have been used in branching structure segmentation into a single framework. In summary, the main contributions of this work have been:

- A generalised Gaussian-Hermite modelling and estimation mechanism has been developed that operates within a multi-resolution framework.
- Branching, crossing points, bifurcations of tree like structures can be implicitly modelled.
- A model inference technique using the Akaki Information Criteria (AIC), selected the most appropriate model/scale at a given region in a bottom-up multi-scale representation.
- A deterministic and a stochastic link strategy were proposed to explore the global topology of the vascular structure and therefore obtain a

complete segmentation.

There is clearly much work to be done in the area of branching structure segmentation. Perhaps the most direct extension of this work is using a full MCMC simulation in the Bayesian framework to express properties of vessels through a *prior* which helps the model to cope with ambiguity and noise. The extension of the framework to 3D could open up applications to MRA and CT airway data [22] [123].

Appendix A

Proof of ML Iterative Equations

$$log(Q(\Theta^{(t+1)}, \Theta^{(t)})) = \sum_{\mathbf{x}} \big[-ln\frac{1}{\sqrt{2\pi}} - \frac{1}{2}ln(|\Sigma|) - \frac{1}{2}(\mathbf{x}-\mu)^T\Sigma^{-1}(\mathbf{x}-\mu)\big]W(\mathbf{x}|\Theta^{(t)}) \tag{A.1}$$

Taking the derivative of Equation A.1 with respect to μ and setting it equal to zero, we get:

$$\sum_{\mathbf{x}} \Sigma^{-1}(\mathbf{x}-\mu)W(\mathbf{x}|\Theta^{(t)}) \tag{A.2}$$

with which we can solve for μ,

$$\mu^{(t+1)} = \sum_{\mathbf{x}} W(\mathbf{x}|\Theta^{(t)})\mathbf{x} / \sum_{\mathbf{x}} W(\mathbf{x}|\Theta^{(t)}) \tag{A.3}$$

To derive Σ, we can rewrite Equation A.1 as,

$$\begin{aligned}(-ln\frac{1}{\sqrt{2\pi}} + \frac{1}{2}ln(|\Sigma^{-1}|)) \sum_{\mathbf{x}} W(\mathbf{x}|\Theta^{(t)} - \frac{1}{2}tr(\Sigma^{-1}(\mathbf{x}-\mu)^T(\mathbf{x}-\mu)) \\ = (-ln\frac{1}{\sqrt{2\pi}} + \frac{1}{2}ln(|\Sigma^{-1}|)) \sum_{\mathbf{x}} W(\mathbf{x}|\Theta^{(t)} - \frac{1}{2}tr(\Sigma^{-1}h)\end{aligned} \tag{A.4}$$

where, according to matrix algebra, the trace of a square matrix $tr(\Sigma^{-1}(\mathbf{x}-\mu)^T(\mathbf{x}-\mu)) = \sum_{\mathbf{x}}((\mathbf{x}-\mu)^T\Sigma^{-1}(\mathbf{x}-\mu))$ and $h = (\mathbf{x}-\mu)^T(\mathbf{x}-\mu)$

Taking the derivative with respect to Σ^{-1}, we can derive,

$$\begin{aligned}\frac{1}{2}\sum_{\mathbf{x}} W(\mathbf{x}|\Theta^{(t)})(2\Sigma - diag(\Sigma)) - \frac{1}{2}\sum_{\mathbf{x}} W(\mathbf{x}|\Theta^{(t)})(2h - diag(h)) \\ = \frac{1}{2}\sum_{\mathbf{x}} W(\mathbf{x}|\Theta^{(t)})(2k - diag(k))\end{aligned} \tag{A.5}$$

where $k = \Sigma - h$. By setting equation A.6 to zero, we can easily get,

$$\begin{aligned}&\sum_{\mathbf{x}} W(\mathbf{x}|\Theta^{(t)})(\Sigma - h) = 0 \\ &\Sigma^{(t+1)} = \sum_{\mathbf{x}} W(\mathbf{x}|\Theta^{(t)})(\mathbf{x}-\mu_t)(\mathbf{x}-\mu_t)^T / \sum_{\mathbf{x}} W(\mathbf{x}|\Theta^{(t)}))\end{aligned} \tag{A.6}$$

Appendix B

Proof of Gaussian Product Theorem

If the two arbitrary angular momentum gaussian functions are defined as

$$G_1 = \frac{1}{\sqrt{2\pi|C_1|}} exp[-\frac{1}{2}(\mathbf{x}-\mu_\mathbf{1})^T C_1^{-1}(\mathbf{x}-\mu_\mathbf{1})] \tag{B.1}$$

$$G_2 = \frac{1}{\sqrt{2\pi|C_2|}} exp[-\frac{1}{2}(\mathbf{x}-\mu_\mathbf{2})^T C_2^{-1}(\mathbf{x}-\mu_\mathbf{2})] \tag{B.2}$$

the product of them is derived as

$$\begin{aligned} G_1 \cdot G_2 &= \frac{1}{2\pi\sqrt{|C_1||C_2|}} \\ &exp\{[-\frac{1}{2}[\mathbf{x}^{-T}(C1^{-1} + C_2^{-1})\mathbf{x} - 2\mathbf{x}^T(C1^{-1}\mu_1 + C_2^{-1}\mu_2) + (\mu_1 C_1^{-1}\mu_1 + \mu_2 C_2^{-1}\mu_2)]\} \\ &= \frac{N}{\sqrt{2\pi|C_3|}} exp[-\frac{1}{2}(\mathbf{x} - \mu_3)^T C_3^{-1}(\mathbf{x} - \mu_3)] \\ &= NG_3 \end{aligned} \tag{B.3}$$

where

$$C_3^{-1} = C_1^{-1} + C_2^{-1} \tag{B.4}$$

$$\mu_{\mathbf{3}} = C(C_1^{-1}\mu_1 + C_2^{-1}\mu_2) \tag{B.5}$$

$$N = \frac{\sqrt{|C_3|}}{\sqrt{2\pi|C_1||C_2|}} exp(-\frac{1}{2}\mu_3^T C_3^{-1}\mu_3) \tag{B.6}$$

$$G_3 = \frac{1}{\sqrt{2\pi|C_3|}} exp[-\frac{1}{2}(\mathbf{x} - \mu_{\mathbf{3}})^T C_2^{-1}(\mathbf{x} - \mu_{\mathbf{3}})] \tag{B.7}$$

Integrating the product of the two Gaussian feature models along a line between their mean $\mathbf{y}(t) = \mu_{\mathbf{1}} + (\mu_{\mathbf{2}} - \mu_{\mathbf{1}})t$, can be calculated from equation B.3:

$$\int_{\mu_1}^{\mu_2} G_1 \cdot G_2 = N \int_{\mu_1}^{\mu_2} G_3 \tag{B.8}$$

Appendix C

List of Publications

1. *Robust Modelling of Local Image Structures and its Application to Medical Imagery*, L. Wang, A. Bhalerao and R. Wilson. Proc. Int. Conf. Pattern Recognition, ICPR'04. Cambridge, 2004 [124].

2. *Model Based Segmentation for Retinal Fundus Images*, L. Wang and A. Bhalerao. Proc. of Scandinavian Conference on Image Analysis (SCIA), LNCS, June, 2003. Gotenberg, Sweden [125].

3. *Detecting Branching Structures Using Local Gaussian Models*, L. Wang and A. Bhalerao. in Proc of IEEE International Symposium on Biomedical Imaging (ISBI), July, 2002. Washington, DC [126].

Bibliography

[1] J. S. Duncan and N. Ayache. Medical Image Analysis: Progress over Two Decades and the Challenges Ahead. *IEEE Trans. on Pattern Analysis and Machine Intelligence*, 22(1):85–105, Jan. 2000.

[2] C. C. Reyes-Aldasoro. Classification of Human Knee Data from Magnetic Resonance Images. Technical report, University of Warwick, U.K., 2002.

[3] J. B. Maintz and M. A. Viergever. A Survey of Medical Image Registration. *Med. Image Analysis*, 2(1):1–37, 1998.

[4] D. Aykac, E. A. Hoffman, G. McLennan, and J. M. Reinhardt. Segmentation and Analysis of the Human Airway Tree From Three-Dimensional X-Ray CT Images. *IEEE Trans. on Medical Imaging*, 22(8):940–950, Aug. 2003.

[5] H. P. Hiriyannaiah. X-ray Computed Tomography for Medical Imaging. *IEEE Signal Processing Magazine*, 14:42–59, Mar. 1997.

[6] J. F. Krücker, G. L. LeCarpentier, J. B. fowlkes, and P. L. Carson. Rapid Elastic Image Registration for 3-D Ultrasound. *IEEE Trans on Medical Imaging*, 21(11):1384–1394, Nov. 2002.

[7] J. U. Quistgaard. Signal Acquisition and Processing in Medial Diagnostic Ultrasound. *IEEE Signal Processing Magazine*, 14:67–74, Jan. 1997.

[8] W. S. Hoge, E. L. Miller, H. Lev-Ari, D. H. Brooks, W. C. Karl, and L. P. Panych. An Efficient Region of Interest Acquisition Method for Dynamic Magnetic Resonance Imaging. *IEEE Trans. on Image Processing*, 10(7):1118–1128, July 2001.

[9] G. A. Wright. Magnetic Resonance Imaging. *IEEE Signal Processing Magazine*, 14:56–66, Jan. 1997.

[10] M. E. Martínez-Pérez. *Computer Analysis of the Geometry of the Retinal Vasculature*. PhD thesis, Imperial College of Science, Technology and Medicine, 2000.

[11] R. Wilson. A Multiresolutional Algorithm for Aligning Electrophoresis. Technical report, University of Warwick, U.K., Sep. 1997.

[12] C. C. Reyes-Aldasoro and A. Bhalerao. Volumetric texture description and discriminant feature selection. In *Information Processing in Medical Imaging (IPMI)*, 2003.

[13] M. Cheriet, J. N. Said, and C. Y. Suen. A Recursive Thresholding Technique for Image Segmentation. *IEEE Trans. on Image Processing*, 7(6):918–921, 1998.

[14] W. A. Perkins. Area Segmentation of Images using Edge Points. *IEEE Trans. on Pattern Recognition and Machine Intelligence*, 2(1):8–15, 1980.

[15] M. E. Martinez-Perez, A. D. Hughes, A. V. Stanton, S. A. Thom, A. A. Bharath, and K. H. Parka. Retinal Blood Vessel Segmentation by Means of Scale-Space Analysis and Region Growing. In *Proceedings of the International Conference on Image Processing*, volume 2, pages 173–176, 1999.

[16] M. OḊonnell, J. Gore, and W. Adams. Towards an Automated Algorithm for NMR Imaging: Initial Segmentation Algorithm. *Medical Physics*, 13:293–297, 1986.

[17] M. L. Comer and E. J. Delp. Segmentation of Textured Images using a Multi-resolution Gaussian Autoregressive Model. *IEEE Trans. on Image Processing*, 8(3):408–420, 1999.

[18] N. W. Campbell, B. T. Thomas, and T. Troscianko. Automatic Segmentation and Classification of Outdoor Images Using Neural Networks. *International Journal of Neural Systems*, 8(1):137–144, 1997.

[19] R. Wilson, A. D. Calway, E.R.S. Pearson, and A. Davies. An Introduction to the Multiresolution Fourier Transform and its Applications. Technical Report RR170, University of Warwick, UK, January 1992.

[20] T. Lindeberg. Scale-space theory: A basic tool for analysing structures at different scales. *Journal of Applied Statistics*, 21(2):225–270, 1994.

[21] A. Can, H. Shen, J. N. Turner, J. L. Tanenbaum, and B. Roysam. Rapid Automated Tracing and Feature Extraction from Retinal Fundus Images Using Direct Exploratory Algorithms. *IEEE Transactions on Information Technology in Biomedicine*, 3(2):125–137, June 1999.

[22] J. Tschirren, K. Palagyi, J. M. Reinhardt, E. A. Hoffman, and M. Sonka. Segmentation, Skeletonization, and Branchpoint Matching – A Fully Automated Quantitative Evaluation of Human Intrathoracic Airway Trees. In *Medical Image Computing and Computer-Assisted Intervention (MICCAI)*, 2002.

[23] A. Simo and E. de Ves. Segmentation of Macular Fluorescein Angiographies. A Statistical Approach. *Pattern Recognition*, 34(4):795–809, 2001.

[24] C. Heneghan, J. Flynn, M. O'Keefe, and M. Cahill. Characterization of Changes in Blood Vessel Width and Tortuosity in Retinopathy of Prematurity using Image Analysis. *Medical Image Analysis*, 6:407–429, 2002.

[25] H. Shen, C. V. Stewart, B. Roysam, G. Lin, and H. L. Tanenbaum. Frame-Rate Spatial Referencing Based on Invariant Indexing and Alignment with Application to Online Retinal Image Registration. *IEEE Trans. on PAMI*, 25:379–384, Mar. 2003.

[26] A. Pinz, S. Bernogger, P. Datlinger, and A. Kruger. Mapping the Human Retina. *IEEE Transactions on Medical Imaging*, 17(4):606–619, 1998.

[27] Z. Ben Sbeh, Cohen L. D, G. Mimoun, and G. Coscas. A New approach of geodesic reconstruction for drusen segmentation in eye fundus images. *IEEE Trans. on Medical Imaging*, 20(12):1321–1333, DEC. 1001.

[28] W. E. L. Grimson, G. J. Ettinger, T. Kapur, M. E. Leventon, W. M. Wells, and R. Kikinis. Utilizing Segmented MRI Data in Image-Guided Surgery. *Inter. Journal of Pattern Recognition and Artificial Intelligence*, 11(8):1367–1397, FEB. 1998.

[29] S. C. Orphanoudakis, C. Chronaki, and S. Kostomanolakis. A System for the Indexing, Storage and Retrieval of Medical Images by Content. *Med. Informatics*, 19:109–122, 1994.

[30] C. Kirbas and F. K. H. Quek. A Review of Vessel Extraction Techniques and Algorithms. Technical report, Dept. of Computer Science and Engineering, Wright State University, 2002.

[31] M. A. T. Figueiredo and J. M. N. Leitao. A Non-smoothing Approach to the Estimation of Vessel Contours in Angiograms. *IEEE. Tran. on Medical Imaging*, 14(1):162–172, 1995.

[32] K. Akita and H. Kuga. A computer method of understanding ocular fundus images. *Pattern Recognition*, 15:431–443, 1982.

[33] Y. Kawata, N. Niki, T. Kumazaki, and P. A. Moonier. Characteristics Measurement for Blood Vessels Diseases Detection based on Conebeam CT Images. *IEEE Nuclear Science Symposium and Medical Imaging Conference*, 3:1660–1664, 1995.

[34] D. Guo and P. Richardson. Automatic Vessel Extraction from Angiogram Images. *IEEE Computers in Cardiolog*, 25:441–444, 1998.

[35] I. Liu and Y. Sun. Recursive Tracking of Vascular Networks in Angiograms Based on the Detection-Deletion Scheme. *IEEE Trans. on Medical Imaging*, 12:334–341, 1993.

[36] R. Jain, R. Kasturi, and B. G. Schunck. *Machine Vision*. McGH, 1995.

[37] R. M. Haralick and L. G. Shapiro. *Computer and Robot Vision*. Addison-Wesley, 1992.

[38] J. F. Mangin, V. Frouin, I. Bloch, I. Bloch, J. Regis, and J. Lopez-Krahe. From 3D Magnetic Resonance Images to Structual Representations of the Cortex Topography using Topology Preserving Deformations. *Jounal of Math. Imag. Vis.*, 5:297–318, 1995.

[39] J. K. Udupa, L. Wei, S. Samarasekera, Y. Miki, and M. A. van Buchem adn R. I. Grossman. Multiple Sclerosis Lesion Quantification Using Fuzzy-connectedness Principles. *IEEE Trans. Medical Imaging*, 16:598–609, 1997.

[40] B. Kochner, D. Schuhmann, M. Michaelis, G. Mann, and K. H. Englmeier. Course Tracking and Contour Extraction of Retinal Vessels from Color Fundus Photographs: Most Efficient Use of Steerable Filters for Model Based Image Analysis. In *Proc. SPIE Medical Imaging*, pages 22–28, 1998.

[41] A. Hoover, V. Kouznetsova, and M. Goldbaum. Locating Blood Vessels in Retinal Images by Piecewise Threshold Probing of a Matched Filter Response. *IEEE Transactions on Medical Imaging*, 19(3):203–210, 2000.

[42] S. Chardhuri, S. Chatterjee, N. katz, M. Nelson, and M. Goldbaum. Detection of Blood Vessels in Retinal Images Using Two-Dimensional Matched Filters. *IEEE Transcations on Medical Imaging*, 8(3):263–269, 1989.

[43] L. Zhou, M. S. Rzeszotarski, L. J. Singerman, and J. M. Chokreff. The Detection and Quantification of Retinaopathy using Digital Angiograms. *IEEE Trans. on Medical Imaging*, 13:619–626, 1994.

[44] W. E. Hart, M. Goldbaum, B. Cote, P. Kube, and M. R. Nelson. Automated Measurement of Retinal Vascular Tortuosity. In *Proc. AMIA Fall Conference*, 1997.

[45] J. Chen, Y. Sato, and S. Tamura. Orientation Space Filtering for Multiple Orientation Line Segmentation. In *Proc. of IEEE Conf. on CVPR*, pages 311–317, 1998.

[46] B. D. Thackray and A. C. Nelson. Semi-Automatic Segmentation of Vascular Network Images Using a Rotating Structuring Elements (ROSE) with Mathematical Morphology and Dual Feature Thresholding. *IEEE Transactions on Medical Imaging*, 12(3):385–392, Sep. 1993.

[47] A. K. Klein, F. Lee, and A. A. Amini. Quantitative Coronary Angiography with Deformable Spline Models. *IEEE Transactions on Medical Imaging*, 16(5):468–482, Oct. 1997.

[48] R. R. Petrocelli, J. Elion, and K. M. Manbeck. A New Method for Structure Recognition in Unsubtracted Digital Angiograms. In *IEEE Computers in Cardiology*, pages 207–210, 1992.

[49] X. H. Gao, A. Bharath, and A. Stanton adn A. Hughes. Measurement of Vessel Diameters on Retinal Images for Cardiovascular Studies. In *Medical Image Understanding and Analysis*, 2001.

[50] A. Bhalerao and R. Wilson. Estimating Local and Global Image Structure using a Gaussian Intensity Model. *Medical Image Understanding and Analysis*, 2001.

[51] P. E. Summers and A. Bhalerao. Derivation of Pressure Gradients form Magnetic Resonance Angiography using Multi-resolution Segmentation. In *Proceedings of International Conference on Image Processing and its Application*, 1995.

[52] T. Lindeberg. Junction Detection with Automatic Selection of Detection Scales and Localization scales. In *Proc. 1st International Conference on Image Processing*, volume 1, pages 924–928, Nov. 1994.

[53] A. R. Davies and R. Wilson. Curve and Corner Extraction using the Multiresolution Fourier Transform. In *Image Processing and its Applications*. 4h IEE Conf., 1992.

[54] Y. Sun. Automated Identification of Vessel Contours in Coronary Arteriograms by an Adaptive Tracking Algorithm. *IEEE Trans on Medical Imaging*, 8(1):78–88, 1989.

[55] S. Tamura, Y. Okamoto, and K. Yanashima. Zero-Crossing Interval Correction in Tracking Eye-Fundus Blood Vessels. *Pattern Recog.*, 21(3):227–233, 1988.

[56] A. Hoover and M. Goldbaum. Locating the Optic Nerve in a Retinal Image Using the Fuzzy Convergence of the Blood Vessels. *IEEE Trans. on Medical Imaging*, 19(3):203–210, 2003.

[57] O. Chutatape, L. Zheng, and S. M. Krishnan. Retinal Blood Vessel Detection and Tracking Matched Gaussian and Kalman Filters. In

IEEE Anuual International Conference of Engineering in Medicine and Biology Society., volume 20, pages 3144–3149, 1998.

[58] M. A. T. Figueiredo and J. M. N. Leitao. Nonsmoothing Approach to the Estimation of Vessel Contours in Angiograms. *IEEE Transactions on Medical Imaging*, 14(1):162–172, 1995.

[59] R. Nekovei and Y. Sun. Back-propagation Network and its Configuration for Blood Bessel Detection in Angiograms. *IEEE Transactions on Neural Networks*, 6:64–72, Jan. 1995.

[60] J. C. Bezdek, L. O. Hall, and L. P. Clarke. Review of MR Image Segmentation Techniques using Pattern Recognition. *Medical Phys.*, 20:1033–1048, 1993.

[61] D. L. Vilarino, M. Brea V, D. Cabello, and J. M. Pardo. Discrete-time CNN for Image Segmentation by Active Contours. *Pattern Recognition Letter*, 19:721–734, 1998.

[62] G. G Gardner, D. Keating, T. H. Williamson, and A. T. Elliot. Automatic Detection of Diabetic Retinopathy using an Aritficial Neural Network. *British Journal of Ophthomology*, pages 940–944, 1996.

[63] P. M. Meaney, K. D. Paulsen, and J. T. Chang. Near-field Microwave Imaging of Biologically-based Materials Using a Monopole Transceiver System. *IEEE Trans. Microwave Theory Tech.*, 46:31–45, 1998.

[64] V. Bombardier, M. C. Jaluent, A. Bubel, and J. Bremount. Cooperation of Two Fuzzy Segmentation Operators for Digital Subtracted Angiograms Analysis. In *IEEE Conf. on Fuzzy Sustem*, volume 2, pages 1057–1062, 1997.

[65] F. Zana and Klein J, C. Robust Segmentation of Vessel from Retinal Angiography. In *Int. Conf. Digital Signal Processing*, pages 1087–1091, 1997.

[66] M. Lalonde, . Gagnon, and M. Boucher. Non-recursive Paired Tracking for Vewwsel Extraction from Retinal Images. In *Conference Vision Interface*, Montreal, May 2000.

[67] L. Lecornu, J. J. Jacq, and C. Roux. Simultaneous Tracking of the Two Edges of Linear Structures. In *Proc. Int. Conf. on Image Processing*, pages 188–192, 1994.

[68] A. Davies. *Image Feature Analysis using the Multiresolution Fourier Transform*. PhD thesis, University of Warwick, UK, August 1993.

[69] D. Boukerroui, A. Baskurt, J. A. Noble, and O. Basset. Segmentation of Ultrasound Images-Multiresolution 2D and 3D Algorithm Based on Global and Local Statistics. *Pattern Recognition Letters*, 24:779–790, 2003.

[70] P. Meulemans. *Hierarchical Image Sequence Analysis and Segmentation*. PhD thesis, Department of Computer Science, University of Warwick, 2001.

[71] T. Walter, J. Klein, P. Massian, and A. Erginay. A Contribution of Image Processing to the Diagnosis of Diabetic Retinaopathy - Detection of Exudates in Color Fundus Images of the Human Retina. *IEEE Trans. on Medical Imaging*, 12(10):1236–1243, Oct. 2002.

[72] L. Gang, O. Chutatape, and S. M. Krishnan. Detection and Measurement of Retinal Vessels in Fundus Images Using Amplitude Modified Second-Order Gaussian Filter. *IEEE Tran. on Biomedical Engineering*, 49(2):168–172, Feb. 2002.

[73] A. Osareh, M. Mirmehdi, B. Thomas, and R. Markham. Automatic Recognition of Exudative Maculopathy using Fuzzy C-Means Clustering and Neural Networks. In *Medical Image Understanding and Analysis*, 2001.

[74] A. Pinz, S. Bernögger, P. Datlinger, and A. Kruger. Mapping the Human Retina. *IEEE Trans on Medical Imaging*, 17(4):606–620, Aug. 1998.

[75] A. Calway. *The Multiresolution Fourier Transform: A general Purpose Tool for Image Analysis.* PhD thesis, University of Warwick, U.K., 1989.

[76] A. Papoulis. *Signal Analysis.* McGraw-Hill, New York, 1977.

[77] A. I. Borisenko and I. E. Tarapov. *Vector and Tensor Analysis with Applications.* Dover Publications, New York, 1979.

[78] J. B. Antoine Maintz and Viergever M. A. A Survey of Medical Image Registration. *Medical Image Analysis*, 2(1), 1998.

[79] A. Davies and R. Wilson. Curve and Corner Extraction using the Multiresolution Fourier Transform. Technical Report RR 202, University of Warwick, UK, November 1991.

[80] B. Kovesi, J. M. Boucher, and S. Saoudi. Stochastic K-means algorithm for vector quantization. *Pattern Recognition Letters*, 22:603–610, 2001.

[81] C. Bishop. *Neural Networks for Pattern Recognition.* Clarendon Press, Oxford, 1995.

[82] R. Wilson. Modelling of 2D gel Electrophoresis Images for Proteomics Databases. In *ICPR*, Quebec City, 2002.

[83] R. Wilson, I. Levy, and P. Meulemans. Image Sequence Analysis and Segmentation using G-Blobs. In *Intr. Conference on Image Processing (ICIP).* IEEE, 1996.

[84] G. E. P. Box and G. M. Jenkins. *Time Series Analysis: Forecasting and Control.* Holden-Day, London, 1970.

[85] K. P. Burnham and D. R. Anderson. *Model Selection and Inference*. Springer-Verlag, 1998.

[86] A. H. Bhalerao. *Multiresolution Image Segmentation*. PhD thesis, University of Warwick, U.K., 1991.

[87] A. Klinger. *Pattern and Search Statistics in Optimising Methods in Sattistics*. Academic Press, New York, 1971.

[88] H. Akaike. Infomatin Theory as an Extension of the Maximum-likelihood Principle. *Second International Symposium on Information Theory*, pages 267–281, 1973.

[89] C. M. Hurvich and C-L. Tsai. Regression and Time Series Model Selection in Small Samples. *Biometrika*, pages 297–307, 1989.

[90] M. Spann and R. Wilson. A Quad-Tree Approach to Image Segmentation Which Combines Statistical and Spatial Information. *Pattern Recognition*, pages 257–269, 1985.

[91] D. Rueckert, P. Burger, S. M. Forbat, R. D. Mohiaddin, and G. Z. Yang. Automatic Traking of the Aorta in Cardiocascular MR Images Using Deformable Models. *IEEE Trans. on Medical Imaging*, 16:581–590, 1997.

[92] K. Haris, S. Efstratiadis, N. Maglaveras, C. Pappas, J. Gourassas, and G. Louridas. Model-based Morphological Segmentation and Labeling of Coronary Angiograms. *IEEE Trans. on Medical Imaging*, 18:1003–1015, 1999.

[93] V. Sauret, K. A. Goatman, J. S. Fleming, and A. G. Bailey. Semi-Automated Tabulation if the 3D Topology and Morphology of Branching Networks Using CT: Application to the Airway Tree. In *Phys. Med. Biol*, page 44, 1999.

[94] P. H. Eichel, E. J. Delp, K. Koral, and A. J. Buda. A Method for a Fully Automatic Definition of Coronary Arterial Edges From Cineangiograms. *IEEE Trans. on Medical Imaging*, 7:313–319, 1988.

[95] Y. A. Tolias and S. M. Panas. A Fuzzy Vessel Tracking Algorithm for Retinal Images Based on Fuzzy Clustering. *IEEE Trans. on Medical Imaging*, 17(2):263–273, 1998.

[96] P. E. Hart, N. J. Nilson, and B. Raphael. A Formal Basis for the Heuristic Determination of Minimum-Cost Paths. *IEEE Trans. Syst. Man. Cyb*, SMC-4:100–107, 1968.

[97] R. Skvarcius and W. B. Robinson. *Discrete Mathematics with Computer Science Applications*. Benjamin and Cummings, 1986.

[98] W. M. Wells, R. Kikinis, W. E. L. Grimson, and R. Jolesz. Adaptive Segmentation of MRI Data. *IEEE. Trans. Medical Imaging*, 15:429–442, 1996.

[99] D. L. Wilson and J. A. Noble. An Adaptive Segmentation Algorithm for Extracting Arteries and Aneurysms from Time-of-flight MRA Data. *IEEE Trans. on Medical Imaging*, 18:938–945, 1999.

[100] A. Bhalerao, E. Thönnes, W. Kendall, and R. Wilson. Inferring Vascular Structure from 2D and 3D Imagery. In *Medical Image Computing and Computer-Assisted Intervention (MICCAI)*, 2001.

[101] A. C. S. Chung, J. A. Noble, and P. Summers. Fusing Speed and Phase Information for Vascular Segmentation of Phase Contrast MR Angiograms. *Medical Image Anaysis*, 6:109–128, 2002.

[102] T. Jaakkola and M. Jordan. Varational Probabiistic Inference and the QMR-DT Database. *Journal of Artificial Intelligence Research*, 10:291–322, 1999.

[103] W. R. Gilks, S. Richardson, and D. J. Spiegelhalter. *Markov Chain Monte Carlo in Pratice.* Chapman and Hall, 1996.

[104] D. Gamerman. *Marko Chain Monte Carlo. Stochastic simulation for Bayesian inference.* Chapman and Hall, 1997.

[105] E. Thönnes, A. Bhalerao, W. Kendall, and R. Wilson. Bayesian Approaches to Medical Image Analysis: Inferring Vascular Tree Structure from 2D Imagery. Technical report, University of Warwick, 2003.

[106] E. Thönnes, A. Bhalerao, W. Kendall, and R. Wilson. A Bayesian Approach To Inferring Vascular Tree Structure From 2D Imagery. In *Intr. Conference on Image Processing (ICIP).* IEEE, 2002.

[107] A. Gelman, J. B. Carlin, H. S. Stern, and D. B. Rubin. *Bayesian Data Analysis.* Chapman and Hall, 1995.

[108] C. E. Metz. Basic Principles of ROC Analysis. *Seminars Nucl. Med.*, 8(4):283–298, 1978.

[109] A. Houben, M. Canoy, H. Paling, P. Derhaag, and P. De Leeuw. Quantitative Analysis of Retinal Vascular Changes in Essential and Renovascular Hypertension. *Journal of Hypertension*, 13:1729–1733, 1995.

[110] A. Stanton, B. Wasan, A. Cerutti, S. Ford, R. marsh, P. Sever, S. Thom, and A. Hughes. Vascular Network Changes in the Retina with Age and Hypertension. *Journal of Hypertension*, 13:1724–1728, 1995.

[111] T. Y. Wong, A. R. Sharrett, M. I. Schmidt, J. S. Pankow, D. J. Couper, B. E. K. Klein, L. D. Hubbard, and B. B. Duncan. Retinal Arteriolar Narrowing and Risk of Diabetes Mellitus in Middle-aged Person. *Journal of American Medical Association*, 287:2528–2533, 2002.

[112] J. Canny. A Computational Approach to Edge Detection. *IEEE Trans. Pattern Analysis and Machine Intel.*, 8(6):679–698, 1986.

[113] P. O. Kazanchyan, V. A. Popov, Y. N. Gaponova, and T. V. Rudakova. The Diagnosis and Treatment of Pathological Deformations of the Carotid Arteries. *J. Ang. Vasc. Surg.*, 7:93–103, 2001.

[114] Ö. Smedby, N. Högman, S. Nilsson, U. Erikson, A. G. Olsson, and G. Walldius. Two-dimensional Tortuosity of the Superficial Femoral Artery in Early Atherosclerosis. *Journal of Vascular Research*, 30:181–191, 1993.

[115] R. Mehrotr, S. Nichani, and N. Ranganathan. Corner Detection. *Pattern Recognition*, 23(11):1223–1233, 1990.

[116] J. Koenderink. The Structure of Images. *Biol. Cybern.*, 50:363–370, 1984.

[117] A. F. Korn. Toward a Symbolic Representation of Intensity Changes in Images. *IEEE Trans. Pattern Analysis and Machine Intel.*, 10(5):610–625, 1988.

[118] D. Eberly. Ridges in image and data analysis. *Computational Imaging and Vision*, 1996.

[119] T. Lindeberg. Feature Detection with Automatic Scale Selection. *Int.J. of Computer Vision*, 30(2), 1998.

[120] N. Otsu. A threshold selection method from gray-level histograms. *IEEE. Trans. on SMC*, 9:62–66, 1979.

[121] N. P. Katz. S. Chaudhuri M. H. Goldbaum and M. Nelson. Image Understanding for Automated Retinal Diagnosis. *Proc. Symposium for Computer Applications in Clin. Med. IEEE*, pages 756–760, 1989.

[122] A. Chung, J. A. Noble and P. Summers. Vascular Segmentation of Phase Contrast Magnetic Resonance Angiograms Based on Statistical Mixture Modeling and Local Phase Coherence. *IEEE Transactions on Medical Imaging*, 23(12):1490–1507, 2004.

[123] A. C. S. Chung, J. A. Noble, P. Summers, and M. Brady. 3D Vascular Segmentation using MRA Statistics and Velocity Field Information in PC-MRA. *Information Processing in Meedical Imaging*, pages 453–360, 2001.

[124] L. Wang, A. Bhalerao, and R. Wilson. Robust Modelling of Local Image Structures and its Application to Medical Imagery. In *International Conference on Pattern Recognition (ICPR)*, August 2004.

[125] L. Wang and A. Bhalerao. Model Based Segmentation for Retinal Fundus Images. In *13th Scandinavian Conference on Image Analysis (SCIA)*. Springer, June 2003.

[126] L. Wang and A. Bhalerao. Detecting Branching Structures Using Local Gaussian Models. In *International Symposium on Biomedical Imaging (ISBI)*. IEEE, July 2002.